ALL-ORGANIC INFRARED-TO-VISIBLE UP-CONVERSION OLEDS FOR LOW-COST SWIR IMAGING

By

GIJUN SEO

Bachelor of Science in Information Display
KyungHee University
Seoul, Republic of Korea
2012

Master of Engineering in Information Display
KyungHee University
Seoul, Republic of Korea
Master of Engineering in Innovation Technology
École Polytechnique
Palaiseau, France
2015

Submitted to the Faculty of the
Graduate College of the
Oklahoma State University
in partial fulfillment of
the requirements for
the Degree of
DOCTOR OF PHILOSOPHY
July 2020

ALL-ORGANIC INFRARED-TO-VISIBLE

UP-CONVERSION OLEDS

FOR LOW-COST SWIR IMAGING

Dissertation Approved:

Dr. Do Young Kim

Dissertation Adviser

Dr. Raman P. Singh

Dr. Raj N. Singh

Dr. Shuodao Wang

ACKNOWLEDGEMENTS

I would first like to thank my advisor Dr. Do Young Kim. He was always helpful whenever I ran into a trouble spot or had a question about my research. He consistently allowed me to be motivated and encouraged to my work and steered me in the right the direction whenever he thought I needed it.

I would also like to thank my dissertation committee members: Dr. Raman P. Singh, Dr. Raj N. Singh, and Dr. Shuodao Wang. The guidance and advices throughout of my PhD program were enormously helpful.

I would also like to appreciate the faculty and the staff members in the Department of MSE at Oklahoma State University. I am gratefully indebted to them for their unbelievably valuable supports.

Finally, I must express my very profound gratitude to my family for providing me with unfailing support and continuous encouragement throughout my years of study and through the process of researching and writing this thesis. This accomplishment would not have been possible without them. Thank you.

Name: GIJUN SEO

Date of Degree: JULY 2020

Title of Study: ALL-ORGANIC INFRARED-TO-VISIBLE UP-CONVERSION OLEDS FOR LOW-COST SWIR IMAGING

Major Field: MATERIALS SCIENCE AND ENGINEERING

Abstract: As a low-cost alternative technology to conventional expensive short-wavelength infrared (SWIR) imaging technology based on InGaAs semiconductors, an infrared (IR)-to-visible up-conversion organic light-emitting diode (OLED) has recently been developed with the potential to convert an IR image to a visible image without pixilation in the device, thus enabling a high-quality image at a significantly low-cost. Recent IR-to-visible up-conversion OLEDs clearly demonstrated the pixel-less SWIR imaging capability directly up-converting SWIR images to visible images by using epitaxial-free solution-based PbS/PbSe colloidal quantum dots (CQDs) as the SWIR sensitizer. However, the large volume synthesis of PbS/PbSe CQDs and the solution-processed device fabrication using PbS/PbSe CQDs are still under development and not ready for manufacturing yet.

In this study, fabrication of all-organic IR-to-visible up-conversion OLEDs is demonstrated by replacing colloidal quantum dot SWIR sensitizers to organic SWIR sensitizer. In order to achieve the aim, following researches were conducted: (1) discover low bandgap small molecules and polymers with strong IR sensitivity in SWIR wavelength, (2) investigate electron acceptors with an appropriate energy alignment to SWIR sensitive low-bandgap organic electron donors, and (3) study the effect of hole blockers in IR-to-visible up-conversion OLEDs. First, low-bandgap organic materials with SWIR sensitivity up to 1200 nm are demonstrated using a low-bandgap polymer, poly 4-(4,8-bis(5-(2-butyloctyl) thiophen-2-yl) benzo[1,2-b:4,5-b′] dithiophen-2-yl)-6,7-diethyl-[1,2,5]thiadiazolo[3,4-g]quinoxaline (PBDTT-BTQ), newly synthesized by alternating strong electron-withdrawing/donating building blocks, and a low-bandgap small molecule, $SnNcCl_2$, selected by adding additional conjugated aromatic rings on the phthalocyanine framework. Next, photodetectors using the SWIR sensitizing materials are fabricated for demonstrating the photoelectric performance of the SWIR sensitizers in actual devices. The photodetector using PBDTT-BTQ shows the maximum detectivity of 3×10^{11} Jones at the wavelength of 1000 nm, while the $SnNcCl_2$ photodetectors showing the maximum detectivity of 2×10^{11} Jones at the wavelength of 1000 nm. Finally, SWIR-to-visible up-conversion OLEDs using PBDTT-BTQ and $SnNcCl_2$ are demonstrated successfully, with sensitivity up to 1200nm. The operation voltage windows are 7 V for the PBDTT-BTQ up-conversion OLED, and 5 V for the $SnNcCl_2$ up-conversion OLED. The importance of the energy band alignment in the sensitizing layer and the hole blocking layer effect are also studied.

TABLE OF CONTENTS

Chapter Page

Chapter Page

VII. SWIR-TO-VISIBLE UP-CONVERSION OLEDs (cont'd)

LIST OF TABLES

Table Page

LIST OF FIGURES

Figure Page

Figure Page

Figure Page

CHAPTER I

INTRODUCTION

1. Current Extremely Expensive Epitaxial-Grown InGaAs-based SWIR Imaging Technology

Infrared (IR) imaging devices have attracted a great deal of research interest because of their potential applications in range finding, security, semiconductor wafer inspections, night vision as

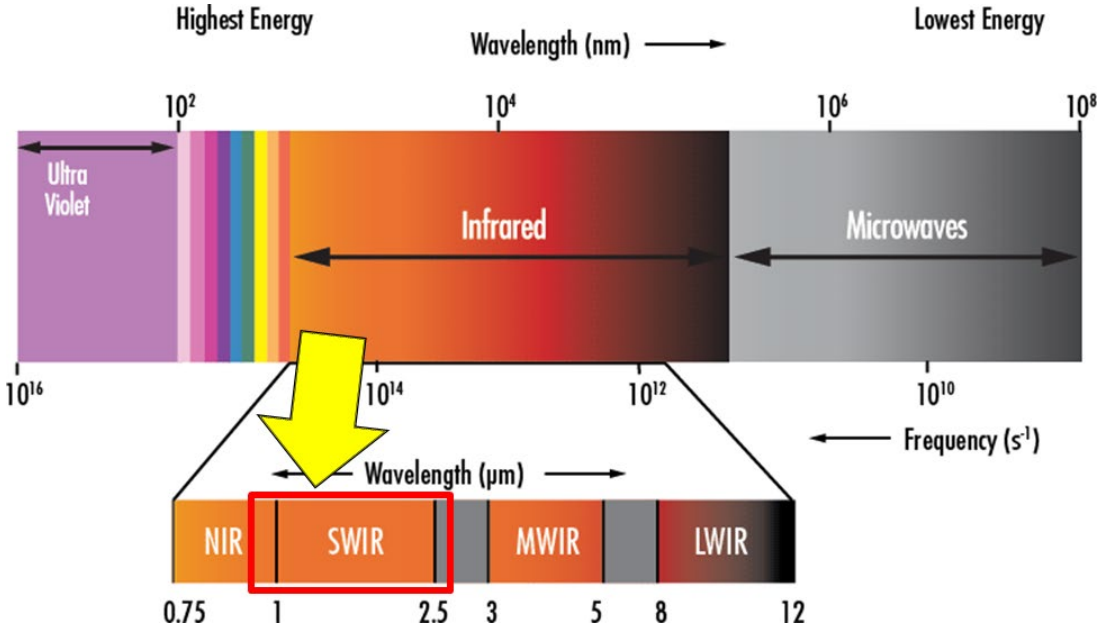

Figure 1 Divisions of electromagnetic waves and sub-divisions of infrared region.

well as medical imaging.[1-10] The short wavelength infrared (SWIR) spectral region between 0.7 and 2.5 μm is of particular commercial interest due to the low water absorption in this range as shown in Figure 1[11]. Because of the low water absorption in the SWIR range, therefore, SWIR imaging technology can enable us to see through with highly accurate images even in severe situations such as heavy rain, thick foggy, and heavy smoky fire that cannot see through by human eyes and visible cameras.

Current SWIR image sensor technologies as shown in Figure 2 are extremely expensive technology because (1) SWIR-sensitive III-V compound semiconductors ALWAYS require an expensive epitaxial growth process only suitable for small area applications [12] and (2) the epitaxial-grown InGaAs-based SWIR photodetector pixel arrays MUST be connected to Si-based readout integrated circuits (ROIC) by problematic chip bonding processes for making IR imaging, thus resulting in the tremendous price of more than $20,000. Due to this traditional ROIC integration method which is very challenging to make a fine pixel size, furthermore, the

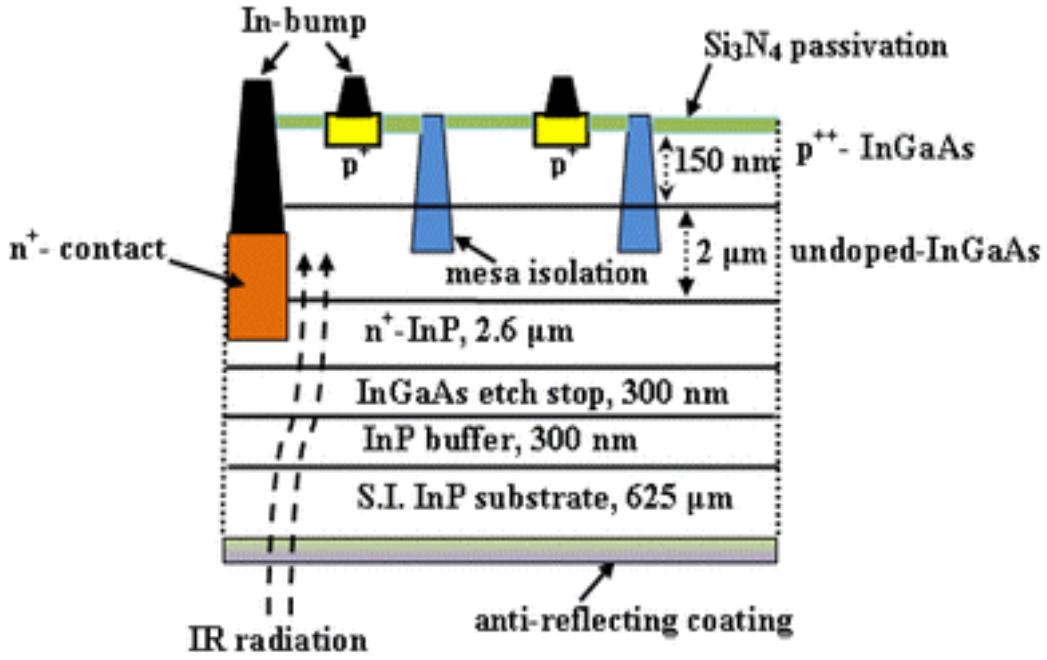

Figure 2 InGaAs SWIR sensor device structure.

final SWIR image sensors have a limited pixel resolution of below 1M pixels. Therefore, the applications of the traditional SWIR image sensors have been severely limited.

2. Alternative Approach for Low-cost SWIR Imaging: IR-to-Visible Up-conversion devices

Optical up-conversion devices are optoelectronic devices that convert low energy photons to high energy photons.[1, 10, 13-19] Generally, these devices consist of a sensitizing part for absorbing low energy light and a light-emitting part for emitting high energy light. Therefore, optical up-conversion devices would be a low-cost alternative IR imaging technology because they offer the potential to convert an IR image to a visible image without pixel array in the device.

2.1. Early Up-conversion Device Based on Epitaxial-grown Inorganic Semiconductors

Up-conversion devices based on inorganic compound semiconductors have been fabricated by integrating an IR photodetector with a light-emitting diode (LED) as shown in Figure 3 (a).[14, 15, 18, 19] However, growing an inorganic LED on top of a photodetector requires lattice matching of two material systems; as a result, only a limited choice of materials is available.[16, 20, 21] III-V semiconductor-based up-conversion devices can only up-convert light of wavelength 1.5 μm to 1 μm and thus are not possible to up-convert IR to visible lights.[19] Ban et. al. combined an organic light-emitting diode (OLED) with an InGaAs/InP photodetector to make an IR-to-Visible up-conversion device as shown in Figure 3 (b),[22] and it converts infrared to visible successfully. But it has still a limitation that can detect the IR but not get the IR image due to incapable of pixelization, because the whole device emits visible lights due to the nature of the InGaAs semiconductor. In addition, these inorganic up-conversion devices still require epitaxially growth of inorganic semiconductor, which is only suitable for small wafer substrates, and thus are still

expensive to fabricate for large-area applications.

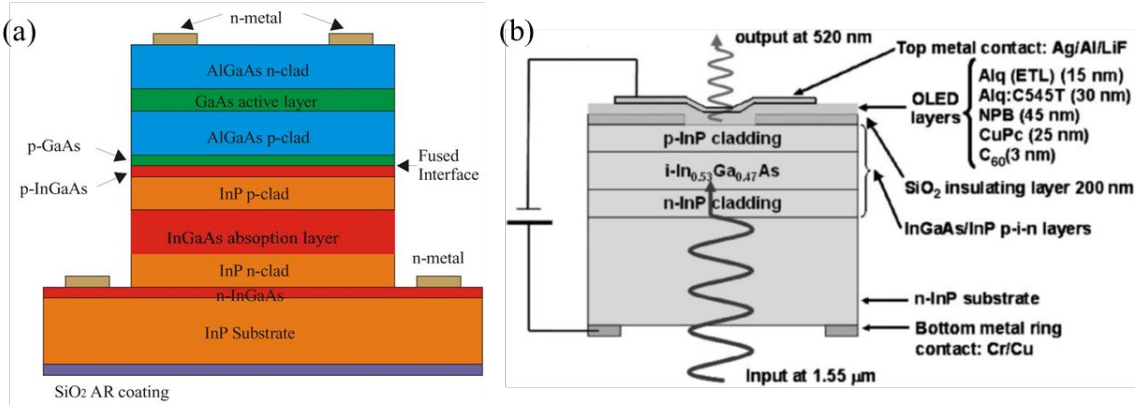

Figure 3 Schematic structure diagram of up-conversion devices based on inorganic InGaAs semiconductor. (a) InGaAs-GaAs up-conversion device, and (b) InGaAs-OLED up-conversion device.

2.2. Low-cost Up-conversion OLED with Epitaxial-free Inorganic CQD SWIR Sensitizers

Unlike epitaxial-grown InGaAs-baesed SWIR sensitive semiconductors, solution-processed epitaxial-free colloidal quantum dot (CQD) inorganic semiconductors with SWIR photosensitivity has great potential for extremely low-cost SWIR imaging because of its inherent compatibility with low-cost, low-temperature, and large area processing methods. CQD inorganic semiconductors are widely used in optoelectronic applications, where their size-tunable optoelectronic properties and their suitability for printing or solution-based processing are distinctive features and major assets.[23] PbS CQDs with excellent photosensitivity, bandgap tunability, and solution processability provide an attractive platform for low-cost multi-spectral photodetectors with light sensitivity from the UV/Visible to SWIR (350-2000 nm) spectral regions.[19] There are numerous reports of devices using PbS CQDs as the infrared sensitizer.[19] Kim *et. al.* recently reported a solution-processed inorganic PbS CQD photodetector with outstanding air-stability and a detectivity of more than 10^{12} Jones, comparable to epitaxial grown InGaAs photodetectors in terms of noise and detectivity.

Recently, OLED-based infrared-to-visible up-conversion devices, called to the IR-to-visible up-conversion OLEDs, have attracted a great deal of research interest as an alternative infrared imaging technology because they also offer the potential to convert an infrared image to a visible image without pixilation in the device, thus enabling a high-quality image at a significantly low cost. [13, 17, 24] The IR-to-visible up-conversion OLEDs have a similar structure compared with conventional OLEDs as shown in Figure 4.[17] This device is basically an OLED with an epitaxial-free solution-processed PbS or PbSe CQD as the SWIR sensitizing layer and only emits visible light under infrared illumination. [13, 17] The light emission modulation by IR light is clearly demonstrated.

The pixel-less IR imaging capability of the IR-to-visible up-conversion OLEDs are already clearly demonstrated by incorporating the IR-to-visible up-conversion OLED into a commercially available DSLR camera as shown in Figure 5 (a).[24] The active device area of the IR sensitive OLED is 1 cm^2 and this device has an extremely simple structure with only one anode pad and

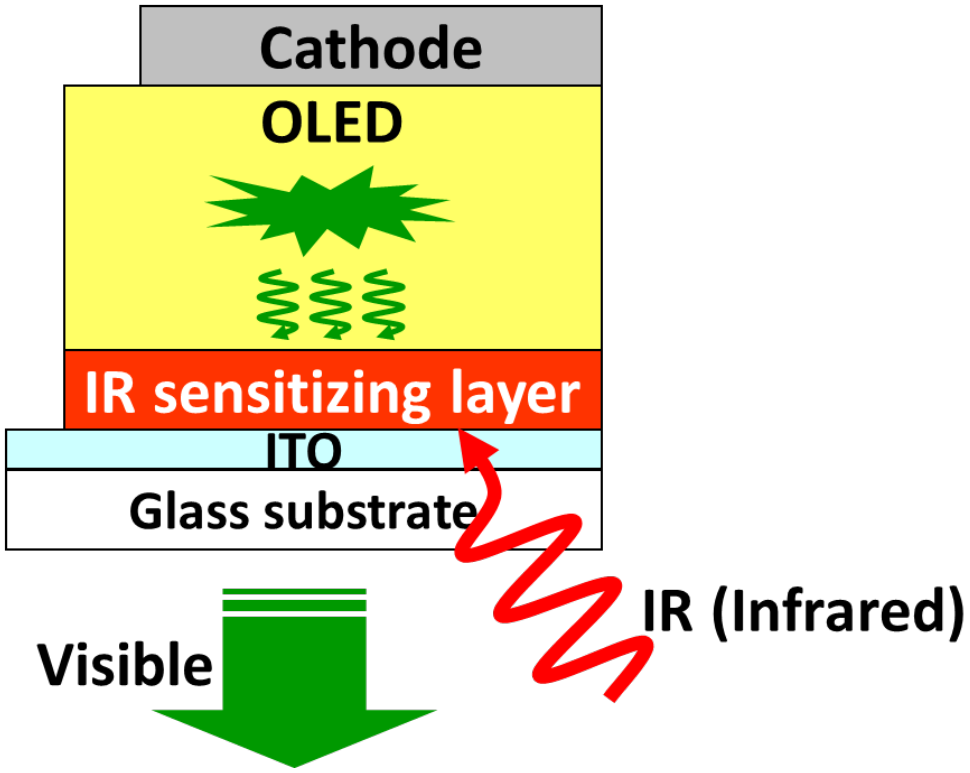

Figure 4 Schematic diagram of the IR-to-visible up-conversion OLEDs.

one cathode pad for supplying the electrical power. The photo images of "UF" were taken in the dark illuminated with the IR light as shown in Figure 5 (b). The up-converted visible images were clear, indicating the high-quality pixel-less imaging capability of IR-to-visible up-conversion OLEDs. The upper limit of the image resolution in the IR sensitive OLED will be total film thicknesses of about 0.2 μm and thus high-resolution up-converted images can be realized in the IR-to-visible up-conversion OLED. [17]

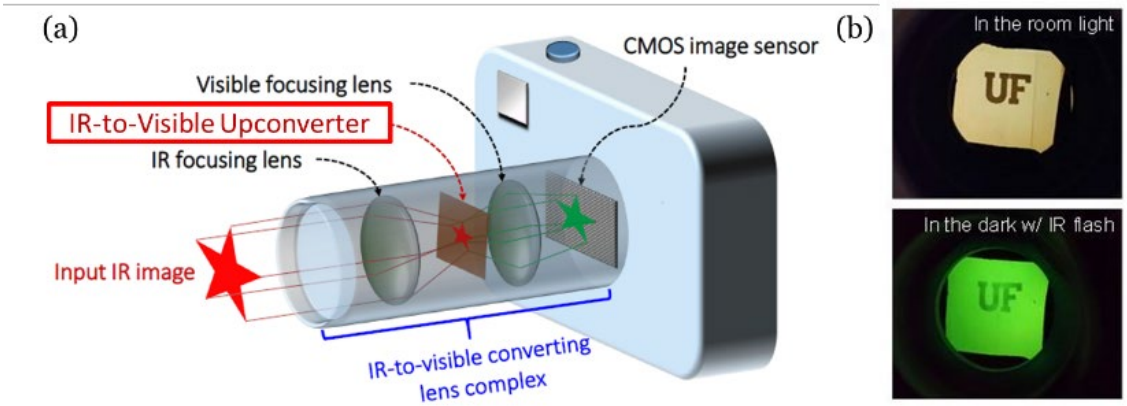

Figure 5 (a) Schematic diagram of the IR imaging camera with the IR sensitive OLED and (b) The photo images of the pixel-less IR imaging demonstration.

CHAPTER II

LITERATURE REVIEW

1. Emerging Organic Materials for Electronic Devices

Organic electronics has been growing because organic materials show the following promising characteristics. The most interesting part is that their optical and electrical properties can be easily modified by changing their molecular structure. Furthermore, organic materials are suitable for low-cost manufacturing because of low-temperature processing, such as thermal evaporation, and solution processing. Especially the solution process facilitates low-cost large-area fabrication by a printing method. For these advantages, various types of organic electronic devices have been developed and compete with conventional inorganic devices. Organic Light Emitting diodes (OLEDs)[25] are already commercialized and widely used in the consumer electronics market, and Organic Photovoltaics (OPVs)[26-28], Organic Thin Film Transistors (OTFTs)[29], Organic Photodetectors (OPDs)[5, 30-32], organic memory devices, and organic sensors are currently studied fields. In this dissertation, the component elements for the all-organic up-conversion devices, OLEDs and organic photodetectors are covered.

1.1. Potential of Organic Devices for Low-cost SWIR Imaging

In current organic devices like OLEDs, the production cost can be as low as 170 USD($)/$m^2$ with advanced deposition technique[33]. Using the organic materials to make the up-conversion devices, the estimated prices of standalone OLED-based SWIR camera is less than $500, because a typical price of a small OLED device (~1") is less than $10[34], and the camera part including optics is few hundred dollars[35]. This is tens of times less cost than the InGaAs camera which requires over than $20,000. If the SWIR up-converting devices are developed for the adapter-type devices for the existing cameras or smartphones, the device needs only optics and the up-conversion OLEDs with driving components. The cost for the adapter-type devices can be as low as $10. With further development on manufacturing technologies like printing process, the manufacturing cost will be much decreased.

2. Organic Light Emitting Diodes (OLEDs)

An Organic Light Emitting Diode (OLED) is a light emitting diode (LED) made with organic semiconductor materials. Figure 6 shows the basic structure of OLEDs. The OLED is made with multiple layers of organic semiconductor thin films. When a bias above the turn-on voltage of the OLED is applied to the device, the OLED emits bright light. Currently, OLEDs are widely used in display applications such as TVs, monitors, mobile phones, and smartwatches. Organic emitters have the advantage of wide color gamut, which results in highly vibrant color reproduction. And they are self-emitting devices, the black level can be completely dark, which makes the contrast ratio of the display infinity. Additionally, they can be fabricated on various substrates like thin metal foils and flexible plastic substrates. The flexibility allows the manufacturers to make ultimate form-factors; foldable mobile phones, and rollable TVs. These features have made OLEDs as the great display technology for the premium electronics market.

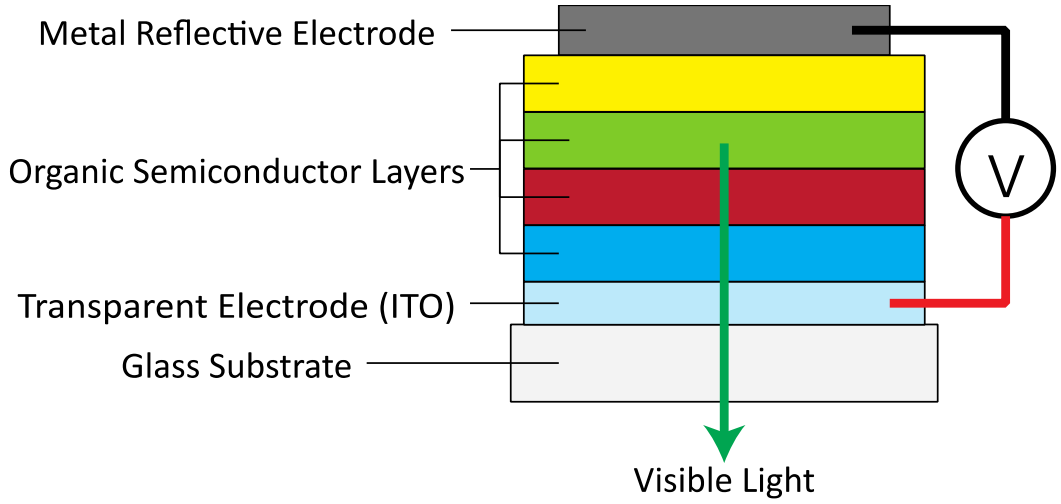

Figure 6 Schematic diagram of a basic OLED structure.

In 1963, M. Pope, *et al.* observed the electroluminescence in single-crystal anthracene[36], but its hundreds voltage for the operating device was too high due to few micrometers of large thickness. C. W. Tang *et al.* introduced a novel structure of the electroluminescent device in late 1987 as shown in Figure 7[37]. They demonstrated a double-layer structure of organic thin-film using evaporation. They achieved 1% photon/electron of external quantum efficiency, 1.5lm/W of power efficiency, and over 1,000cd/m^2 of brightness at under 10V of a driving voltage. The result showed a potential of commercializing OLEDs using a multi-layer of organic material. In 1989,

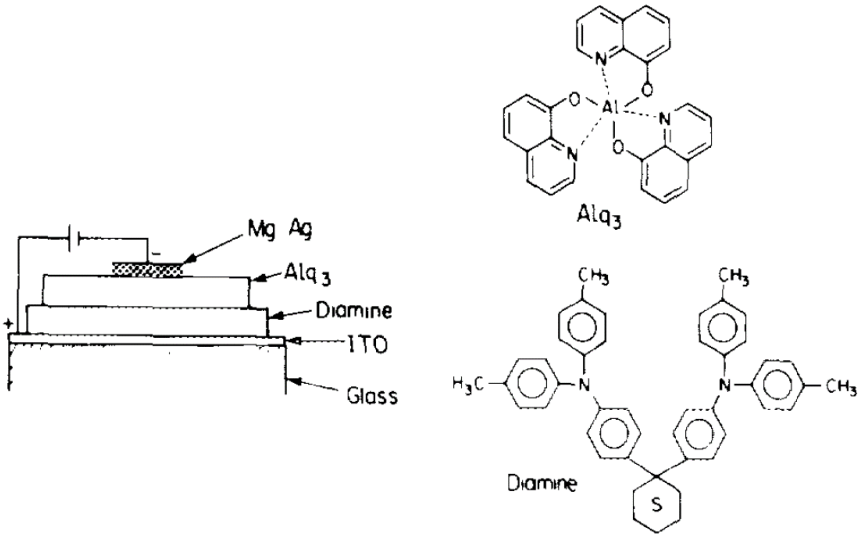

Figure 7 Configuration of the world first EL cell and molecular structures from C. W. Tang et al.

C. W. Tang *et al.* proposed a doping method that separates charge transfer and luminescence [38]. Since using phosphorescence through the doping method, the internal quantum efficiency (IQE) of OLED could be increased rapidly. The next big movement in OLEDs was a design of electro-phosphorescent device[39]. Forrest *et al.* used the red emitting phosphorescent dye 2,3,7,8,12,13,17,18-octaethyl-21H,23H-porphine platinum (II) (PtOEP) as dopant, achieved high IQE over than 90%.

2.1. The basic principle of Organic Light Emitting Diodes

2.1.1. The Structure of OLEDs

The OLEDs consist of several organic material layers between the anode and the cathode. Figure 8 shows the basic structures of OLEDs. To generate electroluminescence (EL), first, electrons and holes need to be injected from the anode and the cathode, respectively. Then injected electrons and holes are transferred to the Emission Layer (EML) and they recombine. For efficient charge transfer, there are multiple organic layers in the OLED structure. The Hole Injection Layer (HIL) helps the hole injection from the anode to organic layers. The Hole Transport Layer (HTL) and the Electron Transport Layer (ETL) delivers the injected holes and electrons to EML, respectively.

2.1.2. Emission process in EML of OLEDs

In the emission process of OLEDs, holes and electrons form a singlet or triplet state. The singlets can relax with emitting light, but the relaxation of triplets is non-radiative. Figure 9 (a)[40] shows the spin alignment schema for triplets and singlet. The three triplet states have total spin angular momentum of S=1, and the one singlet state has a spin angular momentum of S=0[40]. We can assume that the ratio of singlets and triplets is 1:3 by simple spin statistics, and that gives us the value of η_{st} will limit the maximum internal efficiency of the device to 25% [41].

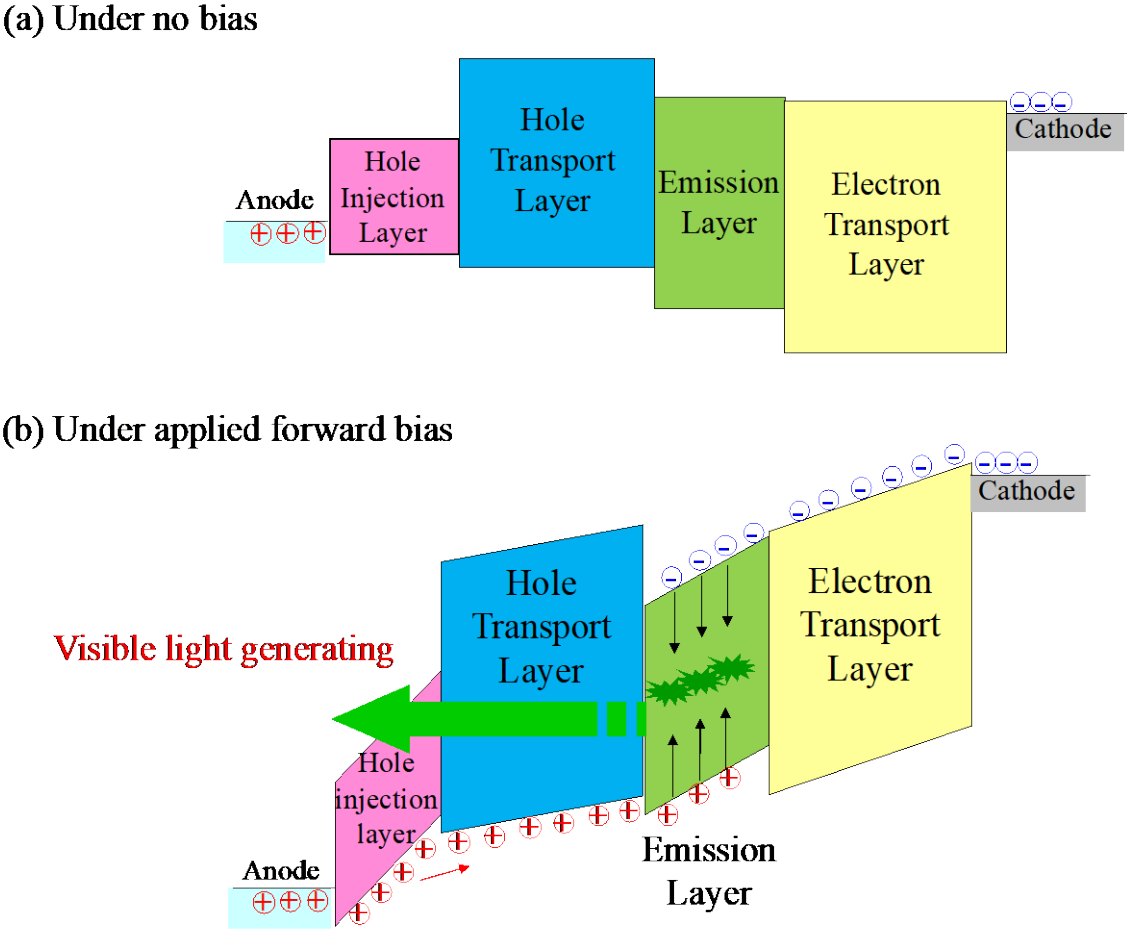

Figure 8 The basic structure of the OLED (a) without external bias condition, and (b) under forward bias condition.

Non-radiative relaxation occurs in the process of relaxation from triplet states in OLEDs due to selection rules: the relaxation from triplet states requires the flip of spin to follow the Pauli Exclusion Principle. This decay process has a longer lifetime for radiation, therefore non-radiative process occurs predominantly. But phosphorescent radiation can occur when spin-flip arises by interaction with impurities and defects.

The guest dopant, heavy mass element organo-metallic phosphors, can enhance the light emission by phosphorescence. Figure 9 (b) shows transitions occur in the host-guest system. Singlet energy transfer from the host material to the guest material can occur via Foster of Dexter energy transfer, but triplet transfer can occur only via Dexter energy transfer [42, 43]. These transfers can

make that all excitons move to guest material. Some studies reported almost 100% of internal light efficiency using PtOEP[44], and $Ir(ppy)_3$[45].

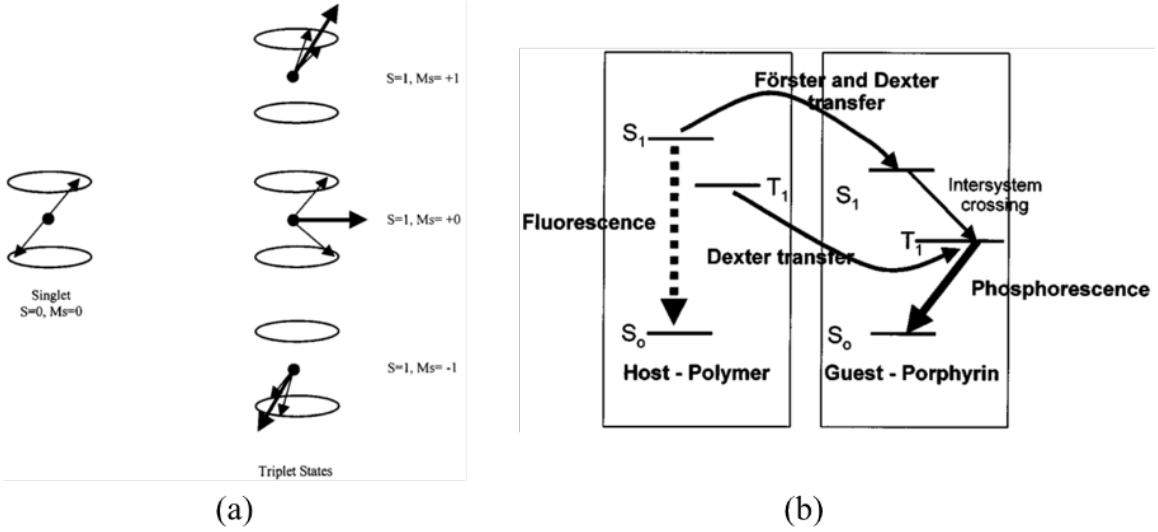

Figure 9 Schematic representations of (a) the spin alignments for the one singlet and three triplet states, and (b) the fluorescent and phosphorescent transitions for host–guest systems.

3. Organic Photodetectors

For the photodetection application, organic materials also are attractive due to their strong absorption in the visible and near-infrared (IR) regions, color selectivity, and compatibility with low-cost roll-to-roll processing. Most of the organic photodetector (OPD) studies have currently been focused on the visible applications[46] for enhancing the performance of a complementary metal-oxide semiconductor (CMOS) image sensor.[47-50] Conventional CMOS image sensors require the integration of Si-based PDs with color filters for full-color imaging. However, organic semiconductors can function as the photoactive layer in the photodetectors as well as the color filters in the image sensor because of the relatively narrow absorption spectra of organic semiconductors compared to their inorganic counterparts. Because of their unique features, OPDs can potentially replace Si-PDs for sensor applications. In addition, the use of organic PDs can improve the sensor sensitivity in the near-IR region due to the large absorption coefficients of

many organic materials (>1.0×10^5 cm^{-1}) at wavelengths above 700 nm, which are significantly higher than the corresponding values for silicon (< 2.0×10^3 cm^{-1}) due to its indirect nature of the bandgap.[50] Therefore, it is especially advantageous to use near-IR OPDs for near-IR imaging applications. Furthermore, the study of infrared detection in OPDs is also important because the infrared sensitivity of OPDs can extend their applications to the military, security, scientific, and medical areas. Figure 10 shows the basic structure for organic photodetectors. They consist of few organic semiconductor layers that absorb the light (photon) or transport photogenerated electrons and holes to the cathode and the anode.

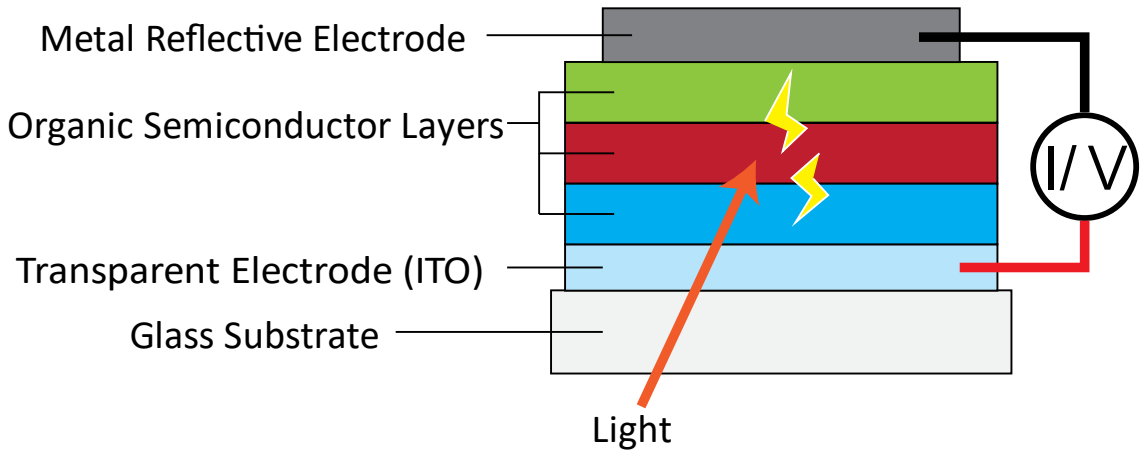

Figure 10 Schematic diagram of a basic organic photodetector structure.

3.1. The basic principle of Organic Photodetectors

3.1.1. Photo-generated excitons in organic semiconductors

The excited state generated by absorption of a photon is called an exciton, which is a bound state of an electron-hole pair. The exciton generation in organic semiconductors can be described by an energy band diagram as shown in Figure 11. An incident photon causes excitation of the electron from a ground state to an excited state. The excited electron in the excited state and the hole in the

ground state form excitons. Due to the high exciton binding energy (>1 eV) in organic semiconductors, it is difficult to get free carriers without any additional supports. To dissociate the photo-generated excitons in organic semiconductors, OPDs require extra energy such as external electrical field.[30]

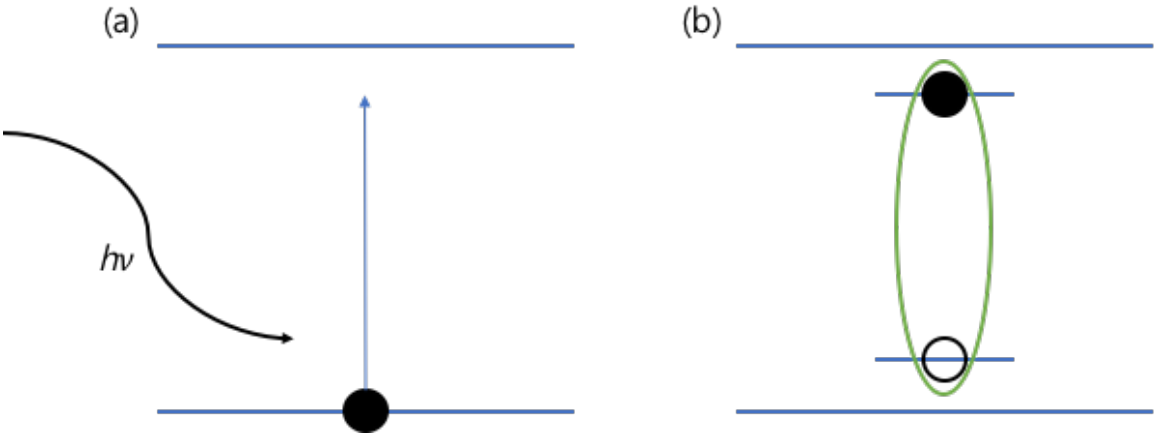

Figure 11 Schematic diagram of (a) excitation of electron, and (b) exciton

3.1.2. Donor-Acceptor interface for charge dissociation.

To increase charge dissociation, the donor and acceptor (D-A) model is employed.[5] As shown in Figure 12, two materials with different energy band form interface that photoinduced charge separation occurs. The interface in this state is a charge transfer (CT) state which has relatively low exciton binding energy to facilitate charge dissociation because the D-A energy offset is relatively higher energy than the energy that binds exciton.[51, 52] Therefore, donor-acceptor bilayers are typically used as the photoactive layer in OPDs.

In donor-acceptor bilayer OPDs, the photoactive layers composed of donor and acceptor semiconducting organic materials are sandwiched between two electrodes. The donor material donates electrons and mainly transports holes and the acceptor material withdraws electrons and mainly transports electrons. As depicted in Figure 10, those photoactive materials absorb photons

to form excitons, in which electrons are excited from the valence band into the conduction band (Light Absorption). Due to the concentration gradient, the excitons diffuse to the donor/acceptor interface (Exciton Diffusion) and separate into free holes (positive charge carriers) and electrons (negative charge carriers) (Charge Separation). A photo-detection is completed when the holes and electrons move to the corresponding electrodes by following either donor or acceptor phase (Charge Extraction).

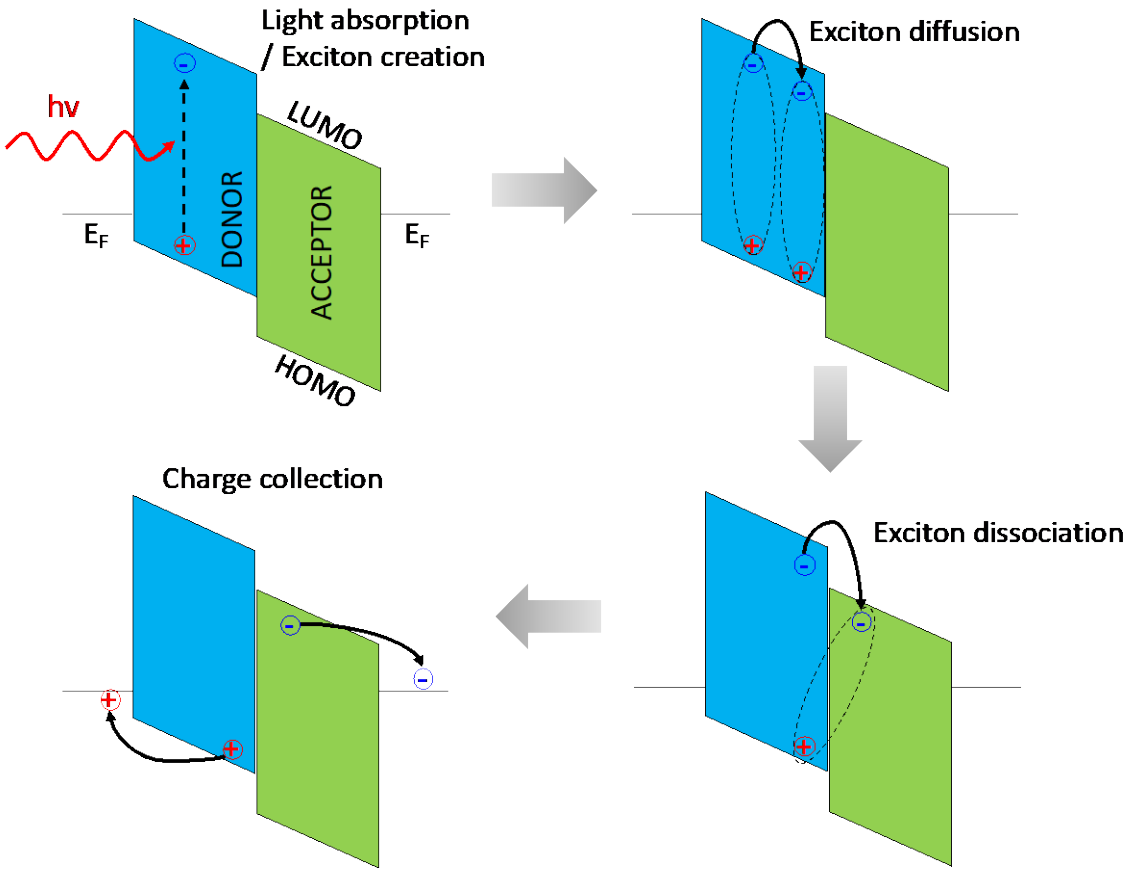

Figure 12 Basic processes in organic light sensitizing layer visualized in a schematic energy diagram of a D–A cell. E_F are the Fermi energies of the cathode and anode contacts, respectively. LUMO is the lowest unoccupied molecular orbital, and HOMO is the highest occupied molecular orbital of the organic film.

3.1.3. Bulk heterojunction (BHJ) for enlargement of the interface area

The first demonstration of OPD was reported by Kudo and Moriizumi in 1981.[53] They showed the potential of spectral selective absorption capability of organic materials. They employed a bilayer of merocyanine and rhodamine B to adopt a donor-acceptor structure as shown in Figure

13. However, the D-A combination can be fabricated by two methods. One way is a formation of D-A planar heterojunction as in the work of Kudo and Moriizumi[53], and another is making a mixture of the donor and acceptor materials. Blend of the D-A materials forms bulk heterojunction (BHJ) layer that the distribution of heterojunction is across the whole layer.[27, 54, 55] Figure 13 shows the different type of heterojunctions. Figure 13 (a) is the planar bilayer, in which two thin-film layers are only stacked. The interface area is only between two layers. Figure 13 (b) shows the typical BHJ made by mixing two materials, thus the interface area between two materials is increased significantly. The ideal BHJ structure is shown in Figure 13 (c). The interface area is maximized, while each acceptor and donor materials are connected, respectively, thus, photogenerated charges can move through each channel to be collected by each electrode. In the aspect of device structures, OPD looks remarkably similar to OPV. But there are several different key factors between OPDs and OPVs. The most significant difference is the operation condition. While photo-generated charge carriers in OPVs must be extracted by an internal built-in potential, charge carriers in OPDs can be extracted by an external electric field due to an

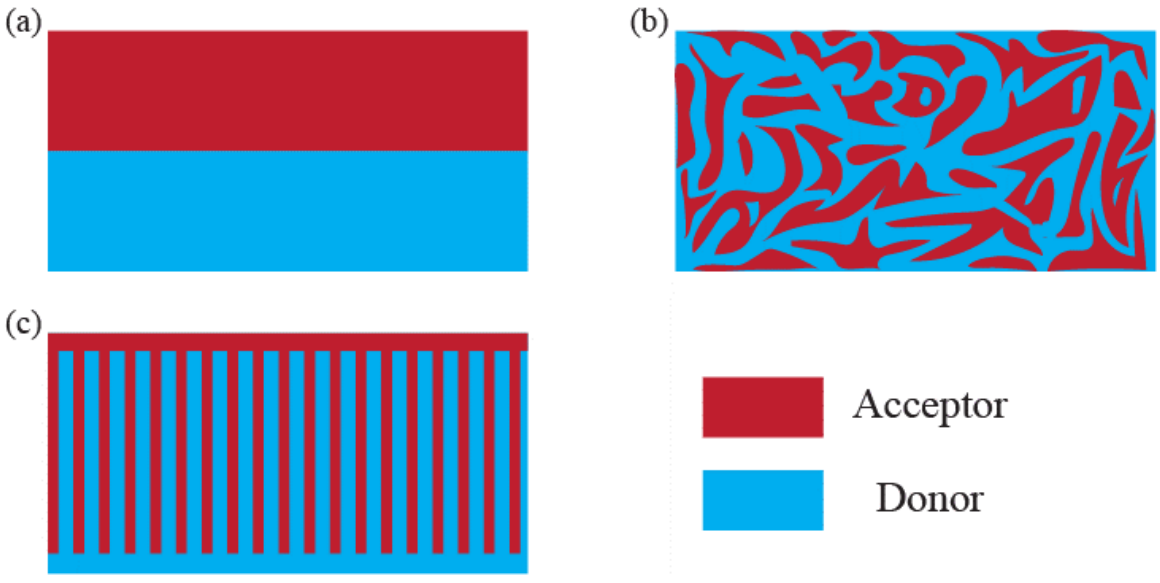

Figure 13 Schematic representation of, a) bilayer, b) bulk-heterojunction (BHJ), and c) ideal BHJ OPV device.

applied reverse bias. Therefore, charge carrier extraction can be further enhanced by this applied reverse bias.

4. Infrared-to-Visible Up-conversion OLEDs

Recently, optoelectronic devices based on organic materials have received a lot of attention because of their compatibility with large area manufacturing that enabling a high-quality image at a significantly low cost.[5, 56-58] IR-to-visible up-conversion OLEDs have a similar structure compared with conventional OLEDs as shown in Figure 14 (a)[17]. Except for the solution-processed PbSe CQD IR sensitizing layer, IR-to-visible up-conversion OLEDs can be fabricated by a simple vacuum thermal evaporation process that is currently being used in a manufacturing line of OLED displays. Without IR light irradiation, light emission from the IR-to-visible up-conversion OLED was not observed until the voltage reached 17 V as shown in Figure 14 (b). Upon irradiation with IR light, the device turned on at 8 V along with an onset of green light emission, and thus the light emission modulation by IR light is clearly demonstrated.

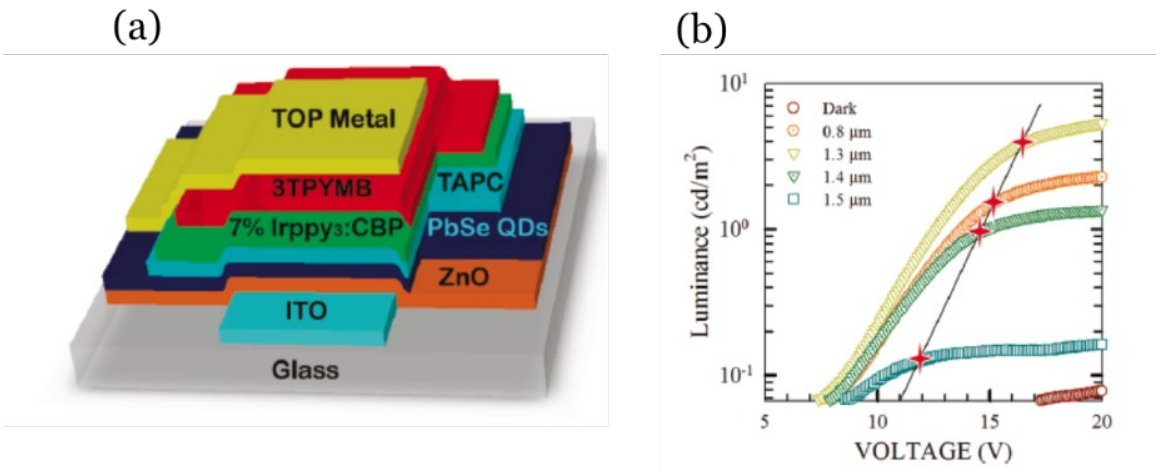

Figure 14 (a) Schematic cross-section view and (b) Photo (under IR illumination) L-V characteristics of the IR-to-visible up-conversion OLED with PbSe QD as the IR sensitizer.

4.1. Basic Principle of Up-conversion OLEDs

4.1.1. Working Mechanism of the Up-conversion OLEDs

A schematic energy band diagram of IR-to-visible up-conversion OLEDs is shown in Figure 15 [17]. The device is basically an OLED with an IR sensitizing layer. The key to IR sensitive OLEDs is to keep the device in an off state even if a forward voltage is applied to the device and turn on the device only with IR light. To keep the device off under forward bias, a hole blocking layer

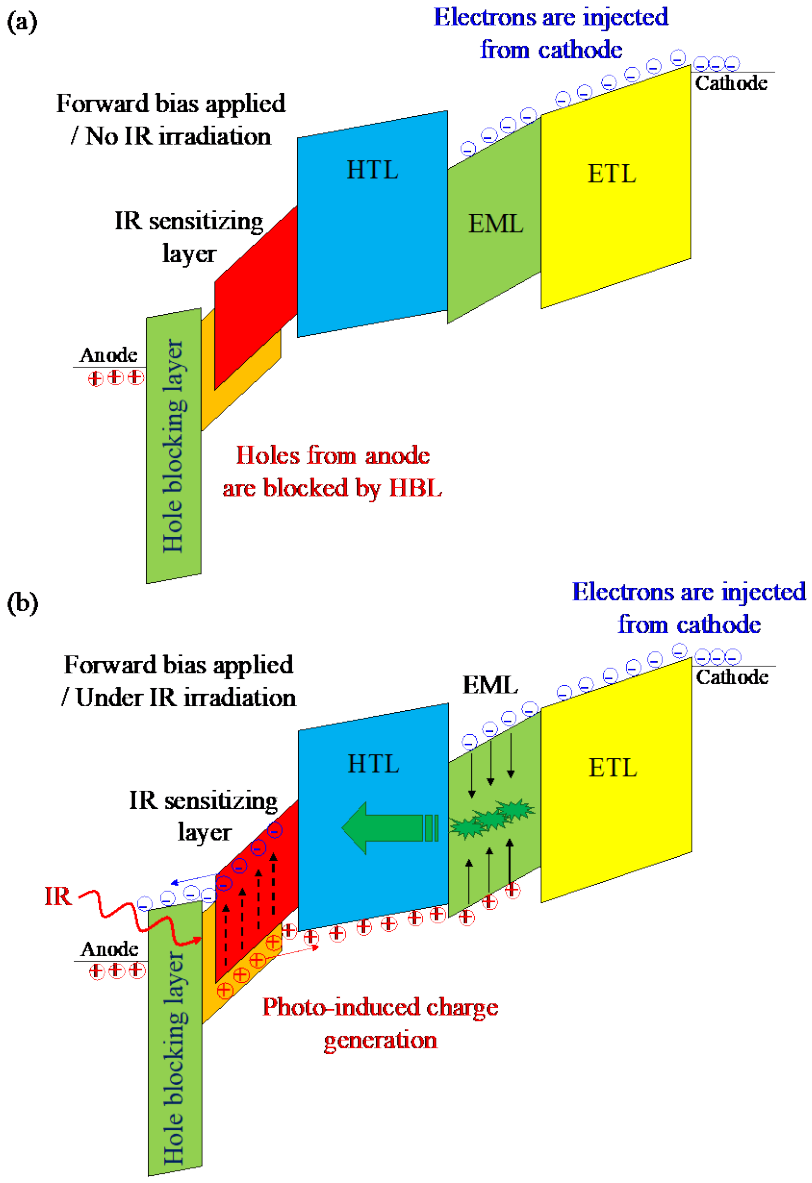

Figure 15 Schematic energy band diagrams of IR-to-visible up-conversion OLED (a) in the dark and (b) in the IR illumination.

(HBL) is inserted between the ITO anode and the IR sensitizer to block hole injection from the anode. Under IR irradiation, photo-generated holes in the IR sensitizing layer are injected through the hole transport layer (HTL) into the emitting layer of the OLED and recombine with electrons injected from the cathode to emit visible light.

4.1.2. Figures of Merits of Up-conversion Devices

4.1.2.1. Photon-to-Photon Conversion Efficiency

The IR-to-visible photon-to-photon conversion efficiency (η_{con}) is the figure of merit for evaluating the performance of an IR-to-visible up-conversion OLED and is then given by the following equation:

$$\eta_{con} = \frac{\#\ of\ emitted\ photons}{\#\ of\ incident\ photons} = \frac{\int \frac{\lambda I_{photo}(\lambda)}{R(\lambda)hc} d\lambda}{\frac{\lambda_{IR} P_{IR}}{hc}}$$

where h is the Planck's constant, c is the speed of light, λ is the wavelength of the emitted light, I_{photo} is the photocurrent measured by the photodetector used for the measurements, $R(\lambda)$ is the responsivity of the photodetector, λ_{IR} is the wavelength of the incident infrared light, and P_{IR} is the incident infrared power.

4.1.2.2. Turn-on Voltages and Operation Voltage Window

Other figures of merit for up-conversion devices are the dark turn-on voltage and the operation voltage window as shown in Figure 16. The operation voltage window is defined as the voltage difference between the dark turn-on voltage (V_{dark}) and the IR illuminated turn-on voltage (V_{IR}). The IR-to-visible up-conversion OLEDs can be operated as the IR sensors representing their on/off characteristics under IR excitation within the operation voltage window.

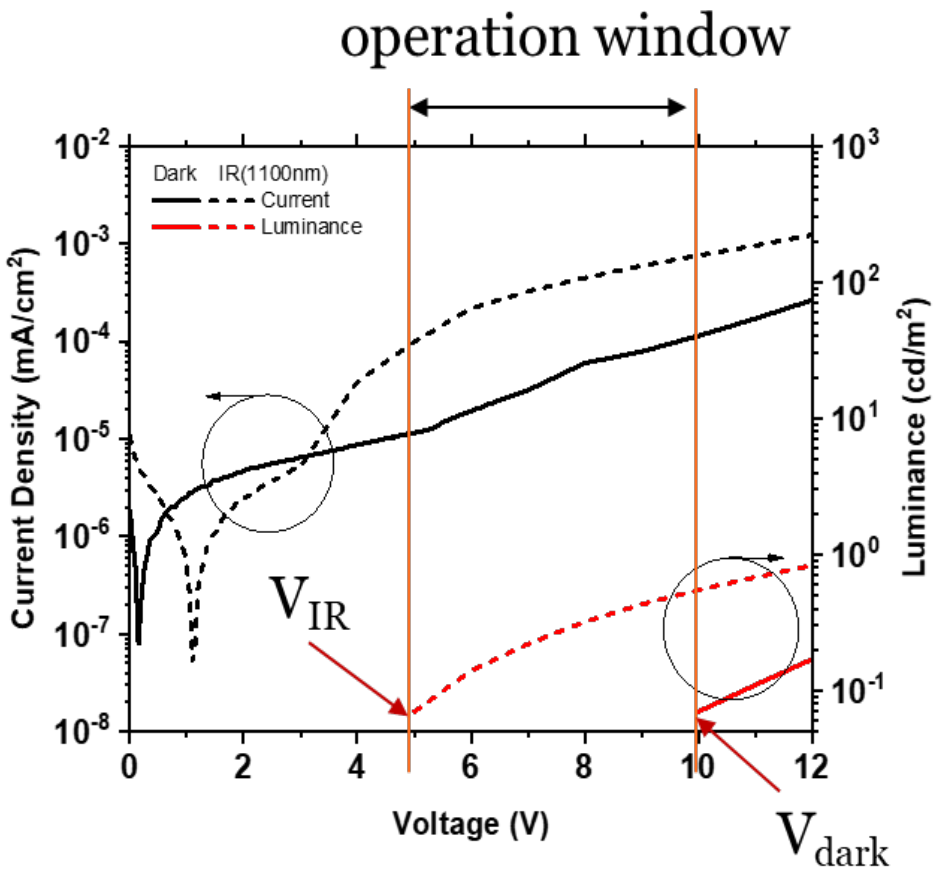

Figure 16 Current-Voltage-Luminance characteristic of an IR-to-visible up-conversion OLED.

CHAPTER III

RESEARCH MOTIVATION AND OBJECTIVES

1. Motivations

1.1. Remaining issue on the Current SWIR-to-visible Up-conversion OLEDs

In current IR-to-visible up-conversion OLEDs, a solution based PbS/PbSe colloidal quantum dots (CQD) was employed as the SWIR sensitizing layer.[17] PbS/PbSe CQDs with excellent photosensitivity, bandgap tunability, and solution processability provide an attractive platform for low-cost epitaxial free SWIR photodetectors with strong IR sensitivity in SWIR wavelengths (700 - 3000 nm)[59-61] as shown in Figure 17[17]. However, it is incredibly challenging to synthesize monodispersed PbS/PbSe CQDs. Also, large volume synthesis of PbS/PbSe CQDs is still under development and thus mass production of PbS/PbSe CQDs is not ready. Therefore, other low-cost epitaxial-free SWIR sensitizers are required for realizing low-cost SWIR imaging products based on IR-to-visible up-conversion OLEDs.

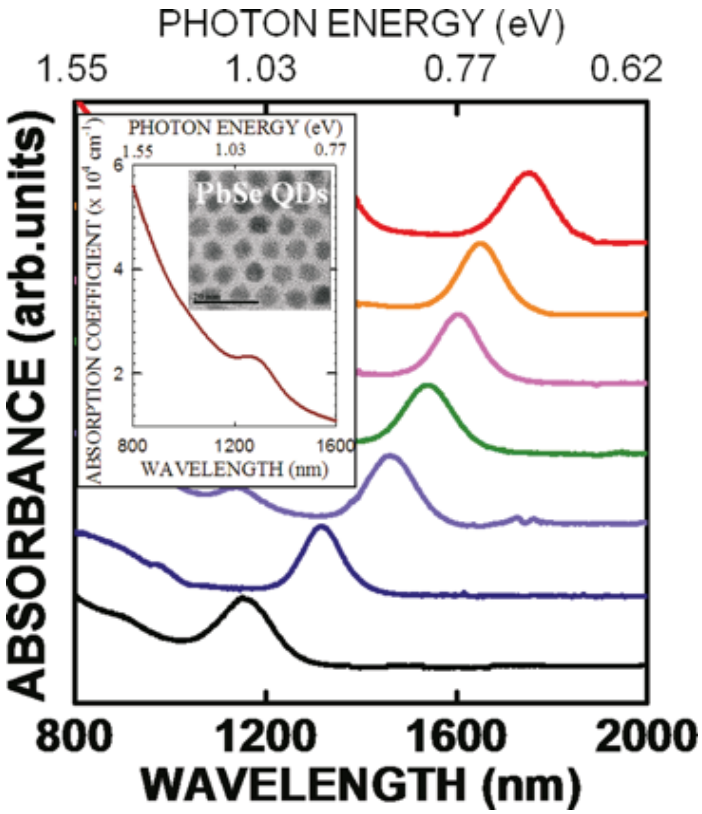

Figure 17 Absorbance spectra of PbSe CQDs with various sizes. (Inset: Absorption coefficient spectrum and TEM image of 50nm thick PbSe QD film with 1.3μm peak wavelength.)

1.2. Advantages of Organic Light Sensitizers

As light sensitizers, organic materials are attractive for visible and near-IR sensing applications due to their intrinsic advantages such as strong optical absorption in visible/near-IR wavelengths and absorption band selectivity.[47, 49, 62-67] Moreover, their inherent compatibility with printable and large-area processing methods makes them a promising material for low-cost, flexible applications.[5, 54] Until now, most organic semiconductors, which have been synthesized especially for solar cell applications, show a strong photo-response in the visible range shorter than 700 nm. A few low-bandgap organic materials have recently been reported with a near-IR response beyond 800nm, thus making them a potential alternative to Si for NIR applications.[3, 68, 69] By further engineering molecular structure of organic semiconductors, therefore, their optical

bandgap can be further lowered, resulting in SWIR sensitivity beyond 1000 nm which Si-based photodetectors cannot offer. By using a SWIR sensitive low-bandgap organic IR sensitizer, all-organic SWIR-to-visible up-conversion OLEDs can be realized for low-cost SWIR imaging applications.

2. Specific Aims

In this dissertation, the research aims to achieve low-cost SWIR-to-visible up-conversion OLEDs using organic SWIR sensitizer to replace CQD sensitizers. For the all-organic up-conversion OLEDs,

- **Objective 1: Low-bandgap organic donor materials with SWIR sensitivity**

Hypothesis 1-1: Low bandgap polymers

The investigation of new polymers' design to lower their bandgap, able to cover the SWIR spectrum, can be accomplished following the rule based on the electron-withdrawing/donating building blocks strategy. Alternating units with different electron-withdrawing/donating abilities in a polymer backbone, it is possible to modulate the gap between the highest occupied molecular orbital (HOMO) and the lowest unoccupied molecular orbital (LUMO). Especially, low band-gap polymers require extraordinarily strong units in terms of electron-withdrawing/donating abilities.

Hypothesis 1-2: Low bandgap small molecules

Commercially available low-bandgap small molecules for a SWIR sensitizing layer can be explored by the extended conjugation approach. A phthalocyanine family is a popular material system for small molecule-based organic photovoltaic and detecting devices. Holmes and coworkers reported that IR sensitivity can be extended by the elongated conjugation from the

addition of aromatic rings on the molecule.[70] The additional conjugated aromatic rings on the phthalocyanine framework have also enhanced the absorbance in the IR region.

- **Objective 2: Proper acceptors with appropriate energy alignment with the low-bandgap organic donors**

Hypothesis 2: Energy level alignment effect in the sensitizing layer

Even though we successfully find very low-bandgap organic semiconductors by either synthesis as well as purchasing, it is very challenging to fabricate SWIR photodetectors as well as SWIR-to-visible up-conversion OLED by using the low-bandgap organic semiconductors because of the nature of the excitonic material with strong binding energy. As excitonic materials, organic semiconductors generate excitons, which is strongly bounded electron-hole pairs, by absorbing photons irradiated. The exciton dissociation is required to get photogenerated current but the photo-generated excitons in organic semiconductors need external forces to be dissociated to electron and hole carriers. In typical organic photovoltaic and detecting devices, therefore, the donor/acceptor system, which is a mixing of two organic semiconductors: an electron donor and an electron acceptor, is used for the exciton dissociation because excitons are easily dissociated at the material interfaces with different HOMO and LUMO levels. For the ideal exciton dissociation, the LUMO level of the accepter material is lower than the LUMO of the donor material. But when the LUMO level of the acceptor has a small offset with the HOMO level of the donor material, the charge generation effect occurs under small bias. This effect results high dark current in the device which affect the performance of the devices. The combination of donors and acceptors with an appropriate energy alignment is vital for efficient exciton dissociation in organic SWIR sensitizer.

- **Objective 3: Hole Blocking Layer for preventing dark current in up-conversion OLEDs**

Hypothesis 3: The HOMO level effect of the hole blocking layer

For the operation voltage window, the IR-to-visible up-conversion OLED is to keep the device in off-state while a voltage is applied to the device, and the device will only turn-on when infrared light is incident onto the device. Ideally, it needs to keep the device off even a large voltage is applied to the device. This can be done by suppressing the injection of one type of carrier. Therefore, controlling the charge injection is critical to the operation of these IR-to-visible up-conversion OLEDs. While the operation of up-conversion devices has been demonstrated, the effect of charge injection on device performance has not systematically studied previously. A good hole blocker needs to extract photogenerated electrons efficiently for avoiding unwanted charge accumulation while blocking hole injection from ITO anode. The HOMO of the hole blocker should be deep enough to block hole injection from ITO anode, and we need to minimize the energy barrier between the LUMO of the hole blocker and the IR sensitizing layer.

CHAPTER IV

EXPERIMENTAL METHODS

1. Device Fabrication

1.1. Substrate Preparation

Pre-patterned ITO coated glass substrates were first cleaned with acetone and isopropyl alcohol in an ultrasonic cleaner for 15 minutes each and then rinsed with de-ionized water. The Bransonic CPX2800 ultrasonic bath, shown in Figure 18 (a), was used for ultrasonic cleaning. The cleaned

Figure 18 (a) Bransonic CPX2800 ultrasonic bath and (b) Jelight Model 18 UVO-Cleaner.

substrates were dried by nitrogen blowing. For the regular structure devices, which the ITO works as the anode, the ITO glass substrates were subsequently treated with UV-O_3 for 30 minutes. This treatment is to reduce the work function of ITO, which enables better hole injection from the ITO anode to the device. Figure 18 (b) shows Jelight Model 18 UVO-Cleaner. In this study, UV-O_3 surface treatment was performed in the atmosphere.

1.2. Spin-coating

Spin-coating is a thin film deposition process using centrifugal force to make uniform films onto a flat substrate. The vacuum from the center of the chuck, which the substrate is placed on, holds the substrate during the spin-coating process. Because the spin-coating process is a solution process, a precursor solution is required to prepare. The result of the thickness of the deposited film is related to the concentration of the solution and the rotation speed of the spin-coater. This method is usually used for the deposition of polymer materials, and various ceramics including metal oxides. In this study, two spin-coaters shown in Figure 19 were used for the solution process; one in the air for PEDOT:PSS and metal oxide, and one inside the nitrogen glovebox for organic materials.

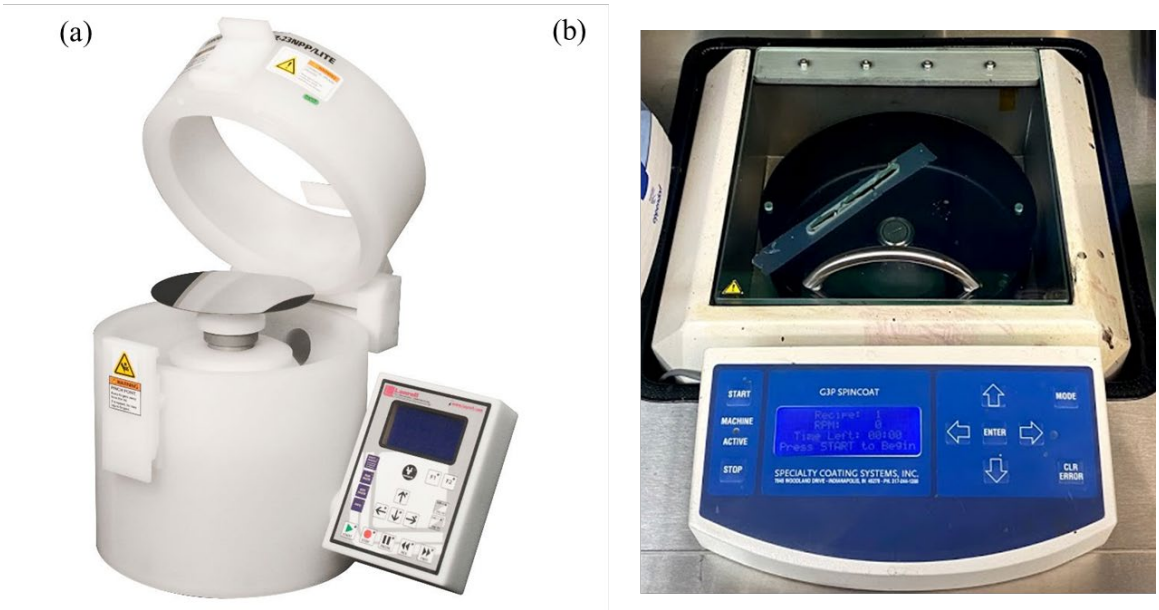

Figure 19 The pictures of the spin-coaters. (a) Laurell WS-650MZ-23NPPB, and (b) SCS G3P Spin coater.

1.3. Thermal Evaporation

The thermal evaporation is one of the physical vapor deposition techniques. The thermal evaporation is usually in a vacuum below 10^{-6} Torr. Heated evaporation source emits vaporized materials, and the gas condenses on the substrate. This method is generally used for organic small molecules, some ceramic materials, and metal deposition.

Figure 20 shows the evaporation system used in this study. Using cryopump, we maintain the vacuum level of the chamber in order of 10^{-7} Torr during evaporation. The vacuum chamber is connected inside of the glove box with nitrogen ambient, and it protects both the vacuum chamber and the materials from oxygen and moisture exposure.

(a)

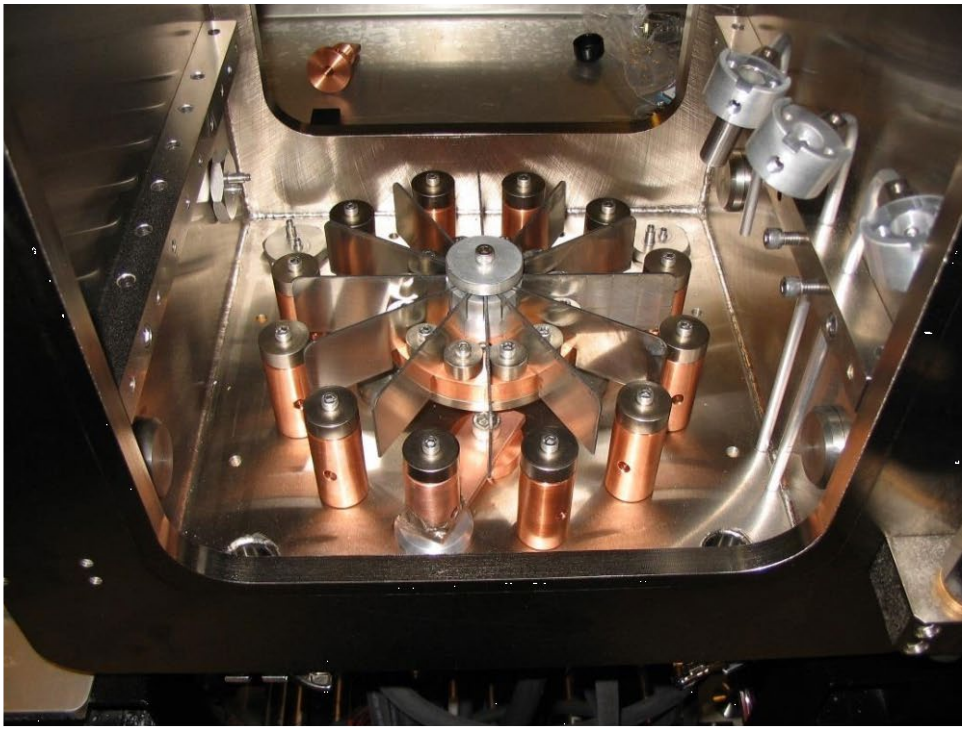

(b)

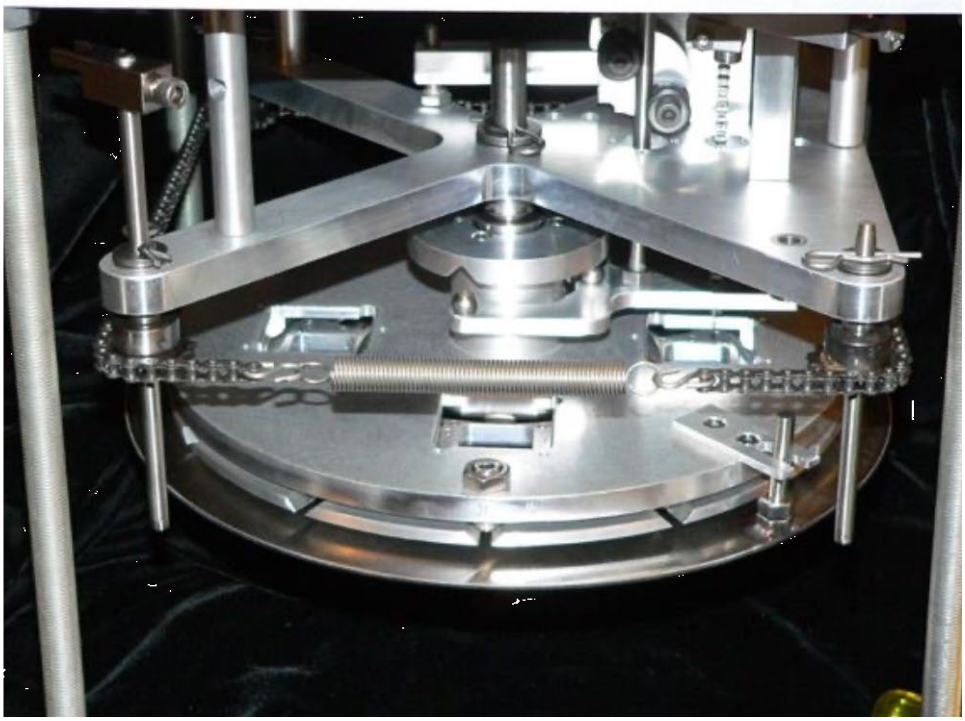

Figure 20 Inside view of the vacuum chamber for thermal evaporation. (a) 12-source-heating system with divider, and (b) the rotating substrate holder with a mask and shutters assembly.

1.4. Encapsulation

After fabrication, the encapsulation to prevent oxygen and moisture from the organic devices is performed inside the nitrogen atmosphere. Thus, the devices can be free from contact with the moisture and oxygen after fabrication. In this study, cavity glass covers, and UV-resin were used for encapsulation. Figure 21 shows the UV curing system with the fixture.

Figure 21 UVP Blak-Ray™ B-100AP High-Intensity UV Inspection Lamps with Exposure Box

2. Device Characterization

2.1. Photodetector Characterization

2.1.1. Current density-Voltage (J-V) Characteristics Response

The J-V characterization is conducted using Keithley 2400 source meter by measuring the current through the device while sweeping the voltage, as shown in Figure 22. For photodetectors, the J-V characteristics under monochromatic light are compared with the characteristics in dark condition.

Figure 22 Keithley 2400 source meter

2.1.2.Spectral Responsivity / External Quantum Efficiency (EQE)

Spectral Response of the photodetector was measured using an in-house setup, the McScience K3100 test system, consisting of calibrated Si and InGaAs photodiodes for the reference EQE, a Xenon DC arc lamp, a monochromator, a current amplifier, a chopper, and a lock-in amplifier. The Xenon lamp generates full spectrum of light, and the filters and the monochromator select specific wavelength of light to get the electric response from the device at a single wavelength. The chopper and the lock-in amplifier make light alternated to compare the dark current and the current while irradiation. The current difference between the dark and irradiated conditions is used for the calculation of the responsivity and the EQE. Figure 23 shows the schematic diagram of the system with the actual picture.

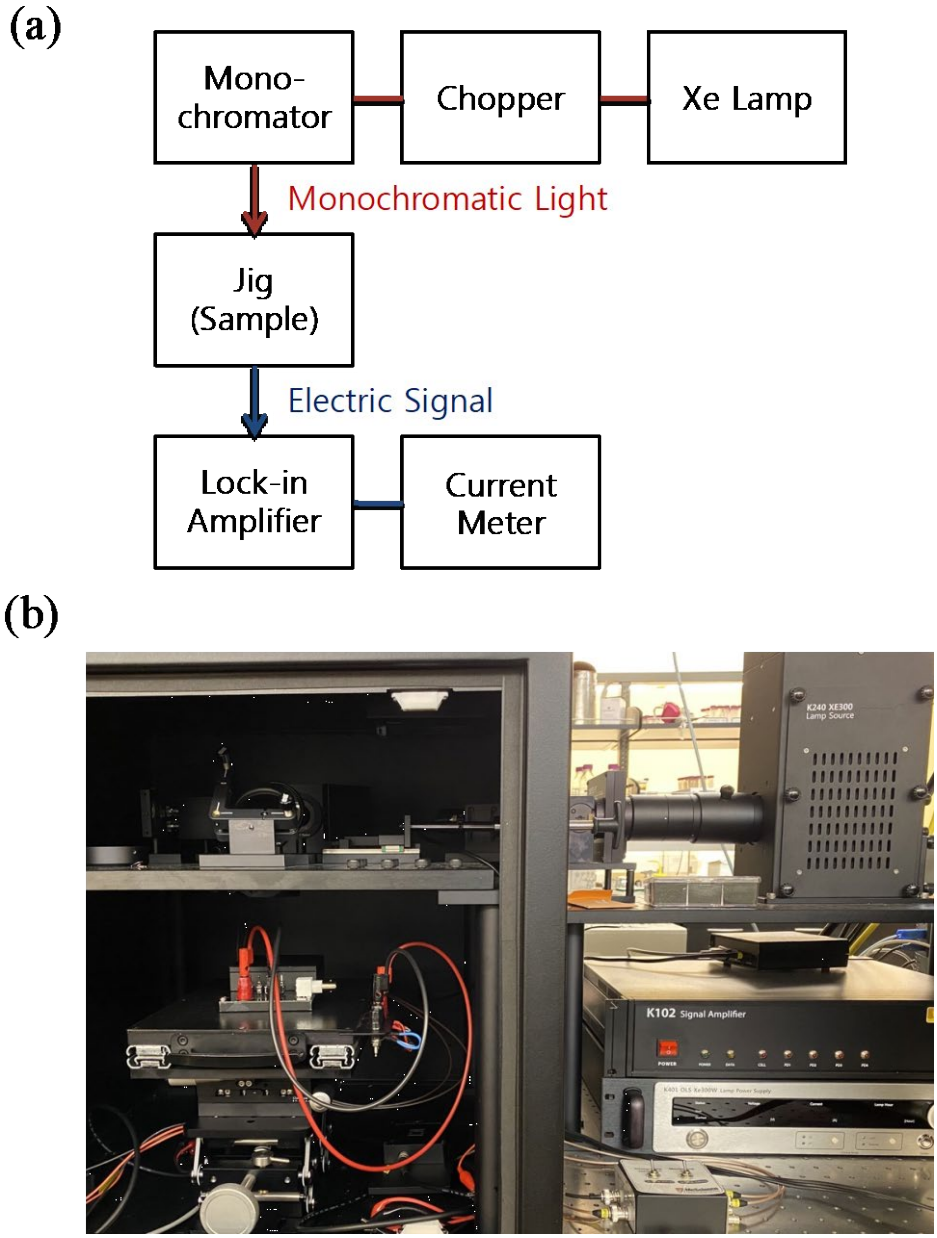

Figure 23 (a) Schematic diagram and (b) Actual picture of spectral response measurement setup

2.2. Up-conversion OLED Characterization: J-V-L Characteristics Response

Luminance-current-voltage (LIV) characteristics of the IR sensitive OLEDs were measured using an in-house setup by integrating the McScience M3000 OLED test system and the McScience K3100 EQE test system, consisting of a Photo Research PR-670 spectroradiometer, a Keithley 2400 source meter, calibrated Si and InGaAs photodiodes, a Xenon DC arc lamp, a

monochromator, a current amplifier, a chopper and a lock-in amplifier. The devices were encapsulated, and the measurements were carried out at room temperature under ambient atmosphere. This special setup for the characterization of the up-conversion device was required because the LIV measurement needs to be performed while IR is irradiated to the sample. A novel measurement setup was designed to meet the requirements for the up-conversion device characterization. Figure 24 shows the final design of the measurement setup. The IR light coming from the monochromator is reflected in the adjustable mirror and irradiates the sample in the jig. The emitted light extracted from the sample is measured by the PR670 spectrometer, while the current and voltage are measured by Keithely 2400 SourceMeter.

(a)

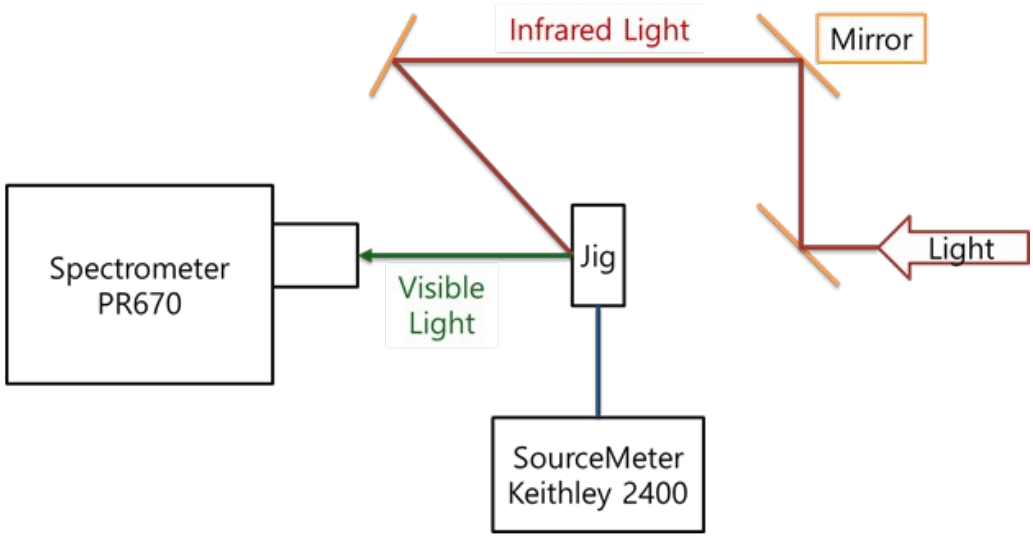

(b)

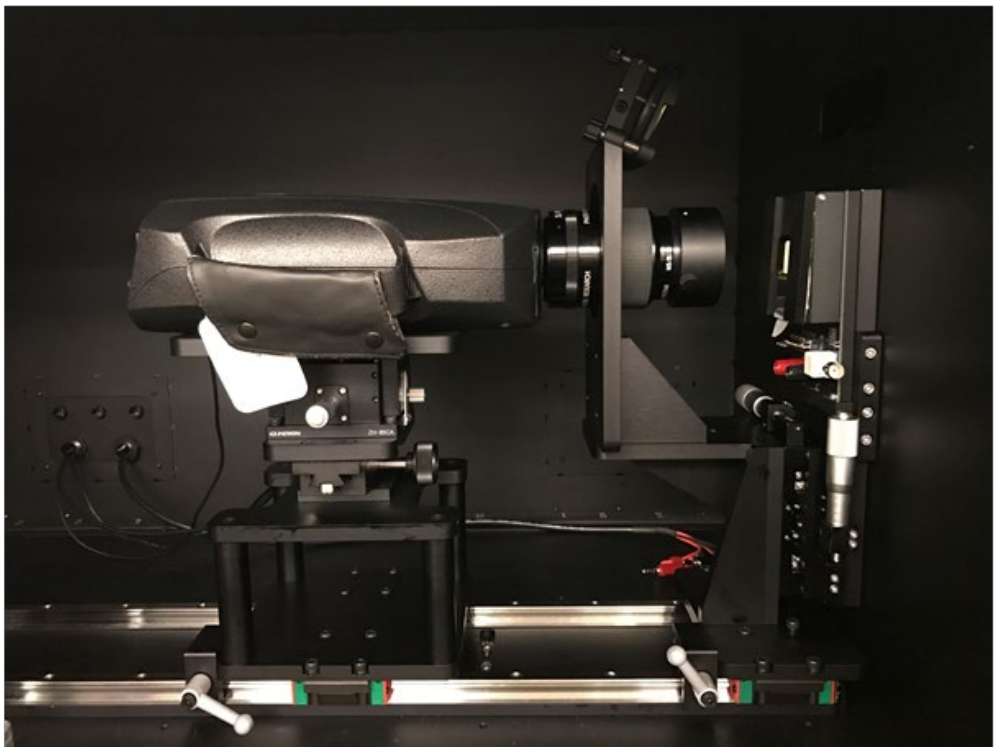

Figure 24 The up-conversion characterization system. (a) Schematic diagram, and (b) the picture of the actual setup in a dark box.

CHAPTER V

SWIR SENSITIVE LOW BANDGAP ORGANIC MATERIALS

1. Introduction

Organic optoelectronic materials are currently widely used in commercial products (e.g. OLED, liquid-crystal display, and organic solar cell), but their focus has been on ultraviolet (UV) and visible light range (250-700nm)[71]. Recently, infrared detection is emerging due to interesting applications in photonics and telecommunications. Detecting photons at longer IR wavelengths requires lower-band-gap organic semiconductors. Organic semiconductors are attractive for visible and near-IR sensing applications due to their intrinsic advantages such as strong optical absorption in visible/near-IR wavelengths and absorption band selectivity.[72-75] Moreover, their inherent compatibility with printable and large-area processing methods makes them a promising material for low-cost, flexible applications.[76-79] Until now, most organic materials, which have been synthesized especially for solar cell applications, show a strong photo-response in the visible range shorter than 700nm.[55, 80, 81] A few low-band-gap polymers have recently been reported with a near-IR response beyond 800 nm, thus making them a potential alternative to Si for near-IR applications. [74, 75, 82-84] By further engineering the molecular structure of polymer semiconductors,

therefore, their optical band gap can be further lowered beyond 1100 nm which Si-based photodetectors cannot offer.[75] There are two types of organic materials: organic small molecules including organometallic compounds containing a transition metal, and conjugated polymers. In this chapter, the strategy to achieve a low bandgap for both small molecules and polymers will be described and demonstrated their optical and electrical properties.

2. SWIR Sensitive low-bandgap polymer: PBDTT-BTQ

2.1. Approach for low-bandgap polymer

The investigation of the new polymer's design, able to cover the near IR spectrum, has been accomplished following the rule based on the electron-withdrawing/donating building blocks strategy.[85] Alternating units with different electron abilities in a polymer backbone, it is possible to modulate the gap between the Highest Occupied Molecular Orbital (HOMO) and the Lowest Unoccupied Molecular Orbital (LUMO) in the region of interest, with regard to the band offset.

$$\left[\mathrm{D}-\mathrm{A}\right]_n \leftrightarrow \left[\overset{+}{\mathrm{D}}=\overset{-}{\mathrm{A}}\right]_n$$

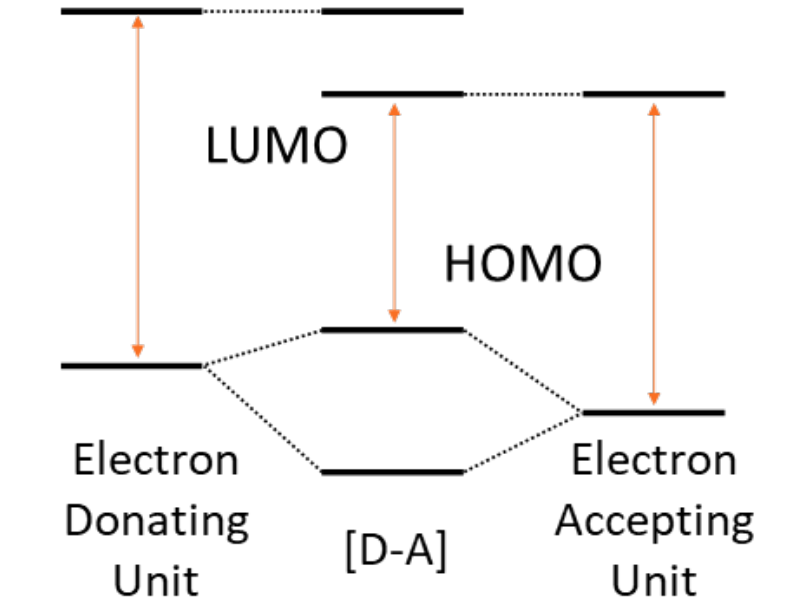

Figure 25 Schematic energy band diagram of the electron donating-accepting unit in the polymer molecule.

In specific, every low band gap polymer[74, 86-88] requires very strong units in terms of electron-donating and electron-withdrawing abilities to be combined, followed by a cautious HOMO LUMO level alignment between Acceptor and Donor material used in the active layer, as shown in Figure 25. In fact, the shrinking of the HOMO-LUMO band gap reduces the effective working window for a good charge transfer between the species, and careful modulation of HOMO and LUMO levels of the Donor (low bandgap polymer) not too far from the ones of the Acceptor (PCBM) for disfavoring losses mechanisms, needed to be addressed.

2.2. Novel Low-bandgap Polymer Synthesis: PBDTT-BTQ

In the landscape of strong electron-withdrawing units, a specific building block attracts the attention being employed in a low bandgap polymer with an unprecedented E_{opt} of 1 eV for organic solar cell (OSC) and photodetector (PD) applications.[89] The unit based on thiadiazolo[3,4]quinoxaline named BTQ turned out to be an optimal aspirant for reaching near IR absorption's peak. In that contribution, the BTQ based polymer showed a very promising value of noise equivalent power (NEP) as low as 2×10^{-9} W, which is one of the important aspects in photo-sensor to get a very high detectivity. Since then the BTQ based polymers have been employed in a few OSC and transistor works,[90-98] further insights were needed on this motif mainly persistent on PD.

Among the strong electron-donating units, particular attention to the Benzodithiophene (BDT) based structure has been considered. Thanks to the easy synthetic approach nonetheless its declared versatility demonstrated in many performing polymers for OCS[99], the BDT core structure turned to be a good candidate to fulfill the requirement for an affordable and performing polymer. In particular, 4,8-bis(5-(2-butyloctyl)thiophen-2-yl)benzo[1,2-b:4,5-b']dithiophene commonly (BDTT), thanks to the presence of additional thiophene rings influencing the planarity

of the polymer backbone, it is well known for broadening the absorption patterns[100, 101], feature essential for application in IR photodetectors.

A novel low bandgap polymer, Poly 4-(4,8-bis(5-(2-butyloctyl) thiophen-2-yl) benzo[1,2-b:4,5-b′] dithiophen-2-yl)-6,7-diethyl-[1,2,5]thiadiazolo[3,4-g]quinoxaline (PBDTT-BTQ) was synthesized by using the electron-withdrawing/donating building blocks strategy with a strong collaboration with Dr. Beaujuge group, King Abdullah University of Science and Engineering (KAUST). The chemical reaction equation is shown in Figure 26.

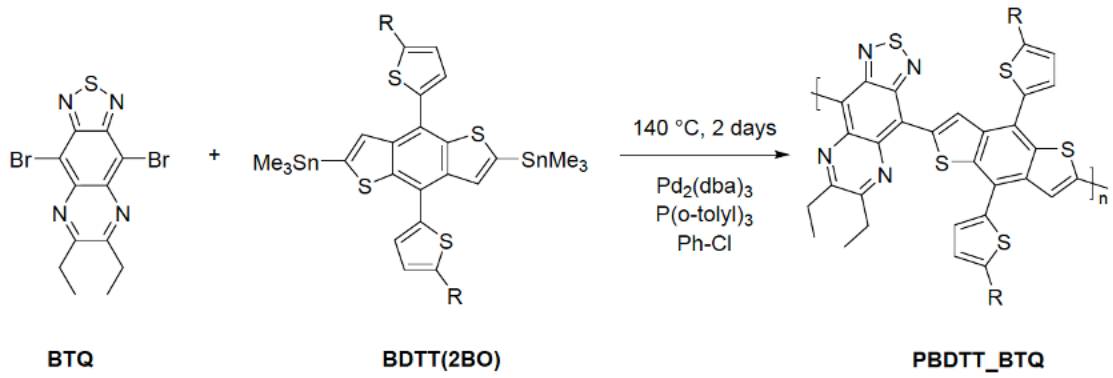

Figure 26 Synthesis of poly 4-(4,8-bis(5-(2-butyloctyl)thiophen-2-yl)benzo[1,2-b:4,5-b']dithiophen-2-yl)-6,7-diethyl-[1,2,5]thiadiazolo[3,4-g]quinoxaline (PBDTT-BTQ)

Monomer BDTT(2BO) (0.29 mmol) was combined with monomer BTQ (0.29 mmol), a stir bar, tris(dibenzylideneacetone)dipalladium (7.9 mg, 8.7×10^{-3} mmol) and tri-*o*-tolylphosphine (11.5 mg, 3.8×10^{-2} mmol) in a 10 mL microwave reaction vial. The reaction vial was subjected to five vacuum-nitrogen cycles. Then, freshly degassed chlorobenzene (5 mL) was added to the vial and the reaction mixture was stirred for 2 days in oil bath at 140 °C. The mixture was slowly precipitated into methanol (100 mL). The precipitate was filtered through a Soxhlet thimble and purified *via* consecutive Soxhlet extractions with acetone (6 h) followed by dichloromethane (12 h), and the polymer was finally collected with chloroform. The organic solution was concentrated by evaporation, precipitated into methanol (100 mL), and the polymer residues were filtered off. The Mn and Mw were performed in GPC at 130 °C using trichlorobenzene as eluent and

calibration using polystirene as standard. The fractionation (Fr 1-2) of the two Mn values has been performed using GPC in chlorobenzene at 90°C.

Table 1 Polymer Properties of PBDTT_BTQ

Polymer	**name**	**Quantity/Yield**	**Mn (KDa)**	**Mw (KDa)**	**PDI**
PBDTT_BTQ	Fede325	240mg/89%	38.4	97.2	2.5

2.3. Optical properties of PBDTT-BTQ

PBDTT-BTQ showed a strong photo-response in SWIR wavelengths of 700−1200 nm as shown in Figure 287. PBDTT-BTQ shows a significantly high absorption coefficient of over 1×10^4 cm^{-1} for near-IR wavelengths of 800-1100 nm compared to Si with low absorption coefficients of 1×10^3 - 1×10^1 cm^{-1} for near-IR wavelengths of 800-1100 nm.[102] The absorption onset is around 1,200 nm, corresponding to a bandgap of ~1.0 eV. The HOMO level of PBDTT-BTQ was measured by photoelectron spectroscopy in air (PESA) and is -4.8 eV as shown in Figure 28. The LUMO level of PBDTT-BTQ is -3.8 eV, which was obtained by using the optical bandgap and the HOMO level of PBDTT-BTQ.

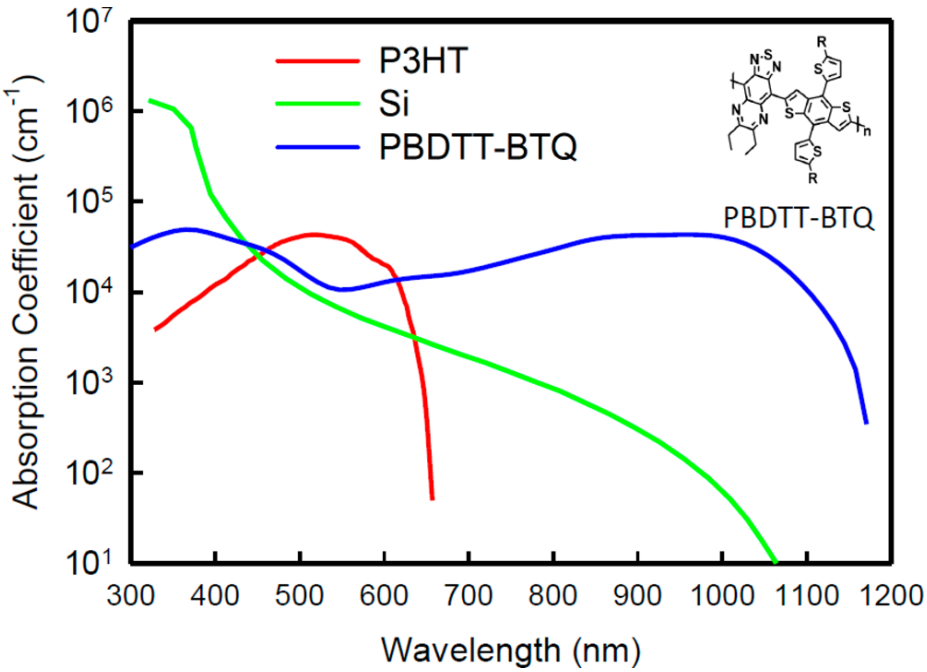

Figure 27 Comparison of absorption coefficients of Si, P3HT (film), and PBDTT-BTQ (film).

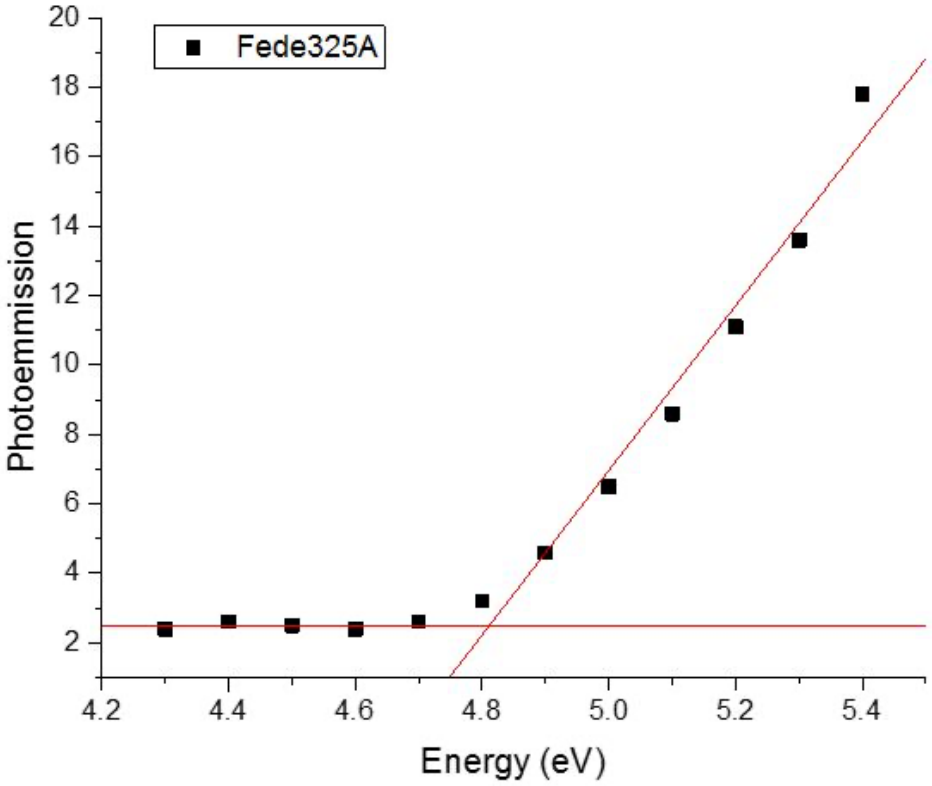

Figure 27 Photoelectron spectroscopy in air (PESA) measurement of the PBDTT-BTQ for HOMO energy level

3. SWIR Sensitive low-bandgap small molecule: $SnNcCl_2$

3.1. Approach for low-bandgap small molecule

To improve the OPDs' competitiveness, their absorption spectra need to be extended further to the infrared area. Extension of the photoresponse to longer infrared wavelengths could be achieved by the employment of the low-bandgap organic semiconductors for an absorption layer. Commercially available low-bandgap small molecules for a SWIR sensitizing layer can be explored by the extended conjugation approach as shown in Figure 29. Holmes and coworkers reported that IR sensitivity can be extended by the elongated conjugation from the addition of

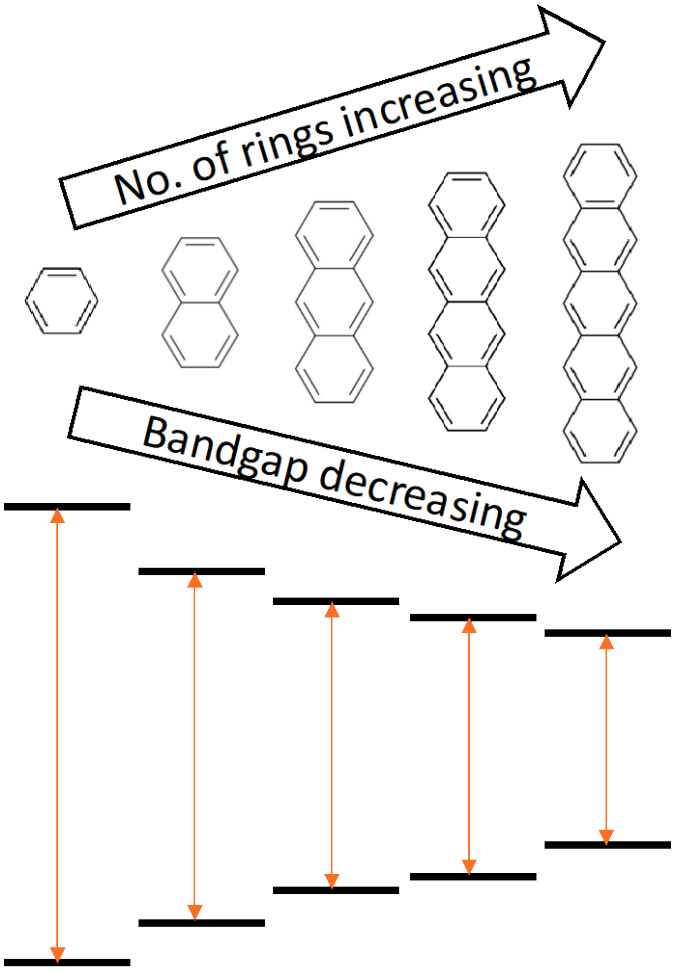

Figure 28 Schematic diagram for showing extended conjugation approach. The number of aromatic ring increment results the bandgap reduction.

aromatic rings on the molecule.[70] The additional conjugated aromatic rings on the phthalocyanine framework have also enhanced the absorbance in the IR region.

3.2. Low-bandgap small molecule selection

The most common small molecule materials for near-IR OPDs are cyanine derivatives, such as metal phthalocyanines.[103-113] Zhang, et al. demonstrated transparent NIR OPDs using heptamethine cyanine dye, Cy7-T.[69] They achieved the absorption of ~900nm with 850nm peak absorption wavelength. Lv, et al. introduced $NdPc_2/C_{60}$ Heterojunction OPD.[104] They utilized exciplex absorption to achieve the absorption of ~900nm. Lead phthalocyanine(PbPc)/C_{60} Heterojunction OPD was demonstrated by Wang, et al.[103] PbPc absorbed broadly on 600nm to 1000nm, and the absorption spectrum extended to 1100nm. One of the most promising candidates is tin naphthalocyanine dichloride ($SnNcCl_2$).[65] Pandey, et al. fabricated organic solar cells with $SnNcCl_2$,[114] and three papers on OPDs with O-$SnNcCl_2$,[115, 116] and $SnNcCl_2$.[65] The utilization of $SnNcCl_2$ will extend infrared absorption to ~1200nm. Furthermore, Jakubikova, et el. reported that the absorption peak can be moved toward longer wavelengths by modification of the functional group on $SnNcCl_2$ molecule.[117] A commercially available low-bandgap small

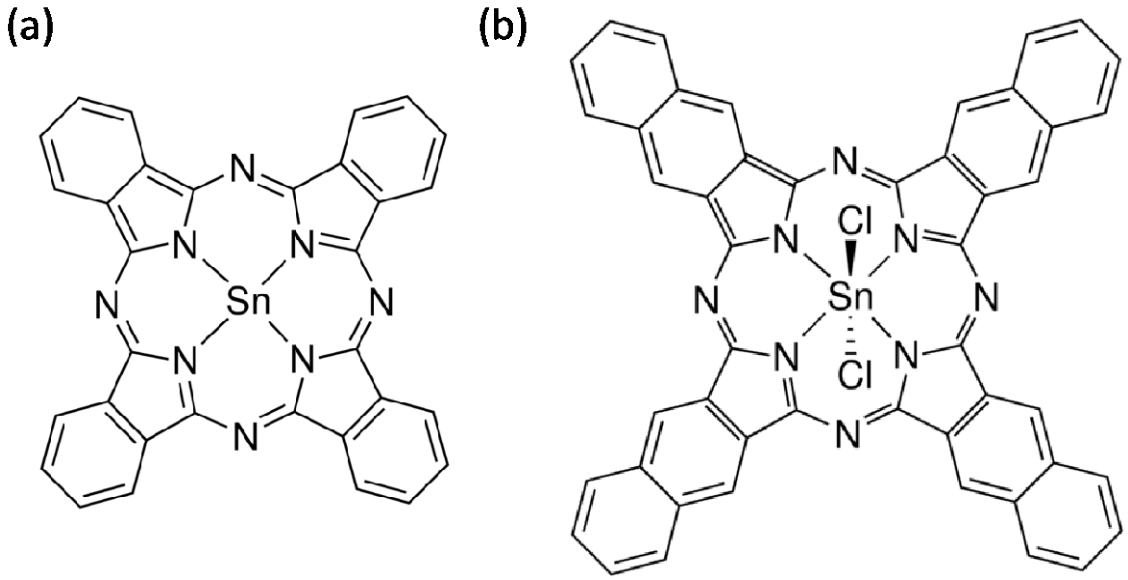

Figure 29 Chemical structures of (a) SnPc, and (b) $SnNcCl_2$.

molecule material, $SnNcCl_2$ was selected by following elongated conjugation strategy adding aromatic rings on the phthalocyanine-based small molecule as shown in Figure 30 (a) and (b). Because $SnNcCl_2$ has longer benzene rings comparing to SnPc, it is expected that $SnNcCl_2$ features lower bandgap and longer-wavelength SWIR absorption.

3.3. Optical property of $SnNcCl_2$

Figure 31 is the comparison of the absorption coefficient spectrum of pristine $SnNcCl_2$ film along with the spectra of conventional organic visible/NIR sensitizers, CuPc and SnPc, and the spectrum of Si as a reference. $SnNcCl_2$ shows a significantly high absorption coefficient of over 1×10^4 cm^{-1} for SWIR wavelengths of ~1,200nm compared to Si with low absorption coefficients of 1×10^3 - 1×10^1 cm^{-1} for wavelengths of 800-1100 nm. The absorption onset is around 1,400 nm, corresponding to an optical bandgap of ~0.9 eV.

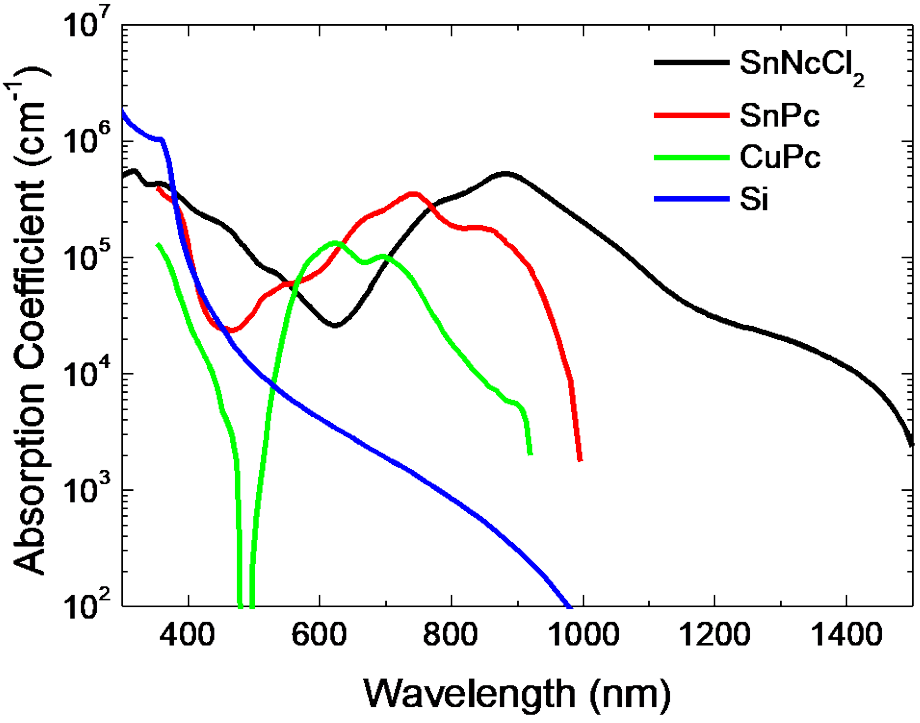

Figure 30 The absorption coefficient spectra of $SnNcCl_2$ and other photovoltaic materials.

The ultraviolet photoelectron spectroscopy (UPS) measurements were performed using a modified VG ESCA Lab system, an ultrahigh vacuum (UHV) system equipped with a He discharge lamp. The base pressure of the spectrometer chamber is typically 8×10^{-11} torr. The UPS spectra were recorded by using unfiltered He I (21.2 eV) excitation as the excitation source with the sample biased at -5.00 V to observe the low-energy secondary cutoff. The UV light spot size on the sample is about 1 mm in diameter. The typical instrumental resolution for UPS measurements is 0.1 eV.

The highest occupied molecular orbital (HOMO) level of $SnNcCl_2$ measured by UPS is -4.91 eV, as shown in Figure 32. The lowest unoccupied molecular orbital (LUMO) level of $SnNcCl_2$ is -4.01 eV, and its bandgap is 0.9eV.

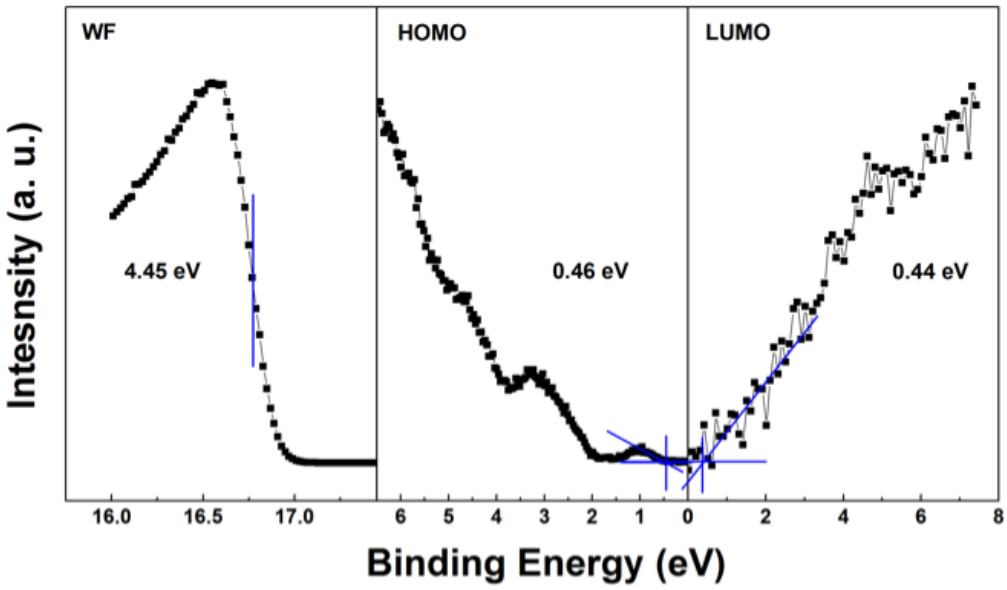

Figure 31 The UPS spectra of $SnNcCl_2$. The work function is 4.45 eV, HOMO offset is 0.46 eV, and LUMO offset is 0.44 eV. Therefore, the band gap is 0.90 eV, and the ionization potential is 4.91 eV.

CHAPTER VI

SWIR SENSITIVE ORGANIC PHOTODETECTORS USING LOW-BANDGAP ORGANIC MATERIALS

1. Introduction

Near-infrared (NIR) photodetectors have been used in optical communication, imaging, security, ranging, and consumer electronics[118-122]. Especially, NIR organic photodetectors have been attracted great attention because it has advantages such as low-cost fabrication, large-area detection, tunable response spectrum, lightweight, flexibility, and chemical versatility[123-126]. In the organic photodetectors, their sensitizing part consists of donor-acceptor (D-A) structure, because the organic materials are excitonic materials which have a relatively high binding energy requires donor-acceptor structure to dissociate exciton and get photocurrent.[127] The donor and acceptor materials need to have proper energy level offset for efficient exciton separation. Especially for SWIR sensitizing materials, due to their extremely low bandgap, energy band offset effects on the performance of the photodetector significantly. In this chapter, photodetectors using SWIR sensitive polymer and small molecule were demonstrated and their sensitizing layers were studied.

2. The Figure of merit for the photodiodes: Specific Detectivity (D*)

The figure of merit for exhibiting the performance of a photodetector is the specific detectivity (D*). The D* is the most important parameter to describe photodetector's performance. To understand D*, first, the Noise Equivalent Power (NEP) needs to be cleared. The NEP is the light power when S/N ratio is 1. It can be written as

$$\mathrm{NEP} = \frac{\mathrm{S_{noise}} \cdot \sqrt{\Delta f}}{R} \qquad (1)$$

where $\mathrm{S_{noise}}$ is the noise spectral density in units of $\mathrm{A}/\sqrt{Hz}$, and Δf is the bandwidth (BW) in unit of Hz. The reciprocal of NEP is detectivity D of the device. D can determine D*be normalized with BW Δf, and device area A. to be useful unit of the comparison for photodetectors. The normalized D is referred to as the specific detectivity D* which is

$$D^* = \frac{\sqrt{\Delta f \cdot A}}{\mathrm{NEP}} \qquad (2)$$

in unit of Jones ($\mathrm{cm}\sqrt{Hz}/\mathrm{W}$). In OPDs, the shot noise from the dark current is the dominant contribution.[74] Then, we can re-write D* as

$$D^* = \frac{R}{\sqrt{2qJ_{\mathrm{dark}}}} = \frac{EQE\sqrt{q}}{h\nu\sqrt{2J_{\mathrm{dark}}}} \qquad (3)$$

where J_{dark} is the dark current density, R is the spectral responsivity, and EQE is the external quantum efficiency. Yao, et al. reported in 2007, the experimental result of the device noise current was matched well with the calculated shot noise.[128]

As shown in equation (3), the keys for performance improvement of the photodiode are an increase of the responsivity and reduction of J_{dark}. The EQE is the percentage of the extracted electrons from the device by the incident photons to the device. It is also called the incident

photon-to-current efficiency (IPCE). The higher EQE indicates better performance on photodetection. The responsivity is the ratio between the input light power and the output current. The EQE and the responsivity are determined by the following equations:

$$R=\frac{I_{ph}}{P_{opt}} \qquad (4)$$

and

$$EQE=\frac{R\ h\nu}{q} \qquad (5)$$

where I_{ph} is the photocurrent, P_{opt} is the power of incident light, $h\nu$ is the energy of the incident photon, and q is the element electron charge, respectively. When the incident light power is fixed, the EQE is determined by the photocurrent of the device. Therefore, people focus on the photocurrent enhancement to get higher EQE.

The value of the dark current in a photodetector can vary by several orders of magnitude depending on the device architecture.[75] Under reverse bias, a major source of dark current is charge injection from the electrodes. To lower this dark current in a photodetector, therefore, it is especially important to suppress charge injection considerably from both electrodes. In SWIR-sensitive organic photodetectors, low dark currents are more challenging due to the narrow bandgap of NIR-sensitive organic materials and thus it is important to have an electron blocking layer (EBL) and a hole blocking layer (HBL) inserted between the electrodes and the photoactive layer to reduce its dark current, as shown in Figure 33. Additionally, the minimization of the dark current results in lower power consumption of OPDs.

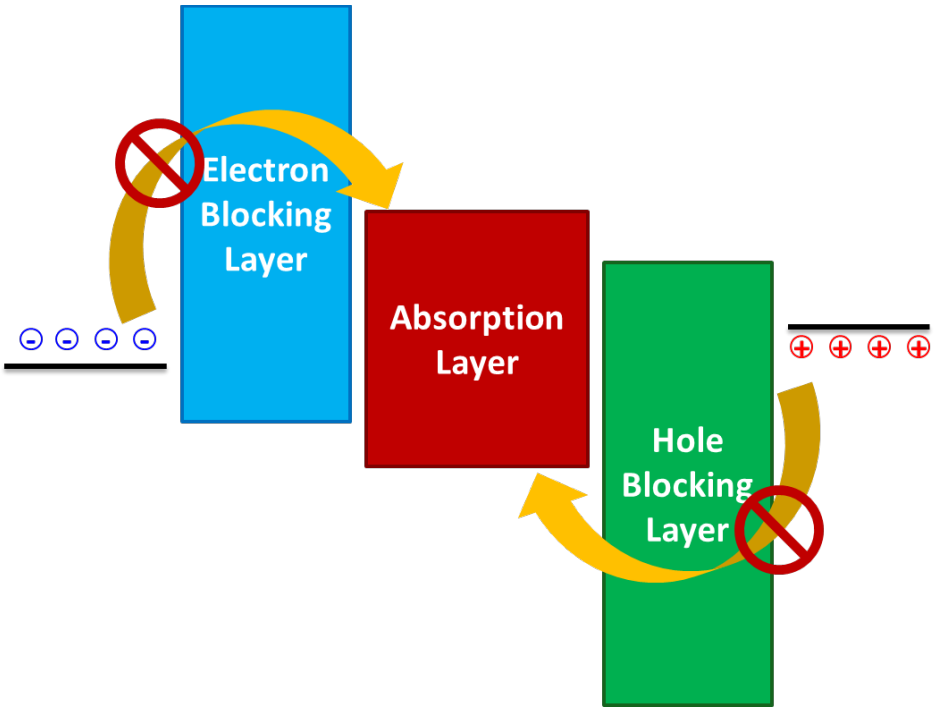

Figure 32 Schematic energy band diagram of the photodetector structure.

3. SWIR photodetector using PBDTT-BTQ as a SWIR sensitizer

3.1. Evaluation of the photoelectric performance of PBDTT-BTQ in the photodetector

To evaluate a PBDTT-BTQ as the SWIR sensitizer, the SWIR photodetectors are first fabricated with a PBDTT-BTQ:$PC_{60}BM$ bulk heterojunction film as the photoactive layer. PBDTT-BTQ SWIR photodetectors are fabricated with both regular (EBL/photoactive layer/HBL) and inverted (HBL/photoactive layer/EBL) structures. A 5 nm-thick layer of molybdenum trioxide (MoO_3) was thermally evaporated onto the cleaned ITO substrates. A 10mg/ml solution of Poly-TPD (American Dye Source) in dichlorobenzene was spin-coated at 4000 rpm for 60 seconds and annealed at 110°C for 30 minutes. The PBDTT-BTQ:$PC_{60}BM$ precursor solution was then spin-coated at 1000 rpm for 60 seconds and annealed a 110°C for 10 minutes. The device was finished by thermally evaporating BCP (10 nm), LiF(1 nm), and Al(100 nm) sequentially. For the inverted photodetectors, the ZnO precursor was spin-coated at 4000 rpm for 60s and then annealed at

350°C for 20 minutes in the ambient. The substrate was subsequently introduced into a nitrogen glove box. The PBDTT-BTQ:$PC_{60}BM$ precursor solution was then spin-coated at 1000 rpm for 60 seconds and annealed a 110°C for 10 minutes. The device fabrication was completed by sequential thermal evaporation of m-MTDATA (10 nm), MoO_x (5 nm), and Al (100nm). All devices were encapsulated with a cavity glass and UV-curable epoxy. The regular device structure is ITO/MoO_3 (5 nm)/Poly(4-butylphenyl-diphenyl-amine (Poly-TPD) (40 nm)/PBDTT-BTQ:$PC_{60}BM$ (200 nm)/2,9-Dimethyl -4,7-diphenyl-1,10-phenanthroline (BCP) (10 nm)/LiF(1 nm)/Al (100 nm). Poly-TPD and BCP are used as an EBL and an HBL, respectively. The inverted device structure is ITO/ZnO/PBDTT-BTQ:$PC_{60}BM$ (100nm)/ 4,4',4"-Tris[(3-methylphenyl)phenylamino]triphenylamine (m-MTDATA) (10 nm)/MoO_3 (5 nm)/Al (100 nm). ZnO and m-MTDATA are used as an HBL and an EBL, respectively. Both regular and inverted devices employ both an EBL and an HBL to decrease the dark current and the schematic energy band diagrams of both regular and inverted devices are shown in Figure 34 (a) and (b).

The current-voltage (J-V) characteristics of the PBDTT-BTQ photodetectors under dark and SWIR illumination (876μW/cm^2 at 1000nm) are shown in Figure 35 (a) and (b). Both photodetectors exhibit typical rectifying characteristics of a diode with rectification ratios of 1.4×10^4 (± 1 V) and 0.9×10^3 (± 1 V) in regular and inverted devices, respectively. The dark currents are 3.5×10^{-5} mA/cm^2 and 8.8×10^{-6} mA/cm^2 for the regular and inverted devices at −1 V, respectively. The photodetectors with both hole and electron blockers show significantly low dark currents even in the low-bandgap nature of the PBDTT-BTQ polymer with a very narrow bandgap of 1.0 eV, which is relatively very narrow compared to typical polymer donor materials used as the visible absorber.[80] Photodetectors with an inverted structure show a lower dark current compared to that with a regular structure. It indicates that the ZnO/m-MTDATA combination is better charge blocking layers compared to the BCP/Poly-TPD combination because ZnO and m-

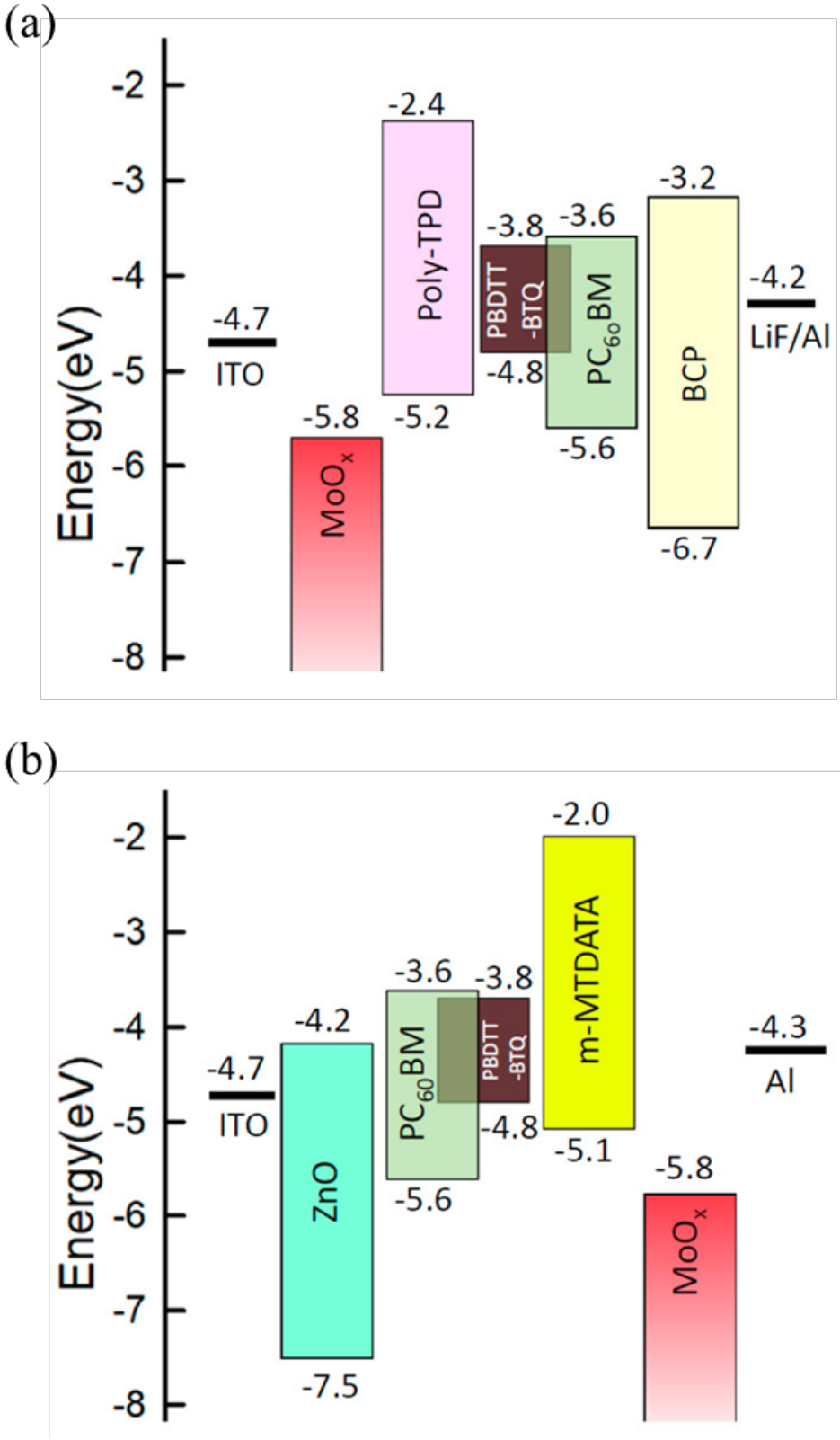

Figure 33 Energy band diagram of (a) the regular photodetector and (b) the inverted photodetector.

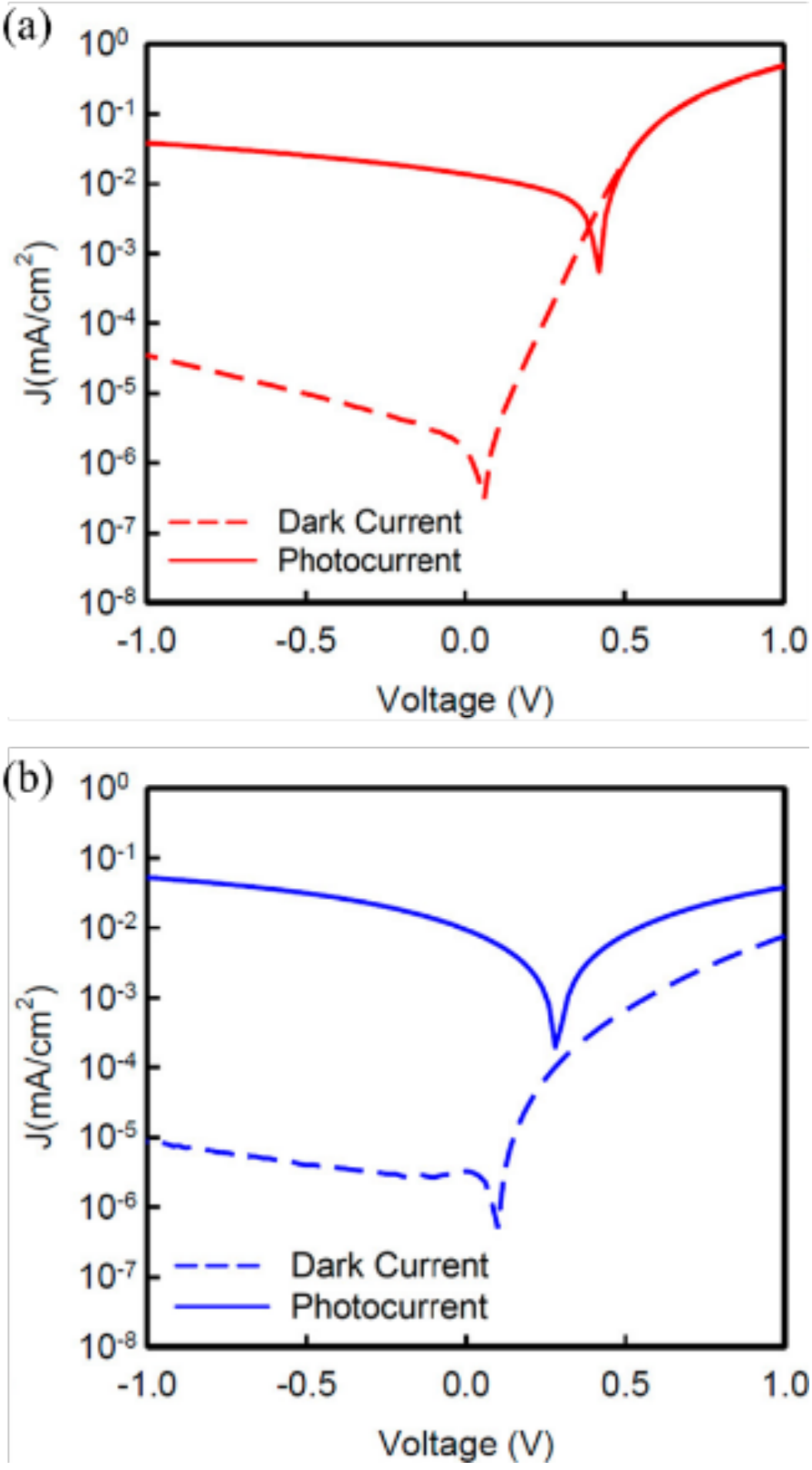

Figure 34 J−V characteristics of (a) the regular device and (a) the inverted device.

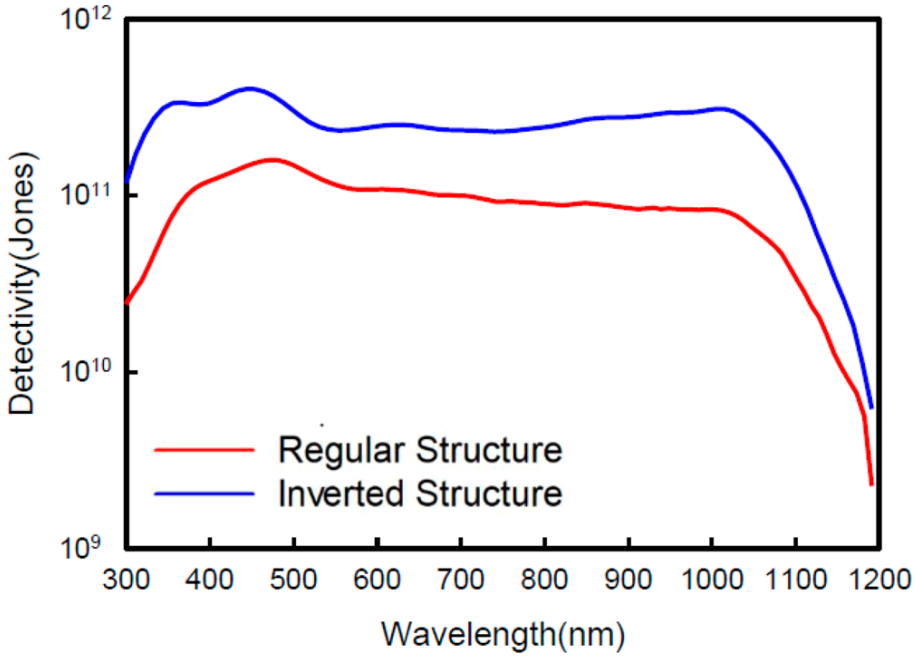

Figure 35 Spectral detectivity of regular and inverted photodetectors under an applied bias of -1 V.

MTDATA create higher barriers for hole and electron injection from electrodes, respectively, as shown in Figure 34.

Spectral detectivities of the photodetectors under -1V are shown in Figure 36, which are similar to the absorption spectrum of the pristine PBDTT-BTQ film, showing a peak wavelength of 1000 nm. The detectivity values of the regular photodetector are over 1×10^{10} Jones at SWIR wavelengths from 800nm to 1150nm, and the maximum detectivity value is 8.4×10^{10} Jones at the wavelength of 1000 nm. Due to the lower dark current in the inverted device compared to the regular device, the inverted device exhibits higher detectivity than regular photodetector. The detectivity values of the inverted photodetector are over 1.0×10^{11} Jones at SWIR wavelengths from 800nm to 1100nm, and the maximum detectivity value is 3.0×10^{11} Jones at the wavelength of 1000 nm.

To further understand the relationship between the detectivity and the dark current, the photodetectors are fabricated with various active layer thicknesses (70, 100, 135, and 200 nm) by

controlling the PBDTT-BTQ:$PC_{60}BM$ precursor solution concentration (15, 20, 25, and 30 mg/mL). *J*–*V* characteristics of the photodetectors with various active layer thicknesses are shown in Figure 37. Figure 38 (a) shows the dependence of the active layer thickness on the photocurrent and dark current under reverse bias (−1 V). In both regular and inverted devices, the dark currents decrease significantly with increasing the active layer thickness. The dark current in the regular device decreases by 2 orders of magnitude as the active layer thickness increases from 70 to 200 nm, resulting in a low dark current density of 3.5×10^{-5} mA/cm^2. For the inverted device, the dark current decreases by 2 orders of magnitude from 1.0×10^{-3} to 8.8×10^{-6} mA/cm^2 with increasing the active layer thickness from 70 to 100 nm. It should be noted that there is no significant change in photocurrent as the active layer thickness increases from 70 to 200 nm. While increasing the active layer thickness is expected to decrease the photocurrent due to the increase of the bulk resistance in the device, conversely, the light absorption is expected to be enhanced due to the thick photoactive layer. The resulting photocurrent shows no significant change with various active layer thicknesses. Due to the significant reduction of dark current with increased active layer thickness, the detectivity enhances from 2.1×10^{10} to 3.1×10^{11} Jones under −1 V at the peak wavelength of 1000 nm as shown in Figure 38 (b).

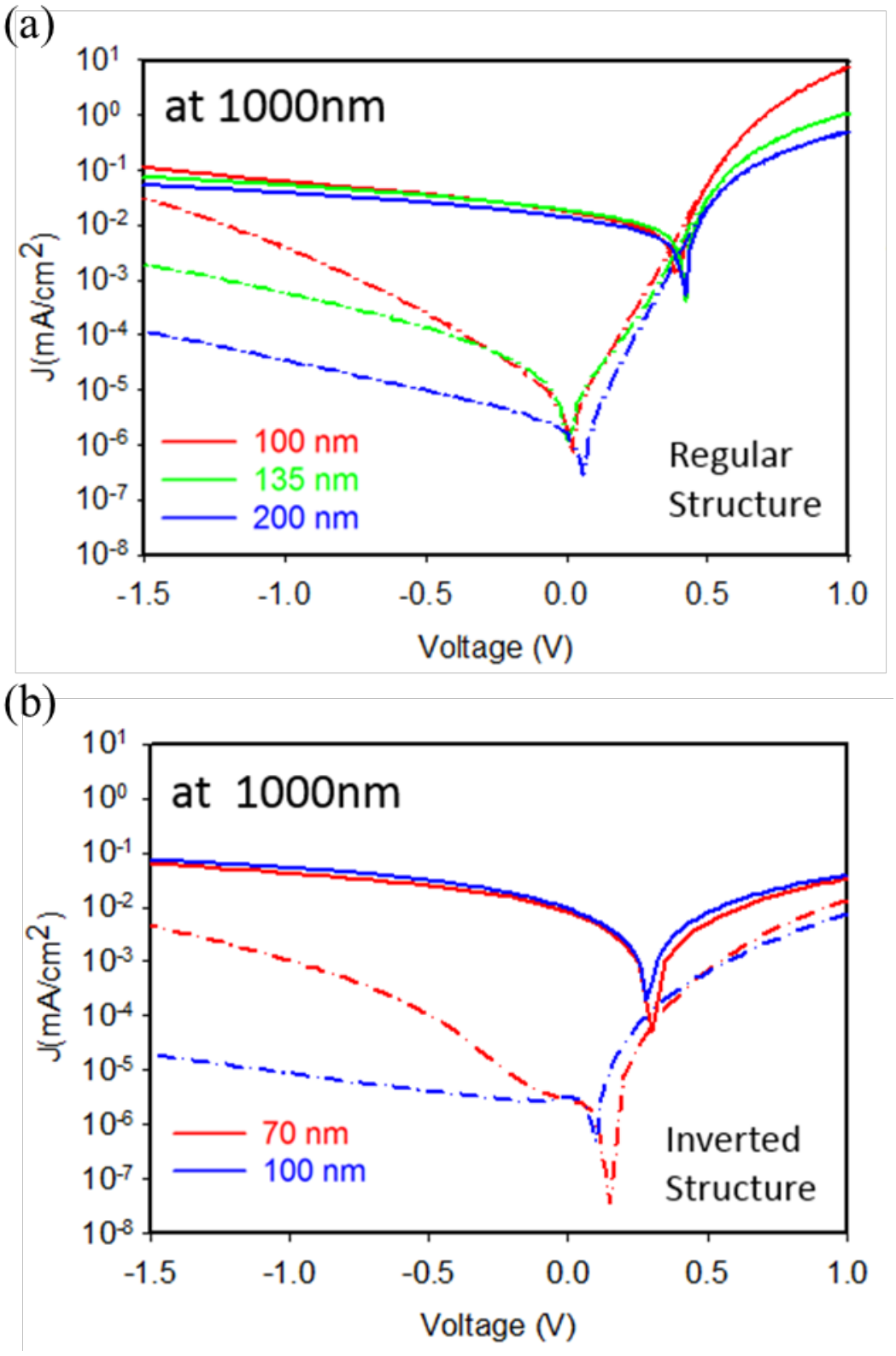

Figure 36 Dark and photo J-V characteristics of (a) the regular and (b) inverted photodetectors with different active layer thicknesses.

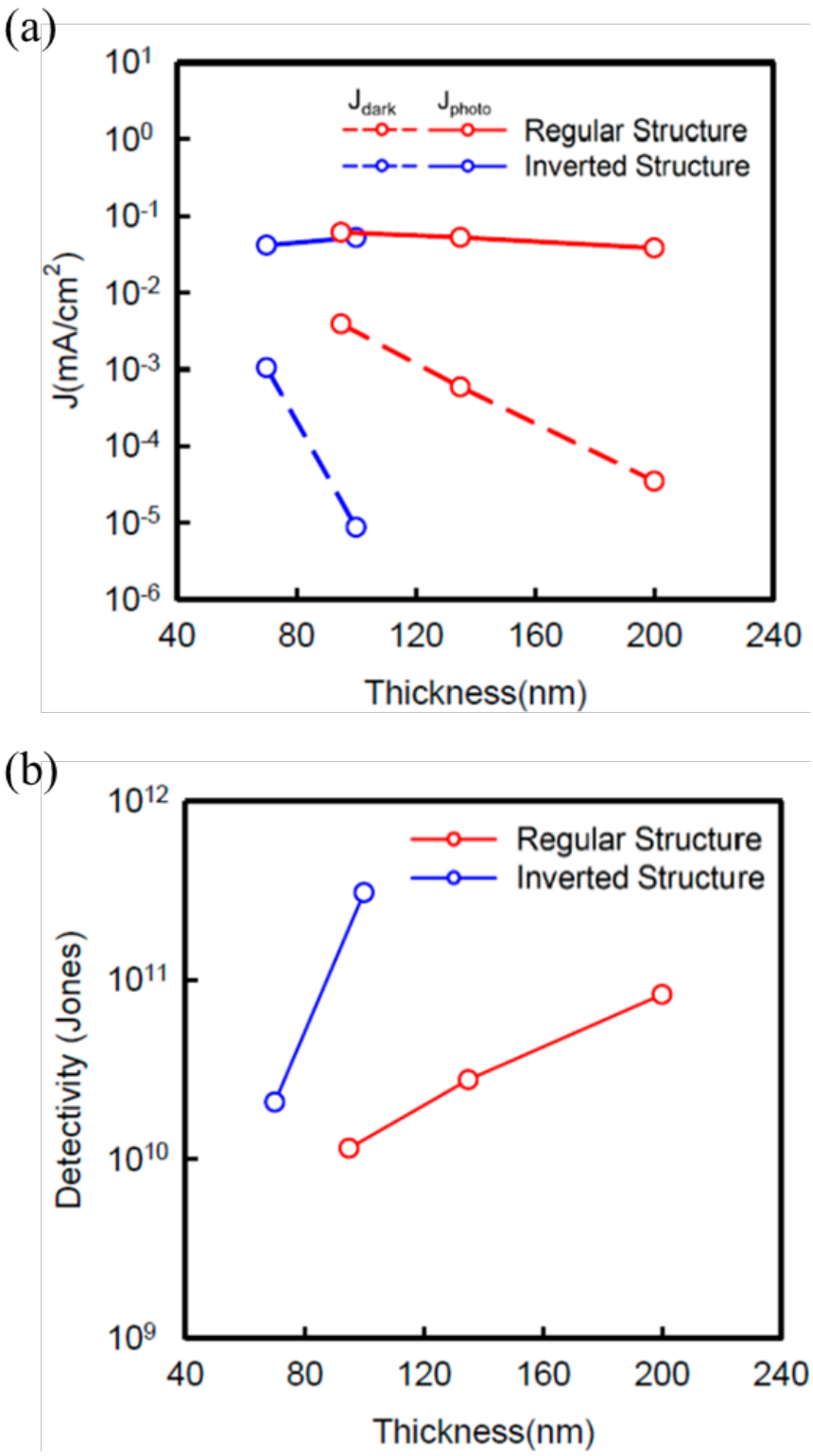

Figure 37 (a) Dependence of the photocurrent and dark current on the active layer thickness for regular and inverted devices. (b) Dependence of detectivity on the active layer thickness for regular and inverted photodetectors. The photocurrent was measured by irradiating the device with 1000 nm monochromatic light.

3.2. Investigation on the origin of low EQE

The PBDTT-BTQ photodetectors show very low external quantum efficiencies (EQEs) of below 10 % in the wavelengths from 300 nm to 1,200 nm as shown in Figure 39. While the EQEs at the wavelengths below 500 nm are ~5 % and slightly higher than that at near-IR wavelengths, the EQEs at the near-IR wavelengths beyond 600 nm is extremely low (below 2%) even under the reverse bias of -1 V.

The possible reason for these low EQE is unfavorable energy band alignment between the PBDTT-BTQ donor and the $PC_{60}BM$ acceptor. It is incredibly challenging to fabricate SWIR photodetectors by using the low-bandgap organic semiconductors because of the nature of the excitonic material with strong binding energy. As excitonic materials, organic semiconductors generate excitons, which is strongly bounded electron-hole pairs, by absorbing photons irradiated. The exciton dissociation is required to get photogenerated current but the photo-generated excitons in organic semiconductors need external forces to be dissociated to electron and hole carriers. In typical organic photovoltaic and detecting devices, therefore, the donor/acceptor system, which is a mixing of two organic semiconductors: an electron donor and an electron acceptor, is used for the exciton dissociation because excitons are easily dissociated at the material interfaces with different HOMO and LUMO levels. The combination of donors and acceptors with an appropriate energy alignment is vital for efficient exciton dissociation in organic SWIR sensitizer. Therefore, the excitonic material, PBDTT-BTQ as a donor, needs to have an acceptor with a proper energy band alignment to efficiently dissociate photo-generated excitons. In the ideal case, the LUMO level of a donor needs to be shallower than that of an acceptor for efficient exciton dissociation, but the LUMO of PBDTT-BTQ (3.8 eV) is deeper than that of $PC_{60}BM$ (3.6 eV) thus resulting in poor exciton dissociation. Therefore, there is still room to further enhance the EQE and, eventually, the detectivity in the PBDTT-BTQ-based near-IR photodetector if applying appropriate acceptors with proper energy band alignments.

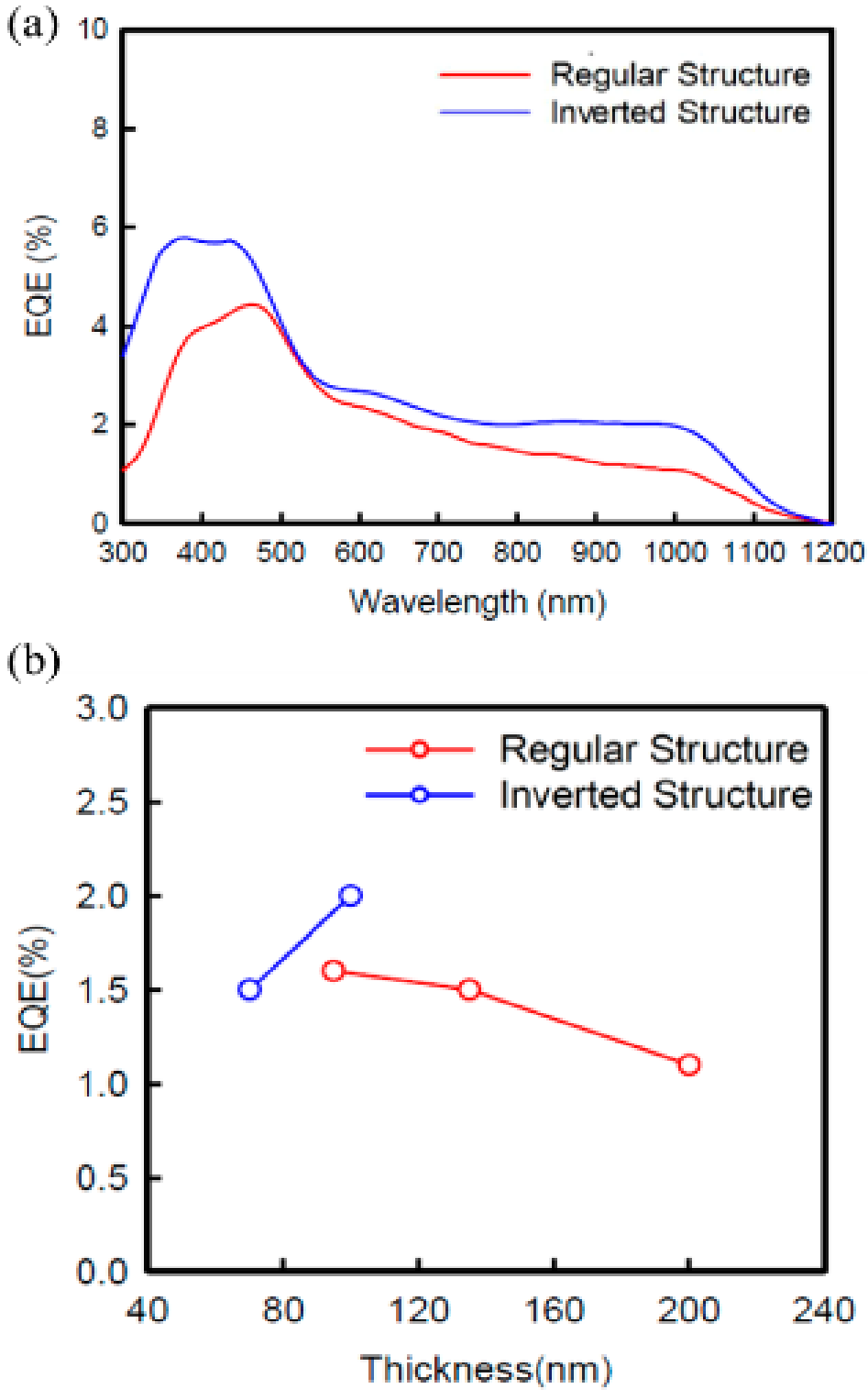

Figure 38 (a) EQE spectra of regular and inverted photodetectors. (b) Dependence of EQE on the active layer thickness under a monochromatic IR light of 1000 nm.

4. SWIR Photodetector using $SnNcCl_2$ as a SWIR sensitizer

4.1. Evaluation of the photoelectric performance of $SnNcCl_2$ in the photodetector

To find appropriate acceptor materials for $SnNcCl_2$ SWIR sensitizer, photodetectors with different acceptor materials are fabricated with inverted (HBL/photoactive layer/EBL) structures. The inverted device structure is ITO / ZnO / Acceptor / $SnNcCl_2$ (30nm) / 4,4',4"-Tris[(3-methylphenyl)phenylamino]triphenylamine (m-MTDATA) (10 nm) / MoO_3 (5 nm) / Al (100 nm). Two acceptors (C_{60} and PCBM) were compared to see the effect of the band offset between the HOMO of the donor and the LUMO of the acceptor. ZnO and m-MTDATA are used as an HBL and an EBL, respectively. The photodetector devices employ both an EBL and an HBL to decrease the dark current and the schematic energy band diagrams of the $SnNcCl_2$ photodetector is shown in Figure 40 (a) and (b).

The current-voltage (J-V) characteristics of the $SnNcCl_2$ photodetectors under dark and near-IR illumination (876μW/cm^2 at 1000nm) are shown in Figure 41. In the C_{60} device, a small energy band offset between the LUMO of C_{60} and the HOMO of $SnNcCl_2$ makes the charge generation effect, resulting in the increased dark currents as shown in Figure 41. Contrastively, in the device using PCBM as an acceptor, the dark current decreased significantly, roughly 10^2 order, which can affect enormously to the performance of the IR-to-Visible up-conversion devices.

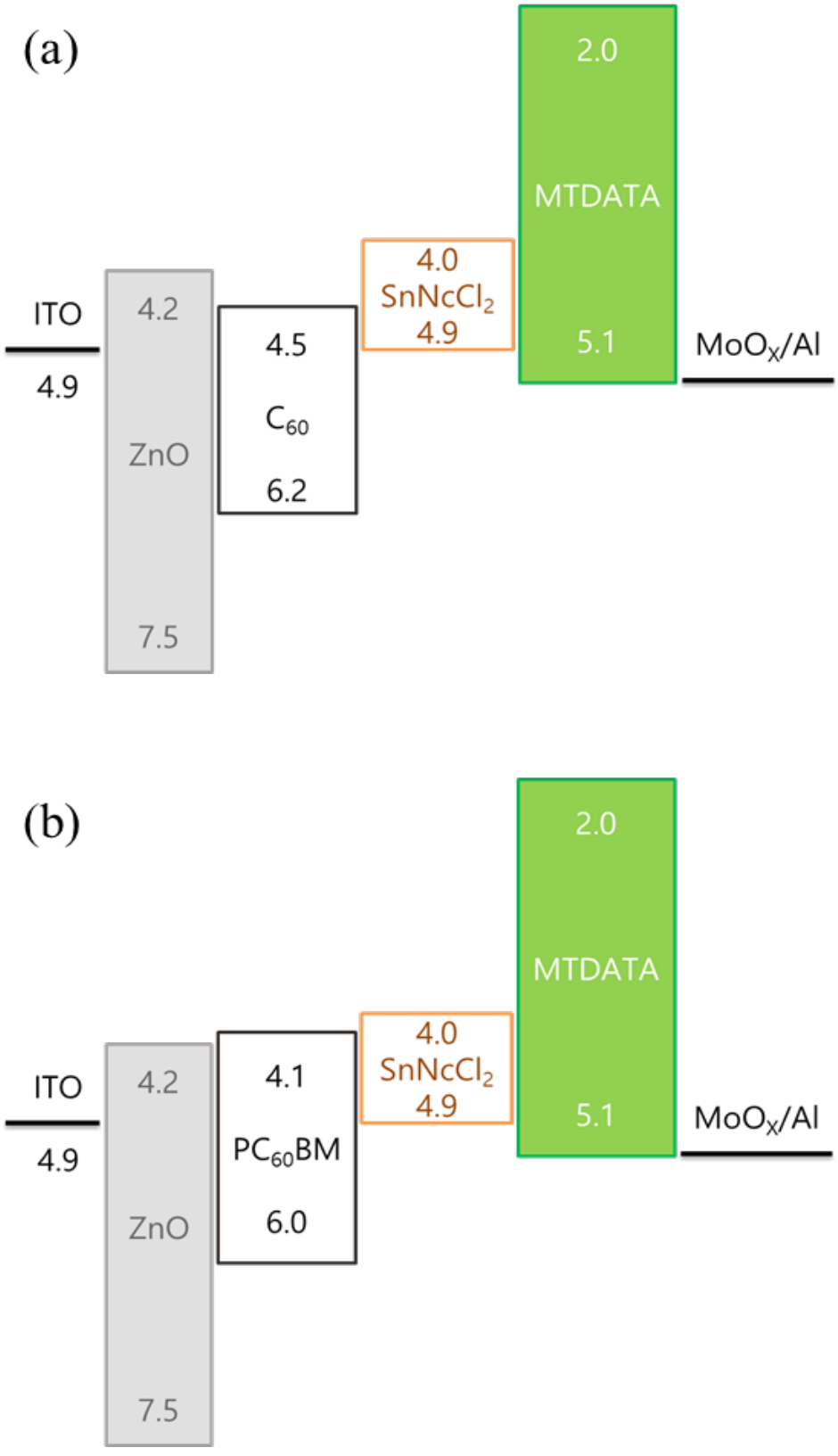

Figure 39 Energy band diagram of inverted photodetectors with bilayer structure using (a) C_{60} acceptor, and (b)PCBM acceptor.

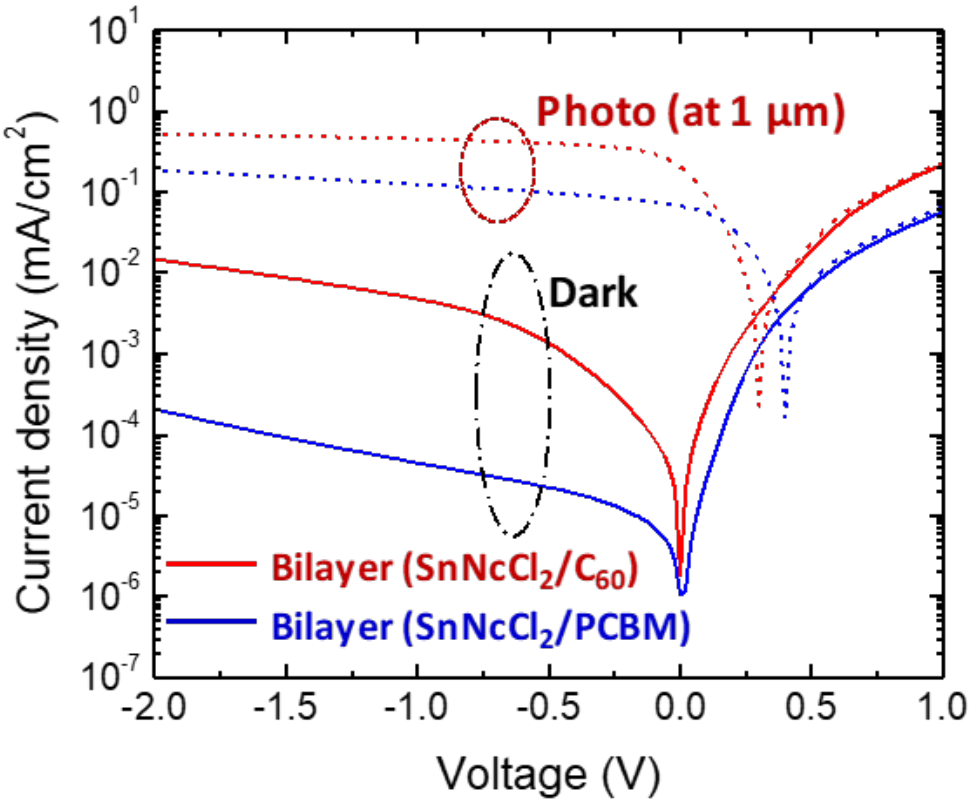

Figure 40 Current-Voltage characteristic of the $SnNcCl_2$ photodetectors

Spectral detectivities of the photodetectors under -0.1V are shown in Figure 42. The device shows a multispectral response with photosensitivity from 300 to 1,200 nm. The detectivity spectra are like the absorption spectrum of the pristine $SnNcCl_2$ film, showing a peak wavelength of 880 nm. The detectivity values of the inverted photodetector are over 1×10^{11} Jones at near-IR wavelengths from 700nm to 1050nm, and the maximum detectivity value is 5×10^{10} Jones at the wavelength of 880 nm.

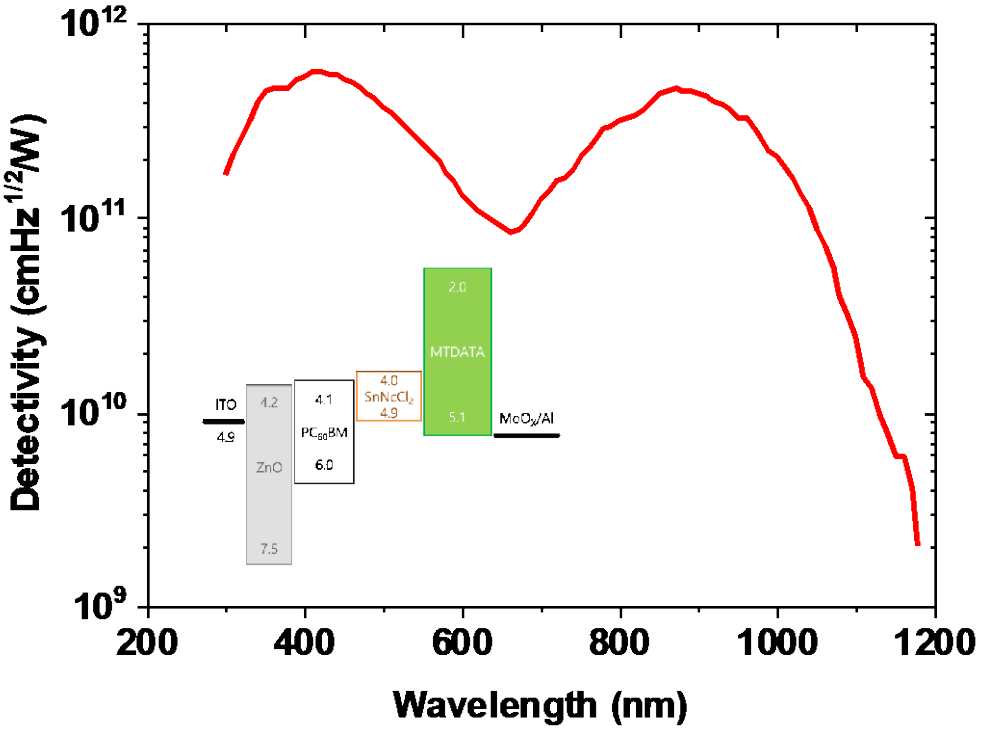

Figure 41 The spectral detectivity of the $SnNcCl_2$ photodetector. (inlet: the structure of the photodetector)

4.2. Effect of $SnNcCl_2$ SWIR Sensitizer Thickness on the Photodetector Performances

The $SnNcCl_2$ layer is the most important layer for the photodetector which absorbs the targeted SWIR wavelength of the light and generates photoelectric effect inside the molecule. To verify the effect of the thickness of $SnNcCl_2$, photodetectors with the various thicknesses (20, 40, 50nm) were fabricated. *J*−*V* characteristics of the photodetectors with various active layer thicknesses are shown in Figure 43. Figure 44 shows the dark current and detectivity values changing with the thickness of the sensitizing material at the bias of -1V. With increasing the thickness from 20nm to 50nm, the IR photocurrent was increasing from 4.32×10^{-3} mA/cm^2 to 8.33×10^{-3} mA/cm^2, and the dark current was decreasing from 5.71×10^{-3} mA/cm^2 to 3.15×10^{-3} mA/cm^2. The reason for the increase of the IR current is that the absorbance is directly proportional to the

thickness of the materials. Due to the increased amount of the absorbed light, the photogeneration in the sensitizing layer also can be enhanced, resulting in high IR photocurrent in the photodetector. For the reduction of dark current, the bulk resistance which is increased with the thickness of the material reduces the current passing through the photodetector. As the outcome of the increase of the photocurrent and the reduction of the dark current, the detectivity of the photodetectors was enhanced with increased thickness, from 2.54×10^{11} Jones to 6.67×10^{11} Jones, as shown in Figure 44 (b). Figure 43 shows the J-V characteristics of the photodetectors with different $SnNcCl_2$ thickness. The photocurrent plots (dashed lines) are increased with the thickness of the SnNcCl2, and the dark current plots (solid lines) are decreased for the thicker layer. Figure 45 also clearly shows the increase of the photoelectric response in the $SnNcCl_2$ absorption range in the IR region. The external quantum efficiency at the peak wavelength of absorption, 880nm, is increased from 1.26 % to 1.71%, under the bias of -0.5V.

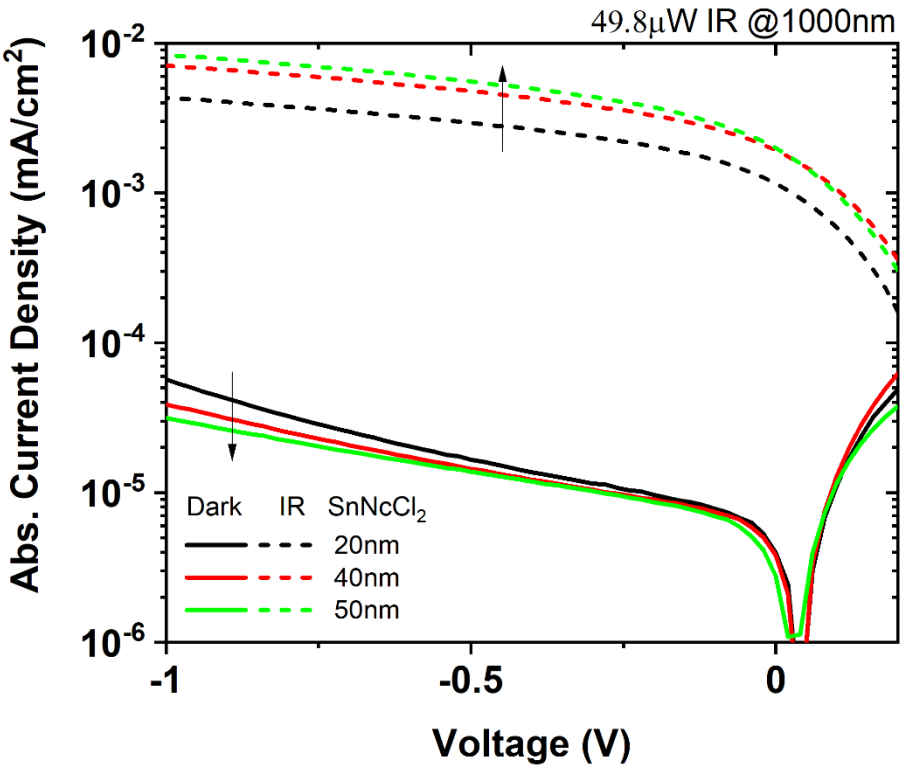

Figure 42 Dark and photo J-V characteristics of $SnNcCl_2$ photodetectors with different $SnNcCl_2$ layer thicknesses.

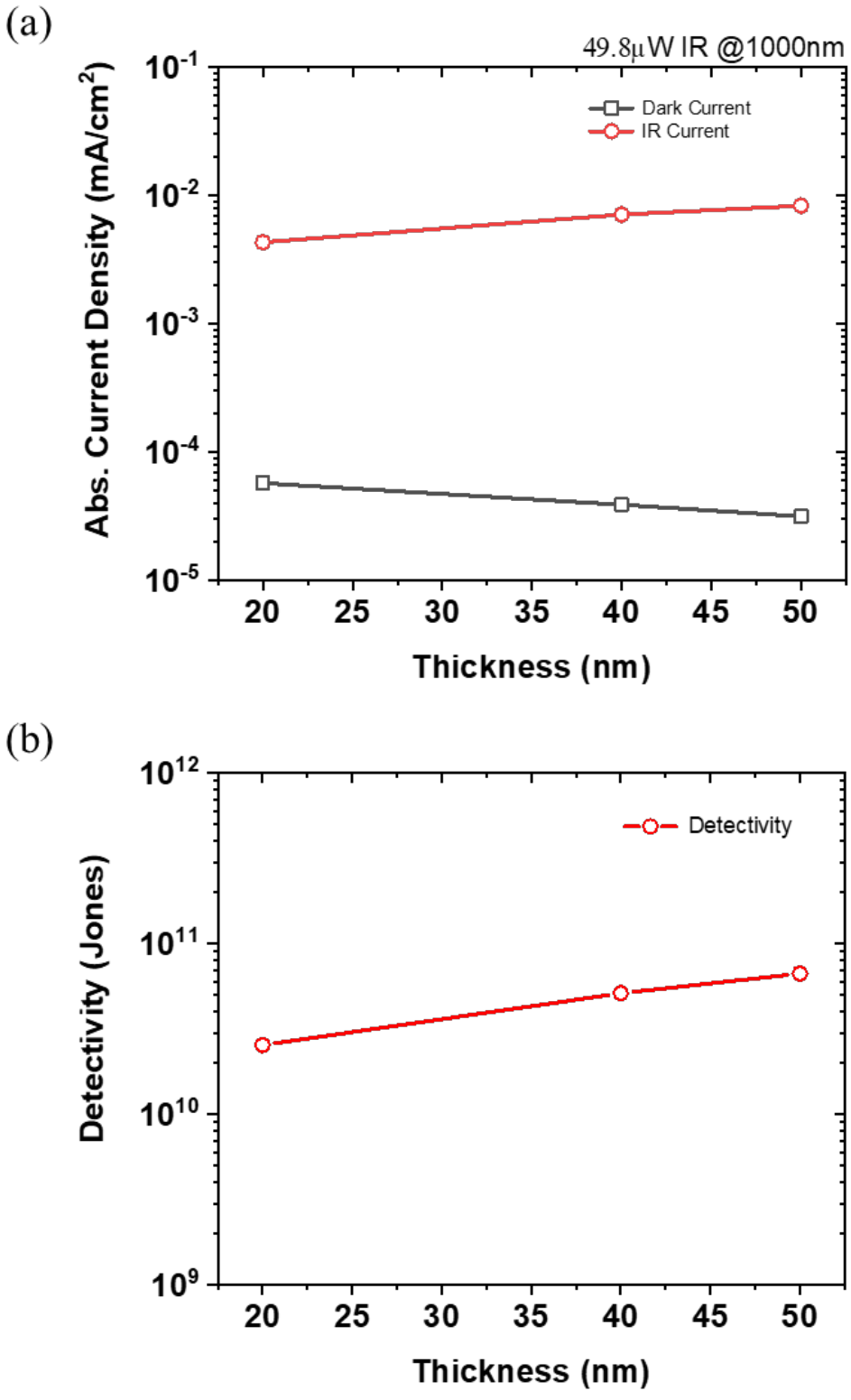

Figure 43 (a) Dependence of the photocurrent and dark current on the active layer thickness, and (b) Dependence of detectivity on the active layer thickness. The photocurrent was measured by irradiating the device with 1000 nm monochromatic light.

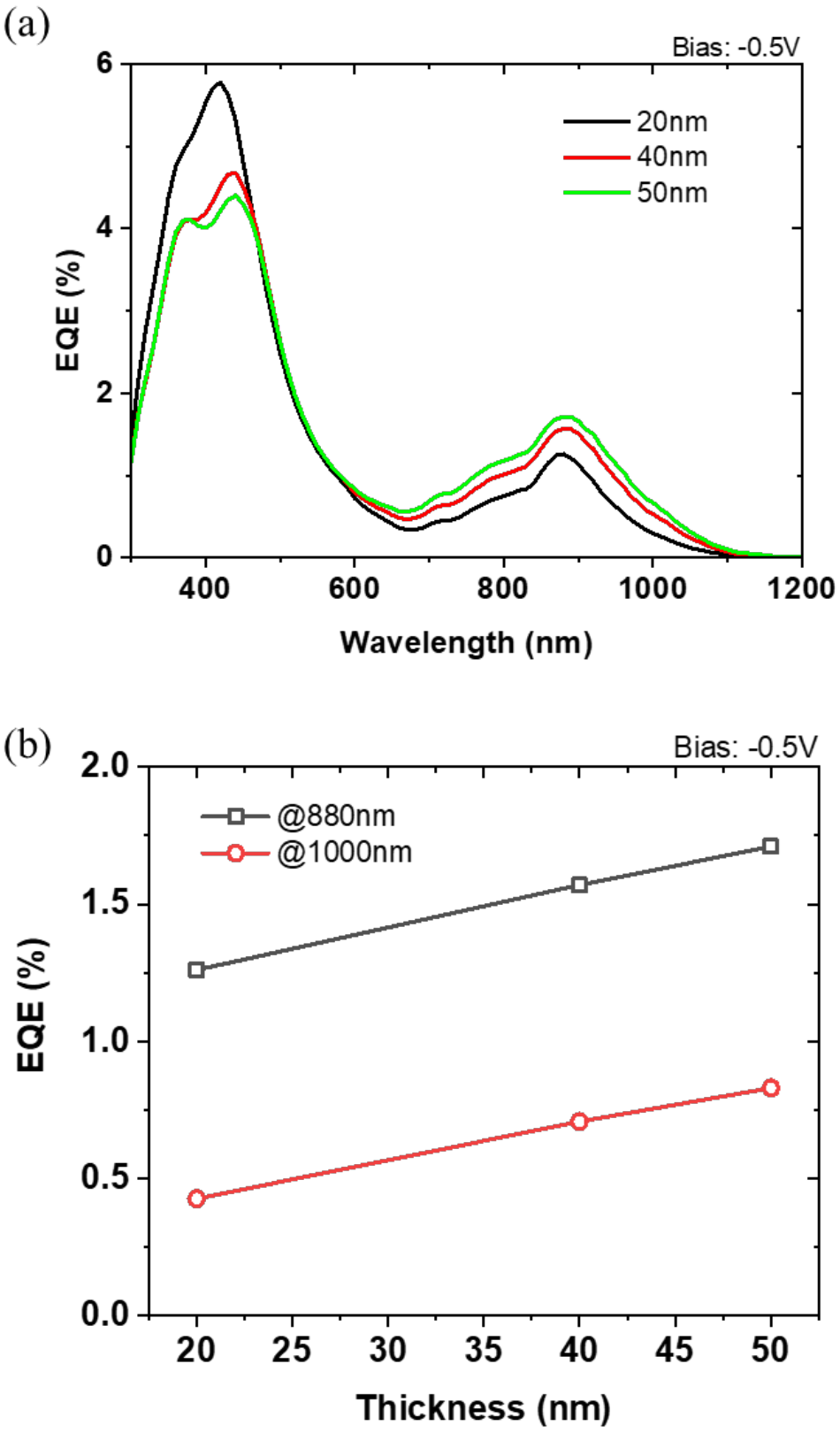

Figure 44 (a) EQE spectra of $SnNcCl_2$ photodetectors. (b) Dependence of EQE on the active layer thickness at the IR light wavelength of 880nm and 1000 nm.

CHAPTER VII

SWIR-TO-VISIBLE UP-CONVERSION OLEDs

1. Introduction

Infrared-to-visible up-conversion OLEDs have great potential because they are based on widely used OLED technology, which has advantages in low-cost and large-area manufacturing. Especially in the SWIR detection field, OLED-based up-conversion devices have a great possibility on a competitive price, because conventional SWIR imaging is based on extremely expensive InGaAs inorganic semiconductors. The SWIR-to-visible up-conversion OLEDs consist of two parts; a photodiode part which detects targeted wavelength range of the light, and an OLED part which emit visible light. The OLED field has been studied enormously and already commercialized for popular consumer electronics, but research on organic photoelectric devices including organic solar cells and photodetectors, especially on the infrared range, has not been performed as much as in OLEDs. Due to the limitation of infrared sensitizer, in the latest SWIR-to-visible up-conversion OLED employed inorganic colloidal PbSe quantum dots (QDs) as a sensitizer to have infrared sensitivity beyond the infrared wavelength of 1μm. But the inorganic QD cannot make low-cost because their synthesis method, hot-injection synthesis, is not easy to

scale for low-cost and mass production. Additionally, the QD contains toxic element Pb, is not suitable for consumer electronics. To realize low-cost SWIR-to-visible up-conversion OLEDs, the QD SWIR sensitizer needs to be replaced with organic SWIR sensitizing materials. In this chapter, SWIR-to-visible up-conversion OLEDs using a polymer and a small molecule SWIR organic sensitizer are demonstrated.

2. All-Organic SWIR-to-Visible up-conversion OLEDs with a low-bandgap polymer SWIR sensitizer, PBDTT-BTQ

2.1. Demonstration of the PBDTT-BTQ SWIR-to-visible up-conversion OLED

Based on the photodetector work using PBDTT-BTQ as the SWIR absorber, IR sensitive OLEDs were fabricated, functioning as a SWIR-to-visible up-conversion device, with a SWIR sensitivity up to 1200nm using a PBDTT-BTQ as the polymer SWIR sensitizer. For the IR sensitive OLEDs, the ZnO precursor was spin-coated at 4000 rpm for 60s and then annealed at 350°C for 20 minutes in the ambient. The substrate was subsequently introduced into a nitrogen glove box. The PBDTT-BTQ:$PC_{60}BM$ precursor solution was then spin-coated at 1000 rpm for 60 seconds and

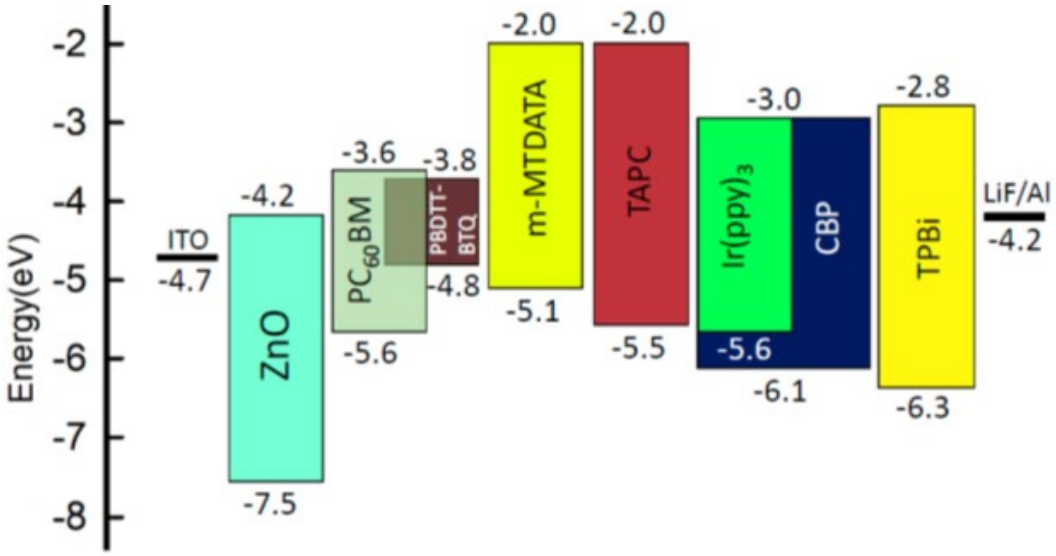

Figure 45 Energy band diagram for the IR sensitive OLED.

annealed a 110°C for 10 minutes. The substrate was transferred to the thermal evaporation chamber where m-MTDATA (15 nm), TAPC (30nm), 9% $Irppy_3$ doped CBP (20nm), TPBi (45 nm), LiF (1 nm) and Al (100 nm) were sequentially deposited. All devices were encapsulated with a cavity glass and UV-curable epoxy. A schematic energy band diagram of the IR sensitive OLED with the following structure: ITO/ZnO/PBDTT-BTQ: PCBM (200 nm)/m-MTDATA (15nm)/4,4'-Cylcohexylidenebis[N,N-bis(4methylphenyl)benzenamine (TAPC) (30nm)/4,4'-Bis(9-carbazolyl-1,1'-biphenyl,4,4-N,N'-Dicarbazole-1,1'-biphenyl (CBP):9% Tris[2-phenylpyridine]iridium(III) ($Ir(ppy)_3$)/2,2',2"-(1,3,5-Benzinetriyl)-tris(1-phenyl-1-H-benzimidazole) (TPBi) (45 nm)/LiF (1 nm)/Al (100 nm) is shown in Figure 46. In the IR sensitive OLED with a PBDTT-BTQ as the polymer IR sensitizing layer, to keep the device off under forward bias, a ZnO HBL is inserted between the ITO anode and the polymer IR sensitizer to block hole injection from the anode. Under IR irradiation, photo-generated holes in the PBDTT-BTQ:PC60BM IR sensitizing layer are injected through the m-MTDATA/TAPC double hole transport layers (HTLs) into the 9% $Ir(ppy)_3$ doped CBP green emitting layer of the OLED and recombine with electrons injected from the cathode to emit green visible light. The all-organic IR up-conversion OLED with a PBDTT-BTQ IR sensitizer successfully converted invisible near-IR light of 700−1100 nm directly to visible green light with a peak emission wavelength of 520 nm. Figure 46 is the energy band structure of the device.

Figure 47 (a) shows the luminance−current density−voltage (L−J−V) characteristics of the IR-to-visible up-conversion OLED under dark and SWIR illumination (876 $\mu W/cm^2$ at 1000 nm). In the dark without IR illumination, light emission from the IR-to-visible up-conversion OLED was not observed until the applied voltage reached 10.5 V as shown in Figure 47 (a). With SWIR irradiation (876 $\mu W/cm^2$ at 1000 nm), the device turned on at 3.5 V along with an onset of green light emission, and thus, the light emission modulation by IR light is clearly demonstrated. Figure 47 (b) shows the spectral IR-to-visible photon-to-photon conversion efficiency under 9.5 V. The

photon-to-photon conversion efficiency spectrum is similar to the detectivity and the EQE spectra of PBDTT-BTQ-based photodetector as shown in Figure 36 and Figure 39, respectively. The all-organic IR-to-visible up-conversion OLED shows IR sensitivity up to 1100 nm, and the photon-

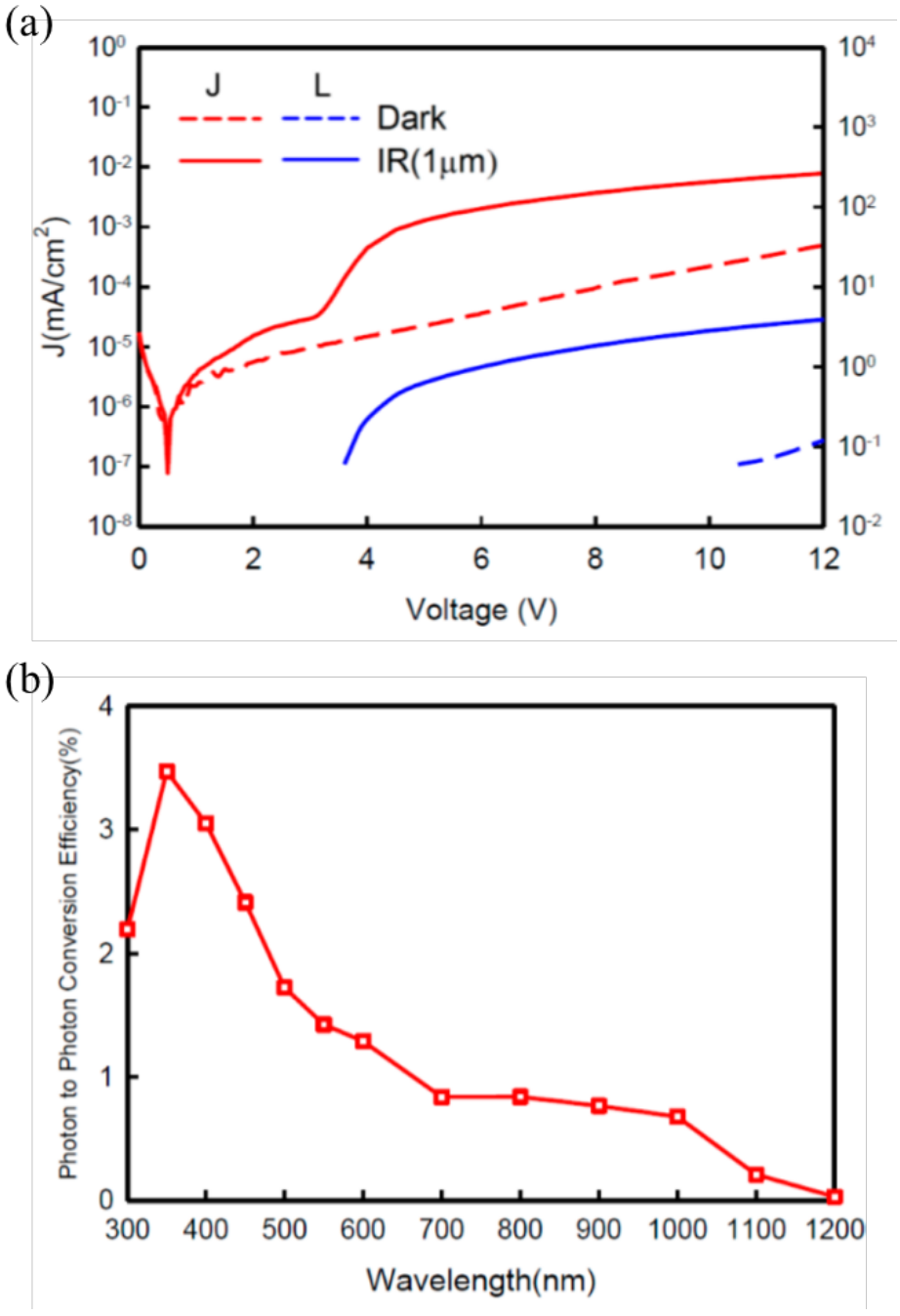

Figure 46 (a) J−V−L characteristics of the IR sensitive OLED, and (b) Spectral IR-to-visible photon-to-photon conversion efficiency of the IR sensitive OLED.

to-photon conversion efficiencies at the near-IR wavelengths from 700 to 1000 nm are ~0.8%. The possible reason for the low photon-to-photon conversion efficiency is a poor exciton dissociation due to unfavorable energy band alignment between the PBDTT-BTQ donor and the $PC_{60}BM$ acceptor, which is the same reason in the PBDTT-BTQ-based photodetectors as shown in Figure 39. Figure 48 shows the images of the IR-to-visible up-conversion OLED at 10 V with and without near-IR illumination. The switching effect of green light-emitting by near-IR light irradiation was clearly shown. This is the very first report of an all-organic IR-to-visible up-conversion OLED with near-IR sensitivity up to 1100 nm using a polymer near-IR sensitizer.

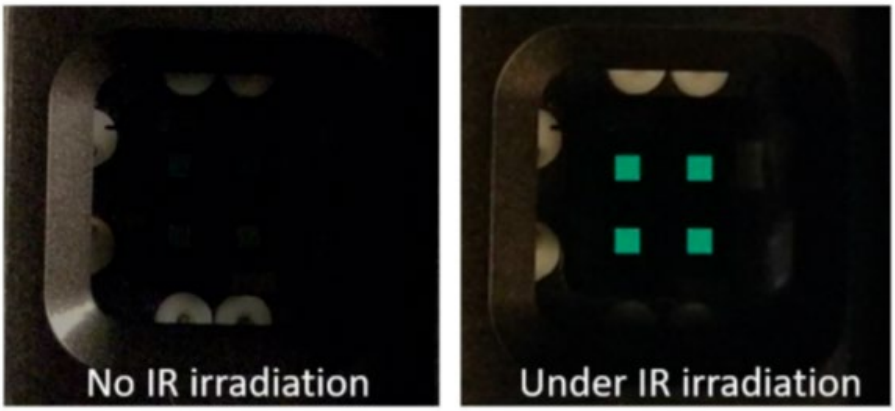

Figure 47 Image of the IR sensitive OLED under no IR and IR irradiation when the applied bias is 10 V.

2.2. Thickness Effect of the PBDTT-BTQ:PCBM SWIR Sensitizing Layer of Up-conversion OLEDs

Thickness variation of SWIR sensitizing layer by changing the concentration of the precursor solution was performed. In the photodetector, a thicker active layer offers lower dark current and higher photocurrent, which increased the performance of the photodetector. In the up-conversion

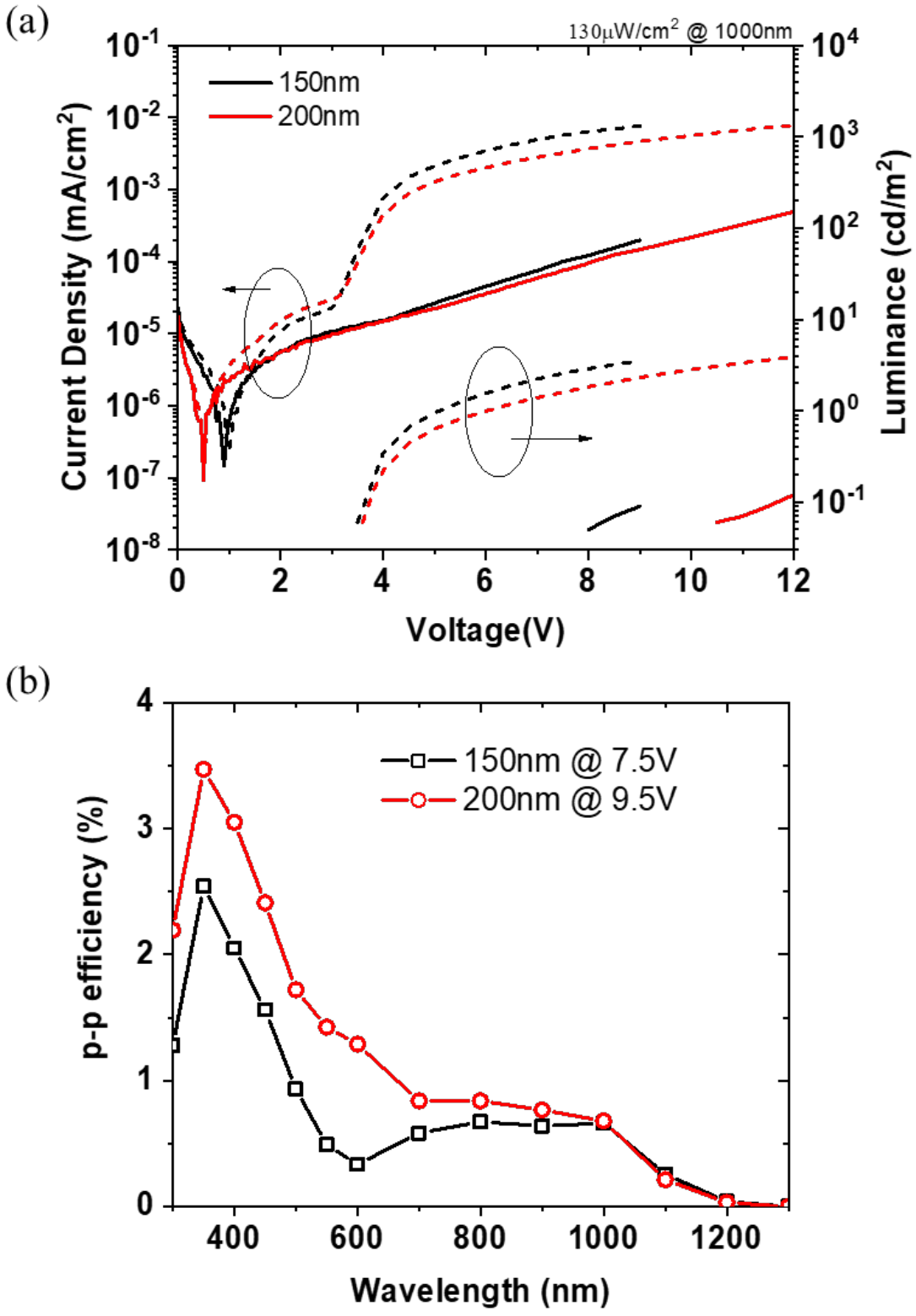

Figure 48 (a) J−V−L characteristics and (b) Spectral IR-to-visible photon-to-photon conversion efficiency of the IR sensitive OLED with various sensitizing layer thickness

OLEDs, a thicker active layer made both the photocurrent and the dark current as shown in Figure 49 (a). The thick active layer increased the bulk resistance which reduced the current through the device for both conditions. As result, the luminance is decreased, but the dark turn-on voltage is increased by 2.5V, which enlarges the operation voltage window. Figure 49 (b) shows spectral photon-to-photon efficiency, which shows that there is no significant difference in IR range up to 1.2 μm, while the response in visible and near IR raised.

3. All-organic SWIR-to-visible up-conversion OLEDs with a low-bandgap small molecule, $SnNcCl_2$

3.1. Demonstration of the $SnNcCl_2$ SWIR-to-visible up-conversion OLED

The photoelectric property of $SnNcCl_2$ to sensitize SWIR was proven in photodetectors in the previous section. In the photodetectors' results, PCBM/$SnNcCl_2$ SWIR absorption layer can successfully generate electric current under SWIR irradiation with the low dark current level. ZnO will be used as hole blockers for the up-conversion device. Because the PCBM layer is solution-processed, the solution-processed hole blocker ZnO is required for device fabrication.

Figure 50 shows the schematic energy band diagram of the SWIR-to-green up-conversion OLED. The device structure is following: ITO/ZnO/ PCBM/$SnNcCl_2$/4,4'-Cylcohexylidenebis[N,N-bis(4methylphenyl)benzenamine (TAPC) (30nm)/4,4'-Bis(9-carbazolyl-1,1'-biphenyl,4,4-N,N'-Dicarbazole-1,1'-biphenyl (CBP):9% Tris[2-phenylpyridine]iridium(III) ($Ir(ppy)_3$)/2,2',2"-(1,3,5-Benzinetriyl)-tris(1-phenyl-1-H-benzimidazole) (TPBi) (45 nm)/LiF (1 nm)/Al (100 nm). For the

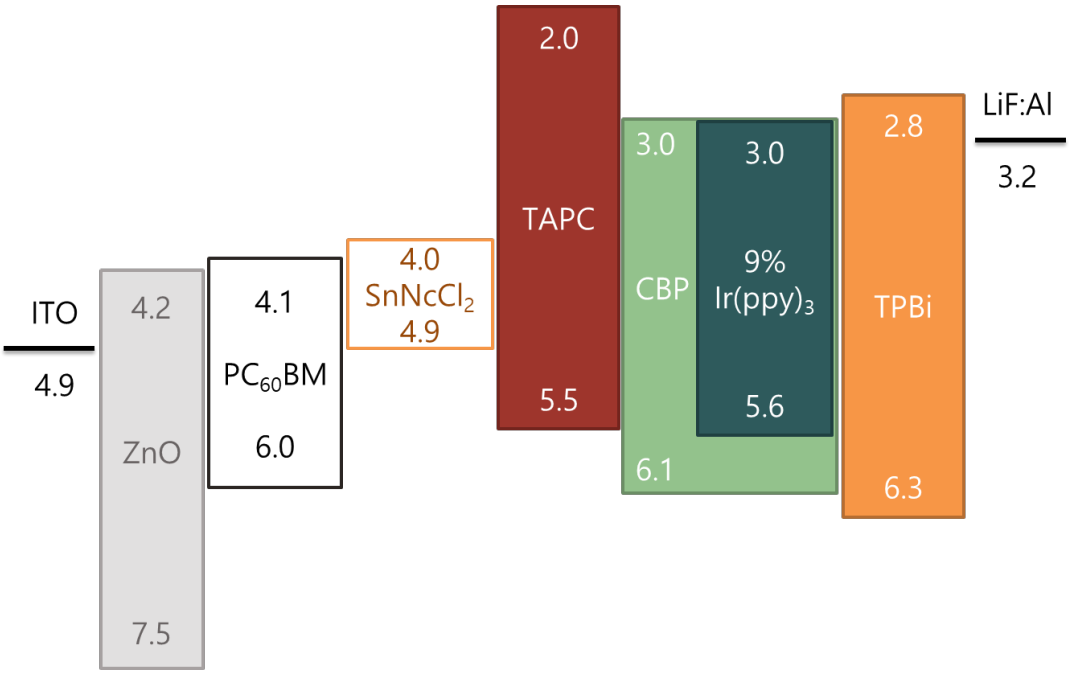

Figure 49 Schematic energy band diagram of the up-conversion OLEDs

device fabrication, first, the patterned ITO substrates were cleaned with acetone and isopropanol in an ultrasonic cleaner and subsequently rinsed with de-ionized water, blown dry with N_2 gas. For a solution-processed hole blocking layer, ZnO film was synthesized by a sol-gel process using precursors of zinc acetate and monoethanolamine (MEA) in ethanol solvent. For the acceptor in the IR sensitizer layer, PCBM was deposited by solution processing. All organic layers in the up-conversion OLEDs were thermally evaporated at a pressure of a few 10^{-7} torr. As the OLED part, TAPC, CBP:$Ir(ppy)_3$ and TPBi layers were used as a hole transporting layer, an emission layer, and an electron transporting layer, respectively. LiF/Al is a cathode electrode. All devices are encapsulated with a cavity glass and UV-cured resin. The active area of the final device is 0.04 cm^2.

Figure 51 (a) shows the J-V-L characteristics of the up-conversion OLED. For the IR irradiation, 1μm-wavelength SWIR from monochromator was used. In the J-V characteristics (red lines), it clearly shows photocurrent increases current density in the devices. The IR turn-on voltage was 5.0V, and the dark turn-on voltage was 10.0V, resulting in 5V of the operating voltage window.

The spectral photon-to-photon (P-P) efficiency of the devices is shown in Figure 51 (b). shows the sensitivity on infrared beyond 1μm wavelength, range up to 1.2μm. It shows the peak IR P-P efficiency as 1.21% at 880nm.

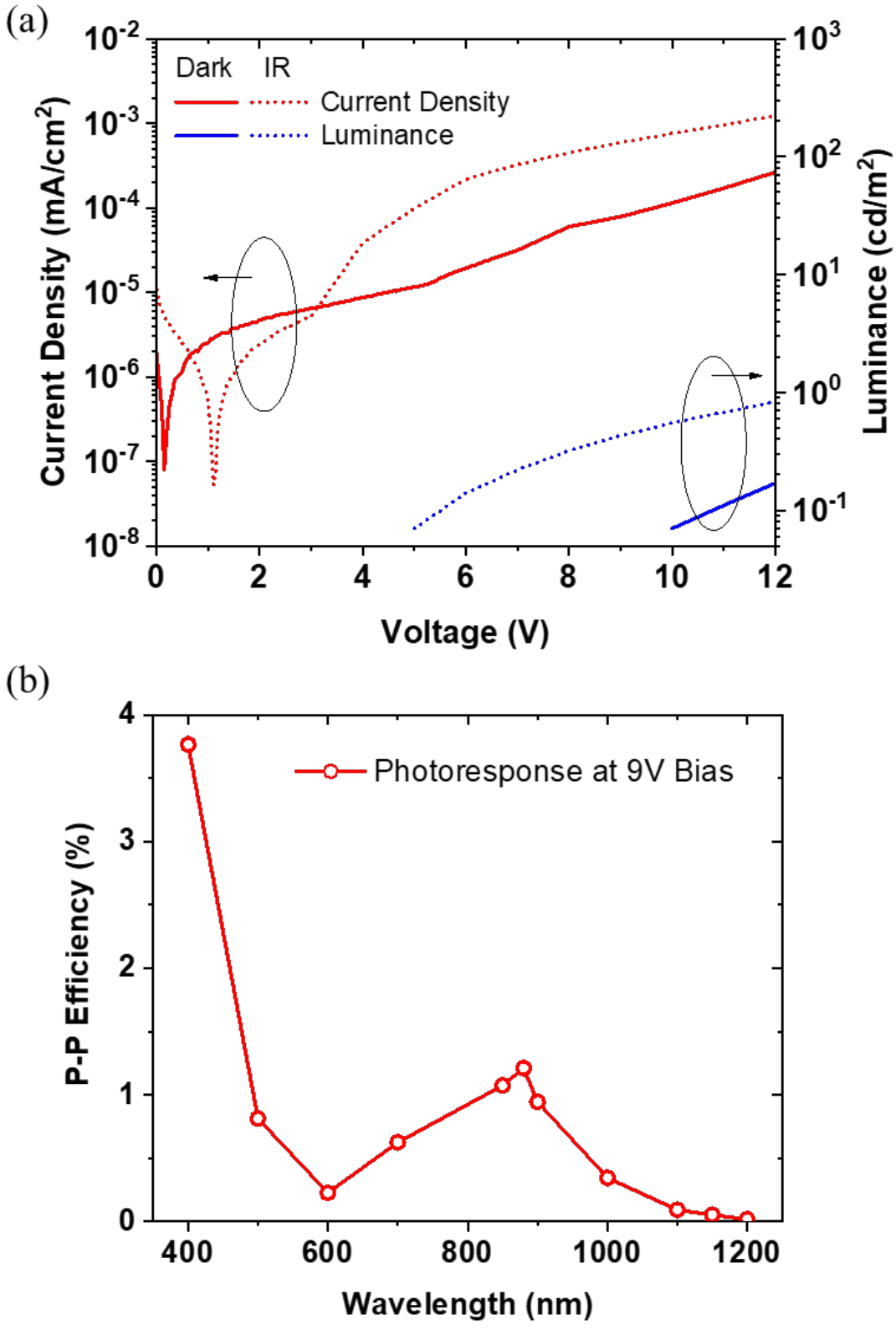

Figure 50 (a) Current-Voltage-Luminance (JVL) Characteristics comparison, (d) Spectral photo-response of the upconversion device with PCBM acceptor.

3.2. Acceptor Effect in the SWIR sensitizing layer of up-conversion OLEDs

In the previous photodetector comparison, the device with C_{60} acceptor shows high dark current as well as high photocurrent Figure 52 shows device structures to compare the acceptor materials, C_{60} and $PC_{60}BM$, for verifying the effect of these high currents in the SWIR-to-visible up-conversion OLEDs. The comparison of Current-Voltage-Luminance (JVL) characteristics is shown in Figure 53. Like the results from the photodetectors, the dark current of PCBM device decreased dramatically, resulting in a significant difference between IR and dark conditions. The operation window is 5V, which is enough value to make the device as the IR detection device. In the C60 device, due to high dark current, dark turn-on voltage was 5.0V, and luminance plots show no significant between the dark condition and the IR condition. This device cannot work as a photodetection and imaging application because it does not have the operation voltage window. This result shows that increasing the offset between the HOMO of the acceptor and the LUMO of the donor successfully reduced the charge generation effect.

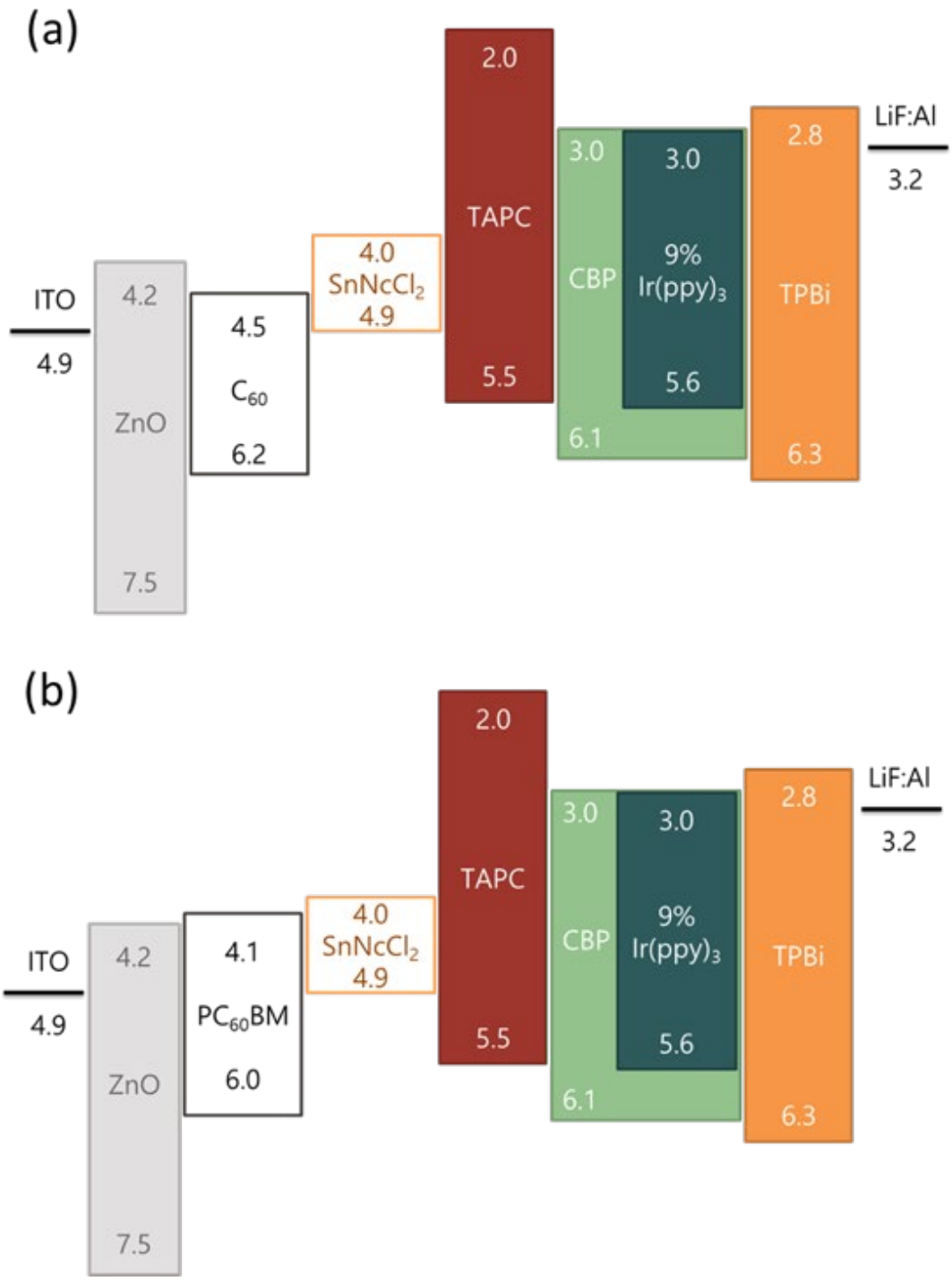

Figure 51 Schematic energy band diagram of the up-conversion OLEDs with (a) C_{60} acceptor, and (b) PCBM acceptor.

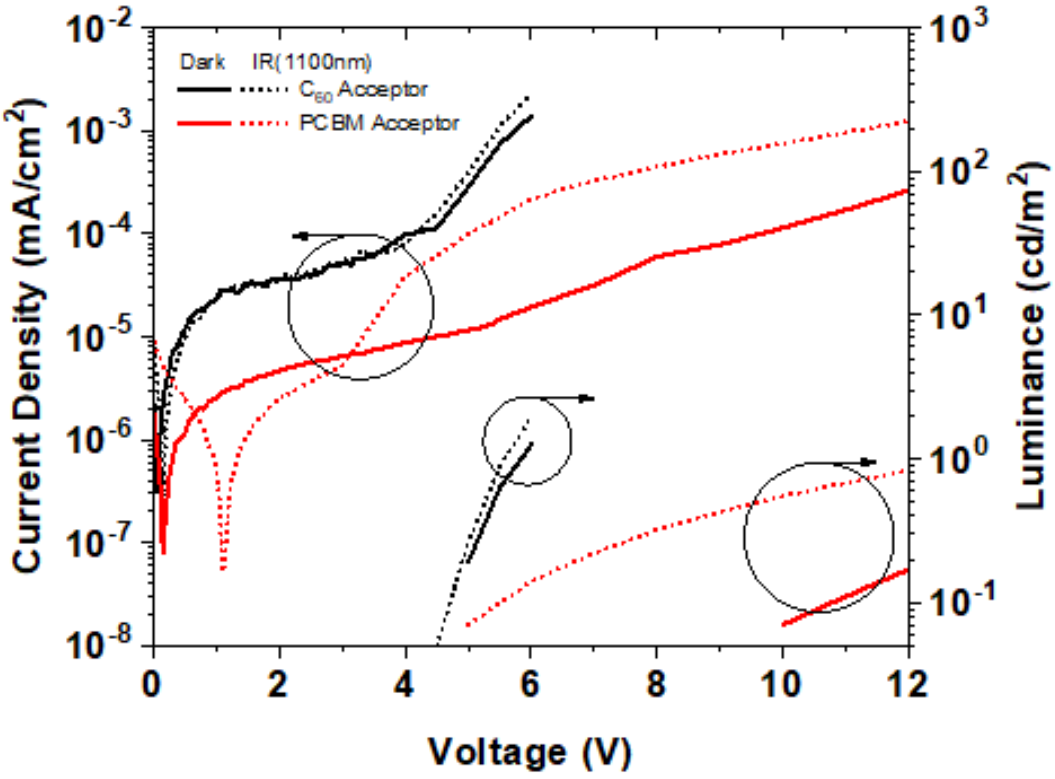

Figure 52 Current-Voltage-Luminance (JVL) Characteristics comparison

3.3. Hole Transport Layer Effect between SWIR Sensitizer and Emission Layer in up-conversion OLEDs

To achieve high photon-to-photon conversion efficiency, a good charge balance in the OLED part of the up-conversion device is crucial.[129, 130] While the HTL needs to have a proper HOMO level to efficiently extract photogenerated holes from a SWIR sensitizing layer to a light-emitting layer, the HTL needs to have a very shallow LUMO level to effectively block electrons injected from the cathode.

In the $SnNcCl_2$ photodetector result, TAPC was used as a hole transport layer (HTL) which also acts as an electron blocker to prevent the electron move from the emission layer (EML) to IR

sensitizing layer. But as shown in the schematic energy diagram in Figure 54 (a), the HOMO level of the TAPC is -5.5eV, which is much lower than 4.9eV, the HOMO level of $SnNcCl_2$.

Figure 55 shows the Current-Voltage-Luminance (JVL) characteristics of the devices with different HTL configurations. The device with MTDATA/TAPC bilayer HTLs (red lines) shows much lower dark current, but similar photocurrent above the IR turn-on voltage. Although the

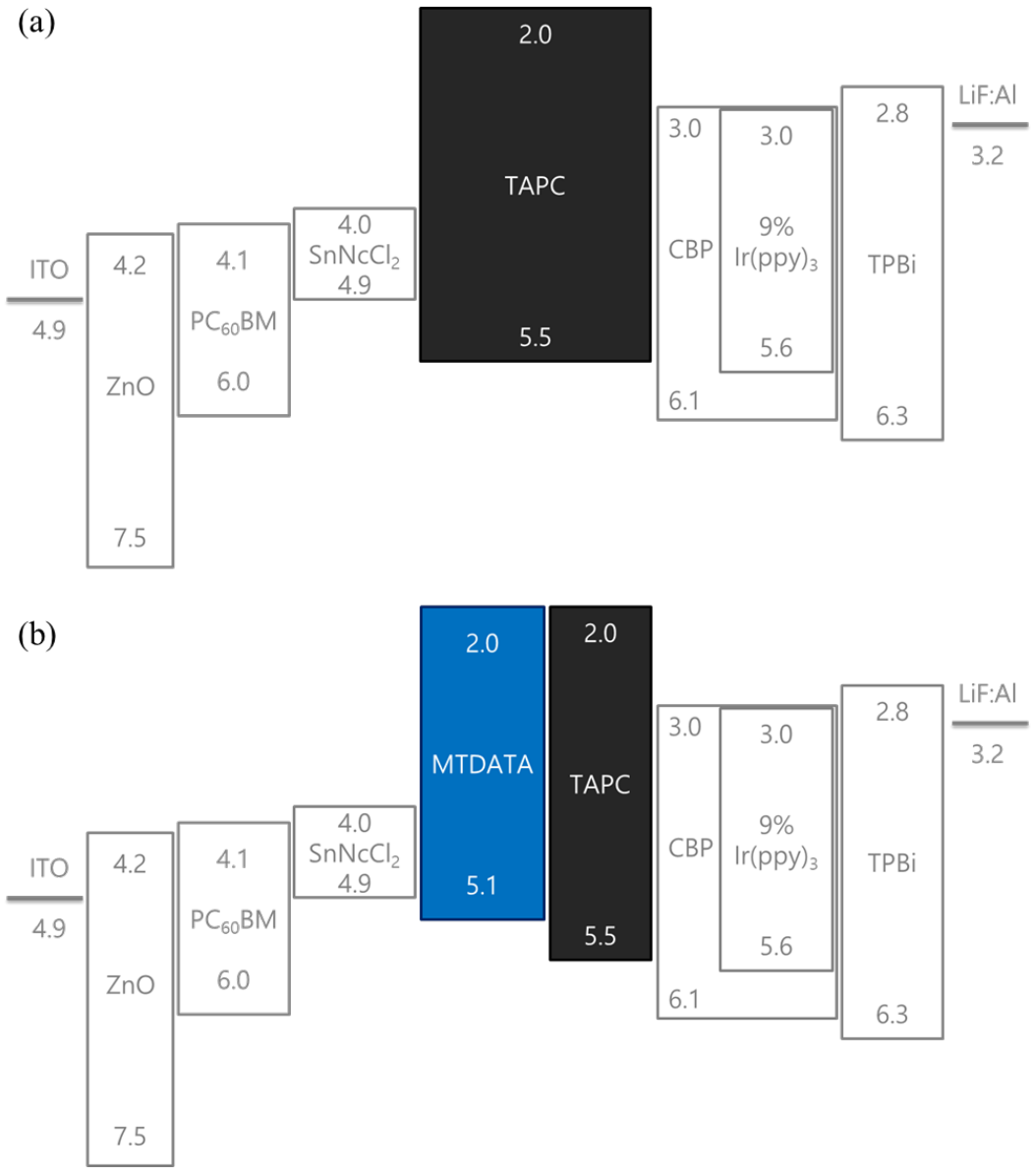

Figure 53 Schematic energy band diagram of the up-conversion OLEDs with (a) TAPC single HTL and (b) MTDATA/TAPC bilayer HTL

dark current was decreased over than 10^1 order, the luminance of the IR condition (dashed lines) was increased almost twice. This result shows that MTDATA/TAPC layers facilitate the photogenerated hole injection from the IR sensitizing layer to the emission layer. But due to this effect, the dark turn on voltage of the MTDATA/TAPC bilayer device was also decreased even though it has much lower dark current. Consequently, the operation voltage window got only 1V increased.

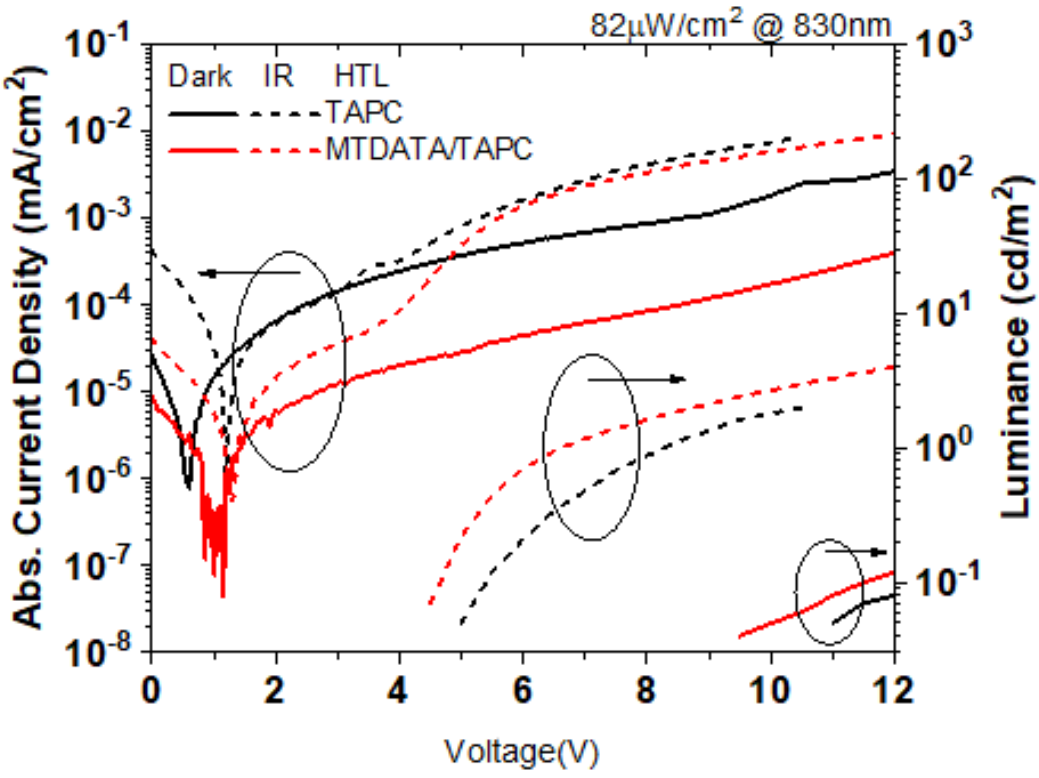

Figure 54 Comparison of TAPC single HTL and MTDATA/TAPC bilayer HTL on (a) Current-Voltage-Luminance (JVL) Characteristics

3.4. Hole blocking layer in up-conversion OLEDs

A key to the operation of the IR-to-visible up-conversion OLED is to keep the device in off-state while a voltage is applied to the device, and the device will only turn-on when infrared light is incident onto the device. Ideally, the device would be kept off even in the condition that a large voltage is applied to the device. This can be done by suppressing the injection of one type of carrier. Therefore, controlling the charge injection is critical to the operation of these IR-to-visible up-conversion OLEDs. While the operation of up-conversion devices has been demonstrated, the effect of charge injection on device performance has not systematically studied previously. A good hole blocker needs to extract photogenerated electrons efficiently for avoiding unwanted charge accumulation, while blocking hole injection from ITO anode. The HOMO of the hole blocker should be deep enough to block hole injection from ITO anode, and it is important to minimize the energy barrier between the LUMO of the hole blocker and the IR sensitizing layer. There has been no published study on the detailed role of the hole blocker in the up-conversion devices. After the successful demonstration of SWIR-to-Visible up-conversion OLEDs, the hole blocker effect is needed to be studied. Figure 56 shows a schematic energy band

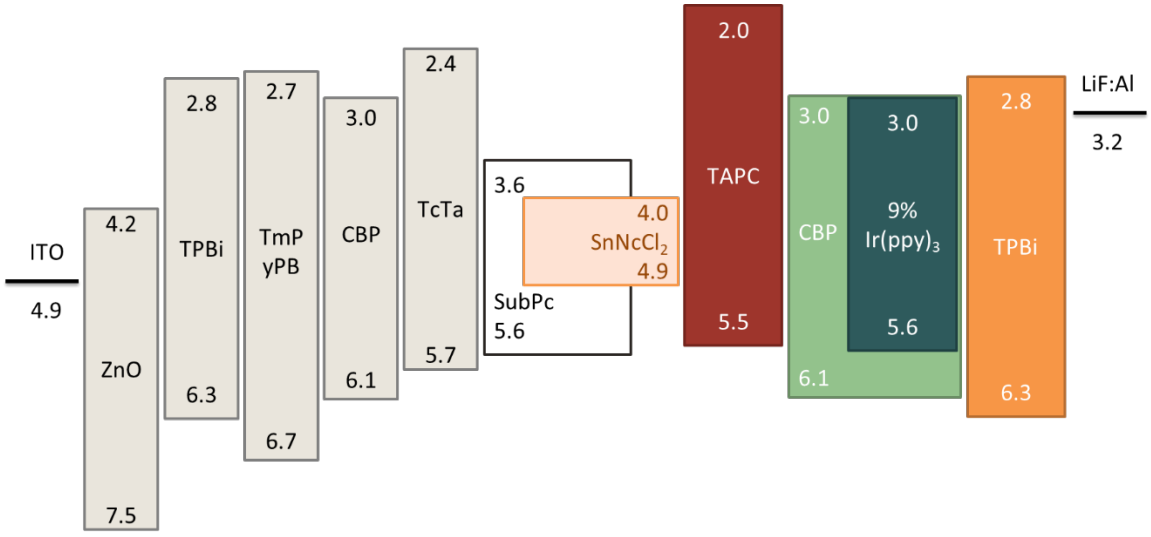

Figure 55 Schematic energy band diagram of materials used in the up-conversion OLEDs

diagram of materials used in the up-conversion OLEDs. As hole blocker materials, zinc oxide (ZnO), 2,2',2''-(1,3,5-Benzinetriyl)-tris(1-phenyl-1-H-benzimidazole) (TPBi), 1,3,5-Tri(m-pyridin-3-ylphenyl)benzene (TmPyPB), 4,4'-Bis(N-carbazolyl)-1,1'-biphenyl (CBP), and Tris(4-carbazoyl-9-ylphenyl)amine (TcTa) were used for comparison. They have various HOMO and LUMO energy levels to see the effect of the hole blocking layer. A boron subphthalocyanine chloride (SubPc) was chosen as the small molecule acceptor to make the SWIR sensitizing layer suitable for the thermal evaporation, because the solution-based PCBM can be used only with solution-based hole blocking layer materials. The comparison of luminance-voltage (L-V) characteristics is shown in Figure 57 (a). The devices using TPBi, CBP, and TcTa as a hole blocker shows no significant difference between the dark and the IR condition. These devices cannot be used for the SWIR imaging application because the operation window allows the devices working as the light detector. The HOMO levels of TPBi, CBP, TcTa are relatively close to the work function of the anode, therefore, as a result, the dark turn-on voltage is almost same as the IR turn-on voltage. The device with the TmPyPB hole blocker has small 1.5V of the operating voltage window, while the ZnO hole blocker has the operation voltage window of about 5V. The HOMO level of the TmPyPB is much shallower than the HOMO level of the ZnO, accordingly, the ZnO HBL device shows much higher dark turn-on voltage of 10V. Figure 57 (b) shows the photon-to-photon efficiency spectra of TmPyPB and ZnO HBL devices at maximum operation voltage, which is the bias of the dark turn-on voltage. The ZnO HBL device converted the IR to visible light with higher efficiency than TmPyPB HBL device, because of its wider operation voltage window as result of higher dark turn-on voltage. For the up-conversion device, the ZnO works the best HBL material because of its deep HOMO level.

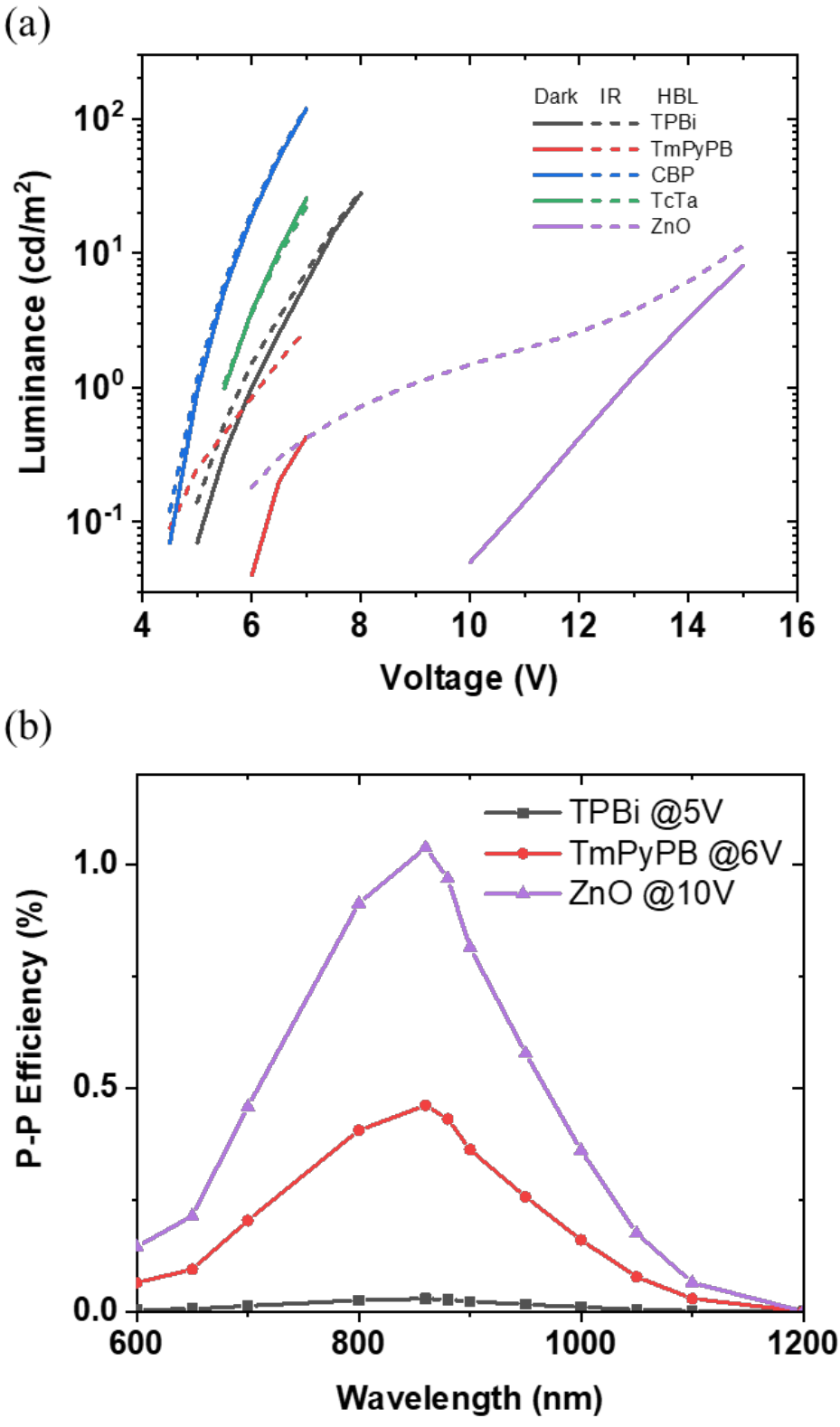

Figure 56 (a) Comparison of Luminance-Voltage (L-V) Characteristics of the up-conversion devices with various hole blockers, and (b) the photon-to-photon efficiency spectra of TmPyPB and ZnO HBL devices at maximum operation voltage.

CHAPTER VIII

CONCLUSION

1. Summary

The all-organic infrared-to-visible up-conversion OLEDs for low-cost SWIR imaging are studied and demonstrated by replacing CQD SWIR sensitizers to organic SWIR sensitizers. First, PBDTT-BTQ as a polymer SWIR sensitizer is synthesized with SWIR sensitivity up to 1200 nm by using the electron donating-accepting polymeric framework method. For low-bandgap small molecules, $SnNcCl_2$ is selected by the extended conjugation approach and showed strong SWIR sensitivity up to 1400 nm. Then, organic SWIR photodetectors using PBDTT-BTQ and $SnNcCl_2$ as the low-bandgap organic SWIR sensitizers are successfully fabricated with strong SWIR sensitivity up to 1200 nm. The photodetector using PBDTT-BTQ shows the maximum detectivity of 3×10^{11} Jones at the wavelength of 1000 nm, while the $SnNcCl_2$ photodetectors showing the maximum detectivity of 2×10^{11} Jones at the wavelength of 1000 nm. Finally, all-organic SWIR-to-visible up-conversion OLEDs are successfully demonstrated with SWIR sensitivity up to 1200nm for the first time in the world.

*** New Scientific Findings**

- The electron donating-accepting polymeric framework approach enables significantly low bandgap polymers with strong optical absorption at SWIR wavelength beyond 1000 nm.
- The IR-to-visible up-conversion OLEDs should first have sufficiently large operating voltages for obtaining high photon-to-photon conversion efficiency.
- With significantly low-bandgap donors having strong SWIR sensitivity beyond 1000 nm, however, the acceptors have to be sufficiently high LUMO levels of at least over 0.4 eV compared to the HOMO level of the SWIR sensitive low-bandgap donor for eliminating the charge generation effect to cause a significant reduction in the operating voltages in the up-conversion OLEDs, thus resulting in a significant decrease of photon-to-photon conversion efficiency.
- With an ITO anode with a work function of 4.45 eV, the wide-bandgap organic or inorganic materials for the hole blocking layer should have deeper HOMO level or valence band edge of more than 6.7 eV for proper up-conversion OLED operation with sufficiently-large operating voltages and high photon-to-photon conversion efficiency.

2. Recommendations for future research

The combination of donor-accepter materials is important to have proper energy band alignment in the IR sensitizing layer. A proper acceptor material can increase the photogeneration efficiency, especially for the PBDTT-BTQ:PCBM devices which has the LUMO level of the donor is below the LUMO level of the acceptor. In the $SnNcCl_2$, the PCBM works as the acceptor, but it is better to find the small molecule acceptor material to further simplifying the fabrication process and the bulk heterojunction formation.

The light emitting part was not the focus of this dissertation, but the higher OLED efficiency will offer higher photon-to-photon efficiency in the up-conversion devices. The HOMO level of the hole transport layer material is also important because the HTL is the interface between the photodetector part and the OLED part in the up-conversion devices.

As the further step to the SWIR region, the sensitizers with smaller bandgap can offer the longer wavelength absorption. Using the electron donating-accepting polymeric framework and the extended conjugation, lower bandgap materials can be synthesized or discovered.

The ZnO was employed for the HBL in this dissertation, but the organic HBL with deep HOMO level can be also effective HBL and offer more continuous fabrication process.

The spin-coating and the thermal evaporation methods are used in this dissertation, but using the organic materials, the printing method can be employed. The printing method offers low-cost fabrication and scale-up availability for ultra large area devices.

For the actual SWIR imaging device, the up-conversion OLEDs need to be combined with the optics parts and the Si-based CMOS camera assembly. The incident image needs to be focused on the up-conversion OLED, and the converted visible image has on the CMOS sensor. With further development, the up-conversion OLEDs will be directly fabricated on the surface of the CMOS sensor, resulting much more simplified structure for the SWIR imaging camera.

REFERENCES

1. R. Hany, M. Cremona and K. Strassel, Science and technology of advanced materials **20** (1), 497-510 (2019).
2. A. Armin, R. D. Jansen-van Vuuren, N. Kopidakis, P. L. Burn and P. Meredith, Nature communications **6** (2015).
3. B. Siegmund, A. Mischok, J. Benduhn, O. Zeika, S. Ullbrich, F. Nehm, M. Böhm, D. Spoltore, H. Fröb and C. Körner, Nature communications **8**, 15421 (2017).
4. F. P. G. de Arquer, A. Armin, P. Meredith and E. H. Sargent, Nature Reviews Materials **2** (3), 16100 (2017).
5. R. D. Jansen-van Vuuren, A. Armin, A. K. Pandey, P. L. Burn and P. Meredith, Adv Mater **28** (24), 4766-4802 (2016).
6. K. Mangold, J. A. Shaw and M. Vollmer, European Journal of physics **34** (6), S51 (2013).
7. Z. Guo, S. Park, J. Yoon and I. Shin, Chemical Society Reviews **43** (1), 16-29 (2014).
8. S. Chinnathambi and N. Shirahata, Science and technology of advanced materials **20** (1), 337-355 (2019).
9. T. Rauch, M. Böberl, S. F. Tedde, J. Fürst, M. V. Kovalenko, G. Hesser, U. Lemmer, W. Heiss and O. Hayden, nature photonics **3** (6), 332 (2009).
10. M. Wu, D. N. Congreve, M. W. Wilson, J. Jean, N. Geva, M. Welborn, T. Van Voorhis, V. Bulović, M. G. Bawendi and M. A. Baldo, Nature Photonics **10** (1), 31 (2016).
11. edmundoptics.com, Electromagnetic Spectrum Illustrating SWIR Wavelength Range.
12. A. Singh and R. Pal, Applied Physics A **123** (11), 701 (2017).
13. D. Y. Kim, D. W. Song, N. Chopra, P. De Somer and F. So, Advanced Materials **22** (20), 2260-2263 (2010).
14. J. Sandhu, A. Heberle, B. Alphenaar and J. Cleaver, Appl Phys Lett **76** (12), 1507-1509 (2000).
15. Y. Yang, W. Shen, H. Liu, S. Laframboise, S. Wicaksono, S. Yoon and K. Tan, Appl Phys Lett **94** (9), 093504 (2009).
16. Y. Wang and J. Ohwaki, Journal of applied physics **74** (2), 1272-1278 (1993).
17. D. Y. Kim, K. R. Choudhury, J. W. Lee, D. W. Song, G. Sarasqueta and F. So, Nano letters **11** (5), 2109-2113 (2011).
18. H. Liu, M. Gao and P. Poole, Electronics Letters **36** (15), 1300-1301 (2000).
19. K. Russell, I. Appelbaum, H. Temkin, C. Perry, V. Narayanamurti, M. Hanson and A. Gossard, Appl Phys Lett **82** (18), 2960-2962 (2003).

20. Y. Mita, Appl Phys Lett **39** (8), 587-589 (1981).
21. P. Kruse, F. Pribble and R. Schulze, Journal of Applied Physics **38** (4), 1718-1720 (1967).
22. D. Ban, S. Han, Z. Lu, T. Oogarah, A. SpringThorpe and H. Liu, Appl Phys Lett **90** (9), 093108 (2007).
23. M. A. Hines and G. D. Scholes, Advanced Materials **15** (21), 1844-1849 (2003).
24. T.-H. Lai, J. W. Lee, J. R. Manders and F. So, Scientific reports **4**, 5946 (2014).
25. N. T. Kalyani and S. Dhoble, Renewable and Sustainable Energy Reviews **16** (5), 2696-2723 (2012).
26. H. S. Vogelbaum and G. Sauvé, Synthetic Metals **223**, 107-121 (2017).
27. G. Dennler, M. C. Scharber and C. J. Brabec, Advanced Materials **21** (13), 1323-1338 (2009).
28. Y. Lin, Y. Li and X. Zhan, Chemical Society Reviews **41** (11), 4245-4272 (2012).
29. H. Sirringhaus, Proceedings of the IEEE **97** (9), 1570-1579 (2009).
30. K. J. Baeg, M. Binda, D. Natali, M. Caironi and Y. Y. Noh, Adv Mater **25** (31), 4267-4295 (2013).
31. H. Dong, H. Zhu, Q. Meng, X. Gong and W. Hu, Chem Soc Rev **41** (5), 1754-1808 (2012).
32. M. Kielar, O. Dhez, G. Pecastaings, A. Curutchet and L. Hirsch, Sci Rep **6**, 39201 (2016).
33. J. Hamer and D. Scott, 2017.
34. J. Kim, Market Report, 2019.
35. Statista, Statista (May 2020) (2020).
36. M. Pope, H. Kallmann and P. Magnante, The Journal of Chemical Physics **38** (8), 2042-2043 (1963).
37. C. W. Tang and S. A. VanSlyke, Appl Phys Lett **51** (12), 913-915 (1987).
38. C. W. Tang, S. A. VanSlyke and C. H. Chen, Journal of applied physics **65** (9), 3610-3616 (1989).
39. M. A. Baldo, D. F. O'Brien, Y. You, A. Shoustikov, S. Sibley, M. E. Thompson and S. R. Forrest, Nature **395** (6698), 151-154 (1998).
40. N. J. Turro, *Modern molecular photochemistry*. (University science books, 1991).
41. N. Patel, S. Cina and J. Burroughes, IEEE Journal of selected topics in quantum electronics **8** (2), 346-361 (2002).
42. T. Főrster, Discussions of the Faraday Society **27**, 7-17 (1959).
43. D. L. Dexter, The Journal of Chemical Physics **21** (5), 836-850 (1953).
44. C. Adachi, M. A. Baldo, S. R. Forrest, S. Lamansky, M. E. Thompson and R. C. Kwong, Appl Phys Lett **78** (11), 1622-1624 (2001).
45. C. Adachi, M. A. Baldo, M. E. Thompson and S. R. Forrest, Journal of Applied Physics **90** (10), 5048-5051 (2001).
46. S. R. Forrest, MRS Bulletin **30** (01), 28-32 (2011).
47. Y. Higashi, K.-S. Kim, H.-G. Jeon and M. Ichikawa, Journal of Applied Physics **108** (3), 034502 (2010).
48. M. Ichikawa, T. Takeuchi, H.-G. Jeon, Y. Jin, S. Lee and K.-S. Kim, Japanese Journal of Applied Physics **51** (3R), 034103 (2012).
49. K.-H. Lee, D.-S. Leem, J. S. Castrucci, K.-B. Park, X. Bulliard, K.-S. Kim, Y. W. Jin, S. Lee, T. P. Bender and S. Y. Park, Acs Appl Mater Inter **5** (24), 13089-13095 (2013).
50. K.-H. Lee, D.-S. Leem, S. Sul, K.-B. Park, S.-J. Lim, H. Han, K.-S. Kim, Y. W. Jin, S. Lee and S. Y. Park, J Mater Chem C **1** (15), 2666-2671 (2013).
51. A. A. Bakulin, S. D. Dimitrov, A. Rao, P. C. Y. Chow, C. B. Nielsen, B. C. Schroeder, I. McCulloch, H. J. Bakker, J. R. Durrant and R. H. Friend, The Journal of Physical Chemistry Letters **4** (1), 209-215 (2013).

52. D. C. Coffey, B. W. Larson, A. W. Hains, J. B. Whitaker, N. Kopidakis, O. V. Boltalina, S. H. Strauss and G. Rumbles, The Journal of Physical Chemistry C **116** (16), 8916-8923 (2012).
53. K. Kudo and T. Moriizumi, Appl Phys Lett **39** (8), 609-611 (1981).
54. H. Lee, S. Nam, H. Kwon, S. Lee, J. Kim, W. Lee, C. Lee, J. Jeong, H. Kim and T. J. Shin, J Mater Chem C **3** (7), 1513-1520 (2015).
55. S. H. Park, A. Roy, S. Beaupre, S. Cho, N. Coates, J. S. Moon, D. Moses, M. Leclerc, K. Lee and A. J. Heeger, Nature photonics **3** (5), 297-302 (2009).
56. J. M. Shaw and P. F. Seidler, IBM Journal of Research and Development **45** (1), 3-9 (2001).
57. E. Cantatore, A Technology-Enabled Revolution, Springer (2013).
58. M. Berggren, D. Nilsson and N. D. Robinson, Nature materials **6** (1), 3-5 (2007).
59. V. Sukhovatkin, S. Musikhin, I. Gorelikov, S. Cauchi, L. Bakueva, E. Kumacheva and E. Sargent, Optics letters **30** (2), 171-173 (2005).
60. E. H. Sargent, Nature Photonics **3** (6), 325 (2009).
61. G. Sarasqueta, K. R. Choudhury and F. So, Chemistry of Materials **22** (11), 3496-3501 (2010).
62. P. E. Keivanidis, S. H. Khong, P. K. H. Ho, N. C. Greenham and R. H. Friend, Appl Phys Lett **94** (17), 123 (2009).
63. P. Peumans, V. Bulović and S. Forrest, Appl Phys Lett **76** (26), 3855-3857 (2000).
64. J. Xue and S. R. Forrest, Journal of applied physics **95** (4), 1859-1868 (2004).
65. S. Matthew Menke, R. Pandey and R. J. Holmes, Appl Phys Lett **101** (22), 223301 (2012).
66. K. H. Lee, D. S. Leem, J. S. Castrucci, K. B. Park, X. Bulliard, K. S. Kim, Y. W. Jin, S. Lee, T. P. Bender and S. Y. Park, Acs Appl Mater Inter **5** (24), 13089-13095 (2013).
67. K. H. Lee, D. S. Leem, S. Sul, K. B. Park, S. J. Lim, H. Han, K. S. Kim, Y. W. Jin, S. Lee and S. Y. Park, J Mater Chem C **1** (15), 2666-2671 (2013).
68. X. Xu, P. Xu, Y. Hao and W. Qin, Organic Electronics (2017).
69. H. Zhang, S. Jenatsch, J. De Jonghe, F. Nüesch, R. Steim, A. C. Véron and R. Hany, Scientific reports **5**, 9439 (2015).
70. A. Kraft, A. C. Grimsdale and A. B. Holmes, Angewandte Chemie International Edition **37** (4), 402-428 (1998).
71. G. Yu, H. Yu, Y. Oi, P. Desjardins, X. Meng, J. P. Gao, E. Todd and N. Song, Pure Appl. Chem **76** (7-8), 1435-1443 (2004).
72. X. Liu, H. Wang, T. Yang, W. Zhang and X. Gong, Acs Appl Mater Inter **4** (7), 3701-3705 (2012).
73. P. Murto, Z. Genene, C. M. Benavides, X. Xu, A. Sharma, X. Pan, O. Schmidt, C. J. Brabec, M. R. Andersson and S. F. Tedde, ACS Macro Letters **7** (4), 395-400 (2018).
74. X. Gong, M. Tong, Y. Xia, W. Cai, J. S. Moon, Y. Cao, G. Yu, C.-L. Shieh, B. Nilsson and A. J. Heeger, Science **325** (5948), 1665-1667 (2009).
75. C. H. Cheung, J. Subbiah, C. M. Amb, J. R. Reynolds and F. So, IEEE Transactions on Electron Devices **61** (11), 3852-3857 (2014).
76. G. Yu, K. Pakbaz and A. Heeger, Appl Phys Lett **64** (25), 3422-3424 (1994).
77. A. Falco, L. Cinà, G. Scarpa, P. Lugli and A. Abdellah, Acs Appl Mater Inter **6** (13), 10593-10601 (2014).
78. G. Yu, J. Wang, J. McElvain and A. J. Heeger, Advanced Materials **10** (17), 1431-1434 (1998).
79. I. Deckman, P. B. Lechêne, A. Pierre and A. C. Arias, Organic Electronics **56**, 139-145 (2018).
80. G. Li, V. Shrotriya, J. Huang, Y. Yao, T. Moriarty, K. Emery and Y. Yang, in *Materials For Sustainable Energy: A Collection of Peer-Reviewed Research and Review Articles from Nature Publishing Group* (World Scientific, 2011), pp. 80-84.

81. J. Wolf, F. Cruciani, A. El Labban and P. M. Beaujuge, Chemistry of Materials **27** (12), 4184-4187 (2015).
82. Y. Liang, Z. Xu, J. Xia, S. T. Tsai, Y. Wu, G. Li, C. Ray and L. Yu, Advanced materials **22** (20), E135-E138 (2010).
83. W. Zhao, S. Li, H. Yao, S. Zhang, Y. Zhang, B. Yang and J. Hou, Journal of the American Chemical Society **139** (21), 7148-7151 (2017).
84. X. Liu, H. Wang, T. Yang, W. Zhang, I.-F. Hsieh, S. Z. Cheng and X. Gong, Organic Electronics **13** (12), 2929-2934 (2012).
85. H. Zhou, L. Yang and W. You, Macromolecules **45** (2), 607-632 (2012).
86. L. Zhang, T. Yang, L. Shen, Y. Fang, L. Dang, N. Zhou, X. Guo, Z. Hong, Y. Yang, H. Wu, J. Huang and Y. Liang, Advanced Materials **27** (41), 6496-6503 (2015).
87. H. Xu, J. Li, B. H. K. Leung, C. C. Y. Poon, B. S. Ong, Y. Zhang and N. Zhao, Nanoscale **5** (23), 11850-11855 (2013).
88. S. Wu, B. Xiao, B. Zhao, Z. He, H. Wu and Y. Cao, Small **12** (25), 3374-3380 (2016).
89. E. Perzon, F. Zhang, M. Andersson, W. Mammo, O. Inganäs and M. R. Andersson, Advanced Materials **19** (20), 3308-3311 (2007).
90. C.-Y. Yu, C.-P. Chen, S.-H. Chan, G.-W. Hwang and C. Ting, Chemistry of Materials **21** (14), 3262-3269 (2009).
91. M. E. Foster, B. A. Zhang, D. Murtagh, Y. Liu, M. Y. Sfeir, B. M. Wong and J. D. Azoulay, Macromolecular Rapid Communications **35** (17), 1516-1521 (2014).
92. Y. Lee, T. P. Russell and W. H. Jo, Organic Electronics **11** (5), 846-853 (2010).
93. G. Zhang, Y. Fu, Q. Zhang and Z. Xie, Polymer **51** (11), 2313-2319 (2010).
94. E. Perzon, X. Wang, S. Admassie, O. Inganäs and M. R. Andersson, Polymer **47** (12), 4261-4268 (2006).
95. X. Zhang, T. T. Steckler, R. R. Dasari, S. Ohira, W. J. Potscavage, S. P. Tiwari, S. Coppee, S. Ellinger, S. Barlow, J.-L. Bredas, B. Kippelen, J. R. Reynolds and S. R. Marder, Journal of Materials Chemistry **20** (1), 123-134 (2010).
96. T. Dallos, D. Beckmann, G. Brunklaus and M. Baumgarten, Journal of the American Chemical Society **133** (35), 13898-13901 (2011).
97. E. Zhou, K. Hashimoto and K. Tajima, Polymer **54** (24), 6501-6509 (2013).
98. T. T. Steckler, P. Henriksson, S. Mollinger, A. Lundin, A. Salleo and M. R. Andersson, Journal of the American Chemical Society **136** (4), 1190-1193 (2014).
99. H. Yao, L. Ye, H. Zhang, S. Li, S. Zhang and J. Hou, Chemical Reviews **116** (12), 7397-7457 (2016).
100. J. Yuan, Z. Zhai, H. Dong, J. Li, Z. Jiang, Y. Li and W. Ma, Advanced Functional Materials **23** (7), 885-892 (2013).
101. J. Warnan, A. El Labban, C. Cabanetos, E. T. Hoke, P. K. Shukla, C. Risko, J.-L. Brédas, M. D. McGehee and P. M. Beaujuge, Chemistry of Materials **26** (7), 2299-2306 (2014).
102. H. Yu, D. Kim, J. Lee, S. Baek, J. Lee, R. Singh and F. So, Nature Photonics **10** (2), 129 (2016).
103. X. Wang, H. Li, Z. Su, F. Fang, G. Zhang, J. Wang, B. Chu, X. Fang, Z. Wei and B. Li, Organic Electronics **15** (10), 2367-2371 (2014).
104. W. Lv, Y. Peng, J. Zhong, X. Luo, Y. Li, T. Zheng, Y. Tang, L. Du and L. Peng, IEEE Photonics Technology Letters **27** (19), 2043-2046 (2015).
105. R. F. Bailey-Salzman, B. P. Rand and S. R. Forrest, Appl Phys Lett **91** (1), 013508 (2007).
106. R. Loutfy, J. Sharp, C. Hsiao and R. Ho, Journal of Applied Physics **52** (8), 5218-5230 (1981).
107. D. Placencia, W. Wang, R. C. Shallcross, K. W. Nebesny, M. Brumbach and N. R. Armstrong, Advanced Functional Materials **19** (12), 1913-1921 (2009).

108. N. Wang, J. Yu, Y. Zang, J. Huang and Y. Jiang, Solar Energy Materials and Solar Cells **94** (2), 263-266 (2010).
109. S. Schumann, R. Hatton and T. Jones, The Journal of Physical Chemistry C **115** (11), 4916-4921 (2011).
110. Y. Kinoshita, T. Hasobe and H. Murata, Appl Phys Lett **91** (8), 083518 (2007).
111. K. Chauhan, P. Sullivan, J. Yang and T. Jones, The Journal of Physical Chemistry C **114** (7), 3304-3308 (2010).
112. F. So and Y. Gao, Solar Energy Materials and Solar Cells **93** (9), 1688-1691 (2009).
113. R. O. Loutfy and J. H. Sharp, The Journal of Chemical Physics **71** (3), 1211-1217 (1979).
114. R. Pandey, R. A. Kerner, S. M. Menke, J. Holst, K. V. Josyula and R. J. Holmes, Organic Electronics **14** (3), 804-808 (2013).
115. I. H. Campbell and B. K. Crone, Appl Phys Lett **95** (26), 336 (2009).
116. I. Campbell, Appl Phys Lett **97** (3), 149 (2010).
117. E. Jakubikova, I. H. Campbell and R. L. Martin, The Journal of Physical Chemistry A **115** (33), 9265-9272 (2011).
118. G. Konstantatos, J. Clifford, L. Levina and E. H. Sargent, Nature photonics **1** (9), 531-534 (2007).
119. A. Rogalski, J. Antoszewski and L. Faraone, Journal of applied physics **105** (9), 4 (2009).
120. X. An, F. Liu, Y. J. Jung and S. Kar, Nano letters **13** (3), 909-916 (2013).
121. E. H. Sargent, Advanced Materials **17** (5), 515-522 (2005).
122. J. W. Lee, D. Y. Kim, S. Baek, H. Yu and F. So, Small **12** (10), 1328-1333 (2016).
123. M. A. Green, Nature Energy **1** (1), 1-4 (2016).
124. A. C. Arias, J. D. MacKenzie, I. McCulloch, J. Rivnay and A. Salleo, Chemical reviews **110** (1), 3-24 (2010).
125. J. Lee, S.-J. Ko, H. Lee, J. Huang, Z. Zhu, M. Seifrid, J. Vollbrecht, V. V. Brus, A. Karki and H. Wang, ACS Energy Letters **4** (6), 1401-1409 (2019).
126. J. Huang, J. Lee, J. Vollbrecht, V. V. Brus, A. L. Dixon, D. X. Cao, Z. Zhu, Z. Du, H. Wang and K. Cho, Advanced Materials, 1906027 (2019).
127. C. W. Tang, Appl Phys Lett **48** (2), 183-185 (1986).
128. Y. Yao, Y. Liang, V. Shrotriya, S. Xiao, L. Yu and Y. Yang, Advanced Materials **19** (22), 3979-3983 (2007).
129. R. Meerheim, S. Scholz, S. Olthof, G. Schwartz, S. Reineke, K. Walzer and K. Leo, Journal of Applied Physics **104** (1), 014510 (2008).
130. N. Chopra, J. Lee, Y. Zheng, S.-H. Eom, J. Xue and F. So, Acs Appl Mater Inter **1** (6), 1169-1172 (2009).

VITA

Gijun Seo

Candidate for the Degree of

Doctor of Philosophy

Dissertation: ALL-ORGANIC INFRARED-TO-VISIBLE UP-CONVERSION OLEDS FOR LOW-COST SWIR IMAGING

Major Field: Materials Science and Engineering

Biographical:

Education:

Completed the requirements for the Doctor of Philosophy in Materials Science and Engineering at Oklahoma State University, Stillwater, Oklahoma in July, 2020.

Completed the requirements for the Master of Engineering in Innovation Technologies at Ecole Polytechnique, Palaiseau, France in 2015.

Completed the requirements for the Master of Engineering in Information Display at KyungHee University, Seoul, South Korea in 2015.

Completed the requirements for the Bachelor of Science in Information Display at KyungHee University, Seoul, South Korea in 2012.